Philipps Universität Marburg

Single-frequency and Dual-wavelength Operation of Vertical-external-cavity Surface-emitting Lasers

Dissertation

zur

Erlangung des Doktorgrades

der Naturwissenschaften

(Dr. rer. nat.)

dem

Fachbereich Physik

der Philipps-Universität Marburg

vorgelegt von

Fan Zhang

aus Jilin, China

Marburg/Lahn, 2016

Vom Fachbereich Physik der Philipps-Universität Marburg
als Dissertation angenommen am:

Erstgutachter: Prof. Dr. Martin Koch
Zweitgutachter: Dr. habil. Wolfgang Stolz

Tag der mündlichen Prüfung: 20. 02. 2017
Hochschulkennziffer 1180

Acknowledgements

This thesis presents the work carried out in Philipps-Universität Marburg, during the years 2012-2016. Indeed, the four years in this beautiful university town has been the most wonderful time so far in my life. The credit should go to many people, to whom I would like to express my gratitude.

Foremost, I would like to thank my supervisor, "Doktorvater", Professor Martin Koch, for giving me the opportunity to be a Ph.D. candidate in his work group, as well as for his guidance in the scientific research and beyond. His encouragement is a treasure of life to me.

My special thank goes to the leader of our VECSEL-team, Dr. Arash Rahimi-Iman, whom I have been looking up to, for his consistent help and support in both work and daily life. I'm going to miss the fruitful and joyful discussions in the group meetings organized by him.

I gratefully acknowledge Professor Wolfgang Stolz, who has been supporting me with his insightful comments and discussions. Thanks to the excellent laser chips provided by his work group, this work was able to proceed successfully.

I also owe many thanks to my former colleagues, Dr. Bernd Heinen and Dr. Matthias Wichmann, for their valuable help in the beginning stage of my Ph.D. time.

I always feel very lucky that I have joined Prof. Koch's group, because I have met so many kind and outstanding colleagues here, whom I consider as my family in Germany. I would like to thank Dr. Christoph Möller, Dr. Mahmoud Gaafar and everyone in the VECSEL-team for their help. I'm grateful for the cheerful lunch-time spent with the "Mensa squad", which includes Dr. Marina Gerhard, Dr. Ralf Gente, Maximilian Schneider and others.

Forty years ago, my parents left the small villages in the northeast of China with nothing but their knowledge and determination. Now, after decades of hard working, not only they have a home they can be proud of, but also they help their son realize his dream, which he can never repay but will always be grateful for.

Finally, I would like to give my beautiful wife, Meihe Xu, a huge hug. Without her love and support, I could never have come this far.

Abstract

Vertical-external-cavity surface-emitting lasers (VECSELs), also referred to as semiconductor disk lasers (SDLs), were invented in the mid-1990s by combining the gain media of semiconductor lasers with the geometry concepts of solid-state disk lasers. After two decades of research and development, this kind of laser offers a high-power output with excellent beam quality at a wavelength which can be tailored by semiconductor bandgap engineering. Moreover, the flexible external cavity of VECSELs allows for the utilization of intracavity elements and saturable absorbers. This feature provides the possibility to operate VECSELs under specific function modes such as single-frequency operation, dual-wavelength operation, and mode-locking.

This work focuses on the experimental study and development of single-frequency as well as dual-wavelength VECSELs. Additionally, an important factor, namely the spectral detuning of VECSELs is discussed and its impact on the performance of the device is experimentally demonstrated.

In order to achieve single-frequency operation, the VECSEL is allowed to operate only on fundamental transverse mode, single longitudinal mode, and single polarization mode. Therefore, to suppress the undesired modes, losses are required to a certain degree. However, this makes the realization of a high-power output challenging, where an overall high gain and a low loss level for the laser mode are favorable. In this work, a high-power single-frequency VECSEL is implemented by balancing the gain and the losses of the laser in combination with frequency stabilization methods. The maximum passively stabilized single-frequency output power from this device reaches 23.6 W, which is to this date the highest power among all single-frequency semiconductor lasers. The major noise sources are identified by analyzing the laser linewidth with respect to the sampling time. In order to further stabilize the single-frequency VECSEL, both passive and active frequency stabilization techniques are applied.

In contrast to a single-frequency laser, laser emission from dual-wavelength VECSELs contains two clusters of multiple longitudinal modes, which can be used for intracavity difference-frequency generation (DFG). For instance, Scheller et al. presented a room-temperature terahertz source based on a dual-wavelength VECSEL. However, both the achievable intracavity power and wavelength spacing of the two colors are limited by the single-chip design. Here, an alternative approach is demonstrated in which two different VECSEL chips are serially connected in one resonant cavity. In this way, the gain of both chips are combined, which enables dual-wavelength operation with

over 600 W intracavity power at a wavelength spacing of 10 nm. The wavelength spacing can be flexibly altered by employing different chip sets and/or intracavity filters. Furthermore, to complement the characterization of the existing terahertz-emitting VECSELs, the beam quality of the terahertz signal is investigated. According to the ISO standard, the deduced M^2-factors for the x- and y-axis amount to 1.41 and 1.72, respectively, which confirm the high quality of the terahertz beam emitted from this intracavity-DFG-based source.

In an additional effort to optimize the performance of VECSELs, which strongly depends on the thermal management, the chip design and its quality, the spectral detuning of VECSELs is targeted. The detuning of VECSELs is defined as the wavelength difference between the material gain and the longitudinal confinement factor at room temperature. Although the detuning is a key factor regarding the output power, threshold, and emission wavelength, it is difficult to conduct experimental studies while excluding the influence of other parameters. In this work, the cavity angle of a V-shaped cavity is varied to change the detuning of a VECSEL chip. Then the impact of different detunings on the performance of the device is demonstrated: By changing the detuning from -37 to -20 nm, an increment of the maximum output power by 70% is observed, while the threshold pump power is modified by a factor of four. Moreover, the wavelength tunability of the VECSEL can be greatly enhanced by the modification of the cavity angle, which is practical for applications that require additional wavelength accessibility.

Zusammenfassung

Vertical-External-Cavity Surface-Emitting Lasers (VECSELs), also oberflächenemittierende Laser mit vertikal angeordneter externer Kavität, wurden Mitte der 1990er-Jahre als eine weitere Klasse von vertikalemittierenden Lasern eingeführt. Diese bedienen sich einer Kombination aus laseraktiven Medien von Halbleiterlasern und den geometrischen Konzepten von Festkörper-Scheibenlasern, weshalb sie auch Halbleiter-Scheibenlaser (*Semiconductor Disk Lasers*, SDLs) genannt werden. Nach zwei Jahrzehnten an Forschung und Entwicklung bietet dieser Typ Halbleiterlaser nicht nur Zugang zuhohen Leistungen, sondern auch mit hervorragender Strahlqualität. Die Wellenlänge von VECSELn kann recht komfortabel und flexibel mithilfe der Bandlückengestaltung in der Halbleitertechnik angepasst werden. Weiterhin ermöglicht das Kavitätsdesign dieser Laser die Nutzung von zusätzlichen Elementen im externen Resonator und die Nutzung von sättigbaren Absorberspiegeln. Dank dieser Eigenschaft können VECSEL in verschiedenen Modi wie Dauerstrich- und Zwei-Farben-Betrieb verwendet werden, und eignen sich auch für die aus Ultrakurzpulslasern bekannte Modenkopplung.

In der vorliegenden Arbeit liegt der Schwerpunkt auf die experimentelle Untersuchung und Entwicklung von Einzelfrequenz- und Zwei-Farben-VECSELn. Des Weiteren wird die spektrale Verstimmung (das *Detuning*) von VECSELn betrachtet und ihr Einfluss auf die Leistung des VECSELs experimentell untersucht.

Um einen Dauerstrichbetrieb im schmalbandigen Einzelfrequenzmodus zu erzielen, muss der VECSEL sehr selektiv betrieben werden. Dazu muss die Lasermode in der transversalen Grundmode und mit einer selektierten Polarisation anschwingen, und nur eine einzelne Longitudinalmode aufweisen. Um unerwünschte Moden zu unterdrücken, sind optische Verluste bis zu einem gewissen Grad sogar erforderlich. Dies erschwert jedoch die Erzielung hoher Ausgangsleistungen, welche nur durch einen hohen Gewinn der Lasermode bei gleichzeitig niedrigen Verlusten begünstigt wird. In dieser Arbeit wird ein besonders leistungsstarker Einzelfrequenz-VECSEL realisiert, indem Gewinn und Verluste des Lasers sorgfältig im Hinblick auf einen einmodigen Betrieb ausgleichen werden. Die maximal erzielte Dauerstrich-Ausgangsleistung dieses VECSELs beträgt 23.6 W, was im Bereich Einzelfrequenz-Halbleiterlaser bis zur heutigen Zeit einen Rekordwert darstellt. Die größten Störquellen für einen sauberen Einzelfrequenzbetrieb werden identifiziert, indem die Laserlinienbreite im Hinblick auf die

Abtastzeit untersucht wird. Um den Einzelfrequenz-VECSEL zusätzlich zu stabilisieren, werden sowohl passive als auch aktive Frequenzstabilisierungstechniken angewandt.

Im Gegensatz zu Einzelfrequenzlasern besitzt die Laseremission von Zwei-Farben-VECSELn zwei spektral getrennte Gruppen longitudinaler Moden, die zur intrakavitären Differenzfrequenzbildung (Difference-Frequency Generation, DFG) genutzt werden können. So haben Scheller et al. beispielsweise eine Zimmertemperatur-Terahertz-Quelle basierend auf einem Zwei-Farben-VECSEL präsentiert. Allerdings werden sowohl die im Resonator erzielbare Leistung als auch der Wellenlängenabstand der zwei Farben durch das Einzel-Chip-Design begrenzt. An dieser Stelle wird eine alternative Herangehensweise vorgestellt, die zwei verschiedene VECSEL-Chips seriell in einem Hohlraumresonator verbindet. Auf diese Weise wird der Gewinn beider Chips kombiniert, was zu einem Zwei-Farben-Betrieb mit über 600 W Leistung im Resonator bei einer Wellenlängendifferenz von 10 nm führt. Der Wellenlängenabstand kann in diesem System jedoch unter Verwendung verschiedener Chipsätze und/oder Filter im Resonator flexibel verändert werden. Ergänzt wird die Beschreibung der bestehenden Terahertz-emittierenden VECSEL durch die Untersuchung der Strahlqualität des emittierten Terahertz-Signals. Gemäß des ISO-Standards beträgt der abgeleitete M^2-Faktor für die X- und Y-Achse 1,41 bzw. 1,72, was die hohe Qualität des intrakavitär erzeugten DFG-basierten Terahertz-Strahls dieser Quelle bestätigt.

Ergänzend zu vorangehenden Optimierungsbemühungen in Bezug auf die Leistungsfähigkeit von VECSELn, die stark vom thermischen Management, dem Chipdesign und der Chipqualität abhängt, wird im Rahmen dieser Arbeit auch die spektrale Verstimmung von VECSELn näher untersucht. Unter der Verstimmung von VECSELn versteht man die Wellenlängendifferenz zwischen dem Gewinn im Lasermedium und dem longitudinalen Einschluss-Faktor der Mikrokavität bei Raumtemperatur. Obwohl die Verstimmung ein wesentlicher Faktor hinsichtlich Ausgangsleistung, Laserschwelle und Emissionswellenlänge ist, ist es schwierig, experimentelle Studien unter Ausschluss der Einflüsse anderer Parameter durchzuführen. In dieser Arbeit wird erstmals der Kavitätswinkel eines V-förmigen Resonators variiert, um die Verstimmung eines VECSEL-Chips gezielt zu verändern. Anschließend wird der Einfluss verschiedener Verstimmungen systematisch auf die Leistung des VECSELs demonstriert: Bei der Veränderung der Verstimmung von -37 auf -20 nm lässt sich ein Anstieg der maximalen Ausgangsleistung um 70 % beobachten, während sich die Schwellenpumpleistung um den Faktor vier verändert. Zudem kann die Wellenlängen-Durchstimmbarkeit des VECSELs durch die Modifikation des intrakavitären Einfallswinkels auf dem Laserchip deutlich erhöht werden, was insbesondere für Anwendungen praktisch ist, welche eine erweiterte Wellenlängen-Zugänglichkeit erfordern.

Outline

1. Introduction

From the earliest times, light has been essential for the human civilization. After the birth of the modern science, the definition of light was extended from visible light, which covers a spectral range of electromagnetic radiation with wavelengths from 400 to 700 nm, to a much broader range, i.e. from gamma rays ($<10^{-12}$ m) to terahertz radiation (10^{-3} – 10^{-4} m). Yet, the significance of light is not only limited to illumination. A new kind of light source was demonstrated in the year 1960 by Theodore H. Maiman based on the fundamentals of quantum physics, which is referred to by its well-known acronym "laser", corresponding to "light amplification by stimulated emission of radiation" [1]. Today, lasers are employed for countless applications concerning people's daily life, for instance in the areas of industrial production, communication, projection and sensing technologies, and medicine. In the field of scientific research, lasers play an irreplaceable role in different domains such as spectroscopy, metrology, and laser cooling – thanks to their unique properties, which include high brightness, directionality, coherence, and monochromaticity.

As the exploration of the scientific frontiers advances further, new obstacles continue to emerge and require to be overcome by new types of lasers with novel features. In the mid-1990s, semiconductor lasers were well developed and widely used because of their advantages such as wide wavelength coverage, high energy efficiency, compact size, and low cost. However, it was difficult to obtain Watts-level output power with good beam quality from semiconductor lasers: The beam quality of the common edge emitters was limited by the waveguide, whereas the output power of the vertical-cavity surface-emitting lasers (VCSELs) in fundamental transverse mode was limited by the small mode size resulting from the short cavity length [2]. In order to solve this problem, researchers combined the geometry of solid-state disk lasers with the gain media of semiconductor lasers, and a new type of laser emerged. Since this kind of surface-emitting laser includes an external cavity, it is referred to as "vertical-external-cavity surface-emitting laser" (VECSEL) or "semiconductor disk laser" (SDL) [3], [4]. Thereafter, efforts have been devoted to the theoretical and experimental study of this new laser [5]–[8]. Indeed, VECSELs inherited the advantageous properties from both semiconductor and solid-state lasers. For instance, the output power in TEM_{00} mode operation from the very first VECSEL reached 0.5 W, which has been improved to over 20 W with excellent beam quality (M^2~1.1) in a later work [3], [9]. Moreover, thanks to the flexible external cavity, the potential of VECSELs has been explored by means of

developing different operation modes. In this thesis, we will focus on the single-frequency operation as well as dual-wavelength operation of VECSELs.

Single-frequency operation is achieved when the laser oscillates at only one resonate mode, that is, fundamental transverse mode, single longitudinal mode, and single polarization mode simultaneously. Therefore, when a laser is operated on a single frequency, its output exhibits the most excellent monochromaticity – that is to say, the "purest light" – of all light sources. Moreover, this feature entails low phase noise and narrow linewidth, which fulfill the crucial requirements for the high-precision measurements in the fields of interferometry, metrology, and spectroscopy [10]–[12]. A well-known example is the first observation of the gravitational waves announced on February 11, 2016 [13]. The detected gravitational-wave signal originates from the collision and merger of two black holes. The event is marked as a milestone in history since humans have finally found a way other than using electromagnetic radiation to study our universe. However, interestingly, the technique to detect the gravitational waves still relies on the utilization of light – to be specific, laser interferometry based on single-frequency Nd:YAG lasers [14]–[16]. Besides the extraordinary frequency stability, the applied single-frequency laser also provides 150 W output power to maximize the signal-to-noise ratio of the device. Similarly, high-power single-frequency laser sources are desirable for free-space communication since they do not require any redundant amplifier system. From the perspective of output power and beam quality, single-frequency VECSELs are promising candidates for the aforementioned applications. Additionally, the wavelength versatility of VECSELs provides the possibility to meet special requirements regarding the emission wavelength. To date, the highest output power from a single-frequency VECSEL is 23.6 W, which is also the record among all semiconductor single-frequency lasers [17]. The implementation of this device will be explained in chapter 3 of this thesis. There, we will also discuss the noise components affecting this laser and present a stabilized single-frequency VECSEL.

Although the emission wavelengths of VECSELs have covered a wide spectrum in the visible and infrared range, the wavelength accessibility can be further improved by means of frequency conversion in the feasible external cavity. In 2010, Scheller et al. demonstrated a room-temperature terahertz (THz) source based on a VECSEL operated on two clusters of laser modes, which is referred to as "dual-wavelength operation" [18]. A milliwatt-level THz signal was generated via intracavity difference-frequency generation (DFG). This report attracted the attention of both the THz and the laser community. The device was then systematically characterized regarding the key component – the dual-wavelength VECSEL [19]–[21]. Several works were dedicated to improve

the design of the dual-wavelength laser, aiming for high intracavity power as well as flexible wavelength-spacing [22]–[25]. In chapter 4 of this thesis, different approaches to implement dual-wavelength VECSELs will be discussed. A new cavity design – achieved by serially connecting two gain chips – will be promoted, followed by the analysis of its advantages and disadvantages [26]. Then the previous results of the THz emitting VECSEL will be reviewed. In the end of the chapter, the characterization will be complemented by the investigation of the beam quality of the emitted THz beam [27].

The single-frequency VECSEL and dual-wavelength VECSEL presented in chapters 3 and 4 both distinguish themselves from ordinary VECSELs by their high optical powers. A key parameter for expanding this advantage, namely the "detuning" of VECSELs, will be investigated in chapter 5. The detuning is the spectral difference between the material gain and the micro-cavity resonance. Since these two factors of the detuning stand in a linear relation to the modal gain of the device, the detuning has a significant influence on the performance of the laser, which was theoretically predicted by Hader et al. [28], [29]. However, due to the device-to-device fluctuation, it is difficult to directly examine the detuning-dependent performance difference of the gain chips with different detunings. In this work, a new approach will be promoted where the cavity angle of a V-shaped cavity is varied to change the detuning of a VECSEL chip. In this manner, the impact of the detuning will be experimentally demonstrated regarding the maximum output power, threshold, and emission wavelength.

2. Vertical-external-cavity Surface-emitting Lasers

As a member of the laser family, a functional VECSEL consists of three basic and essential components: a pump source, an optical resonator, and a gain medium [30]. The pump scheme of VECSELs is optical in most cases. For instance, a high-power semiconductor diode laser is employed, which is not required to be of very good beam quality. The optical resonator of VECSELs is completed by an on-chip distributed Bragg reflector (DBR) and one or more external cavity mirrors. The gain medium, which can consist of multiple quantum wells (MQWs) or quantum dots (QDs), is also integrated into the semiconductor chip. As shown in Fig. 2.1 (a), the cap layer, the DBR, the gain region, and the heat spreader together assemble the VECSEL chip. Fig. 2.1 (b) shows a real VECSEL chip included in this work, in size comparison to a one-cent coin. The grey area in the outer region of the chip mount represents the heat spreader, in this case, diamond grown by metalorganic chemical vapour deposition (MOCVD) with indium on top. The dark area in the middle of the mount comprises the semiconductor laser chip, with the DBR, gain region and cap layer aligned perpendicular to each other and to the diamonds surface. Although the DBR and the gain region have a total thickness of only a few micrometers, their performance is crucial to the laser. In chapters 2.1 and 2.2, the DBR structure and the gain region will be explained in detail. Based on this, the operation principle of a typical VECSEL will be summarized in chapter 2.3.

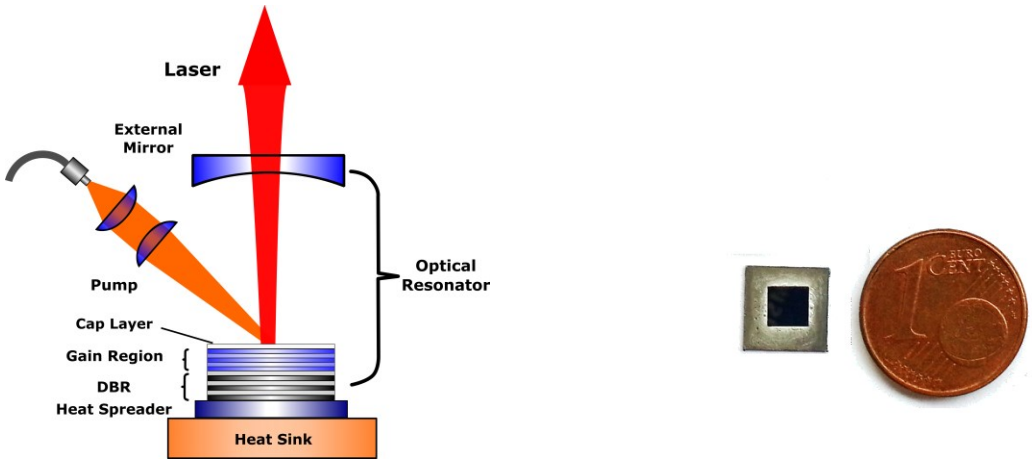

(a) (b)

Fig. 2.1. (a) A typical VECSEL setup consists of the gain chip, (here: linear) resonator, and optical pump scheme. (b) A photo of a mounted VECSEL chip used in this work in size comparison to a one-cent coin.

2.1 Distributed Bragg Reflector

The on-chip DBR structure performs as a compact high-reflectivity (HR) mirror. Together with the external mirror(s), the DBR completes the optical resonator. As shown in Fig. 2.2, a typical DBR is epitaxy-grown on the substrate by alternatively stacking two different kinds of thin films. The refractive indices are denoted as n_1 and n_2, respectively (a system with $n_1 < n_2$ is considered). The optical thickness of each layer matches a quarter of the design wavelength. Based on Fresnel's law of reflection, the incoming light will be partly reflected at each layer-layer interface. The light reflected at the interface between the materials coming from the side with lower refractive index experiences a 180-degree phase shift, while that reflected at the interface towards the lower-refractive-index layer experiences no phase shift. Considering interference at the layer boundaries, the reflection components are enhanced by constructive interference, whereas the transmission components are reduced by destructive interference.

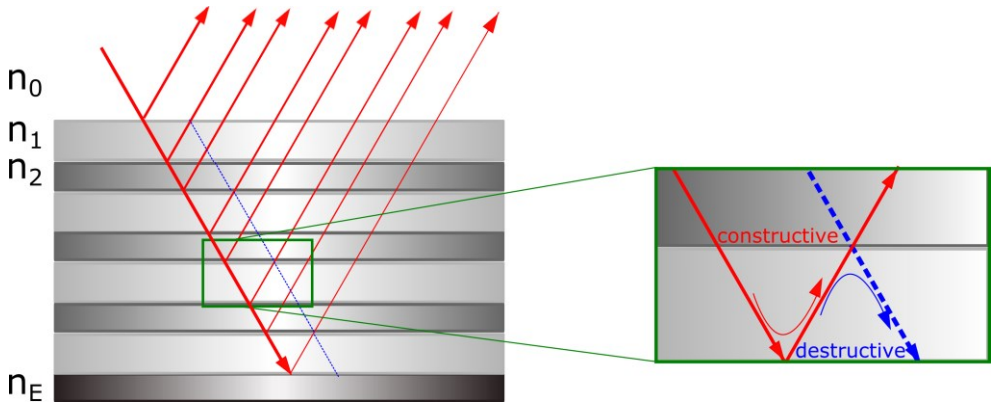

Fig. 2.2. The cross-section of a DBR structure. The zoom-in part illustrates the constructive interference of the reflection and the destructive interference of the transmission.

The total reflectivity of a DBR is given by

$$R_{tot} = \left[\frac{1 - \frac{n_0}{n_E}\left(\frac{n_1}{n_2}\right)^{2N}}{1 + \frac{n_0}{n_E}\left(\frac{n_1}{n_2}\right)^{2N}} \right]^2 \qquad (2.1),$$

where R_{tot} is the total reflectivity of the DBR; n_0 and n_E are the refractive indices of the entrance material and exit material, respectively; N is the number of layer pairs.

The bandwidth of a DBR is given by

$$\Delta\lambda = \frac{4\pi}{\lambda}\arcsin\left(\frac{1-\frac{n_1}{n_2}}{1+\frac{n_1}{n_2}}\right) \qquad (2.2),$$

where $\Delta\lambda$ is the bandwidth of a DBR; λ is the center wavelength of the incoming light. As we can see from Eq. (2.1), to obtain a high reflectivity from a DBR, the contrast between the refractive indices of the two kinds of material should be significant. Also, as shown in Eq. (2.2), a big contrast between n_1 and n_2 is able to provide a broad bandwidth. However, one has to consider the lattice constants of the two materials since it may cause practical problems during the epitaxy growth. For instance, for an interested wavelength around 1 μm the most widely used DBRs consist of AlAs/GaAs layer pairs, which have a n_1/n_2 ratio of 0.88 and a small lattice mismatch [31]. Regarding the choice of N, i.e. the number of layer pairs, it is clear that a larger N leads to a higher reflectivity. Yet, as the thickness of the DBR grows, its thermal impedance contributes more to that of the whole VECSEL structure, which hinders heat dissipation away from the gain region through the DBR to the heat sink. Therefore, the thickness of the DBR is an important factor concerning thermal management of the high-power VECSELs. For instance, in the work of Heinen et al., where a record-high optical output of 106 W has been produced from a single VECSEL chip, a DBR with 22.5 AlAs/GaAs layer pairs is used [32]. With a total thickness of around 4 μm, this DBR provides over 99.9% reflectivity and a bandwidth of over 100 nm, while exhibiting a good thermal conductivity of 32 W/mK [33]. In the case of some other material systems, the thermal impedance of the DBR could be significantly larger than that in the aforementioned case. To circumvent this problem, the thermal management strategy should be altered, as there is no standard design for both the DBR and the whole chip.

2.2 Gain Region

The gain region of VECSELs typically consists of multiple QWs or quantum dots QDs. QWs in semiconductors are formed of a layer of one material sandwiched between two layers of another material with a wider band gap (cf. Fig. 2.3). Theoretically, a QW is a potential well that is able to confine the particles (electrons and holes, in this case) into a two-dimensional region. The confinement effect forces the confined particles to exhibit discrete energy levels in the direction of

confinement, which is helpful for the generation of efficient laser emission as the density of states in lower-dimensional structures differ from the situation in bulk.

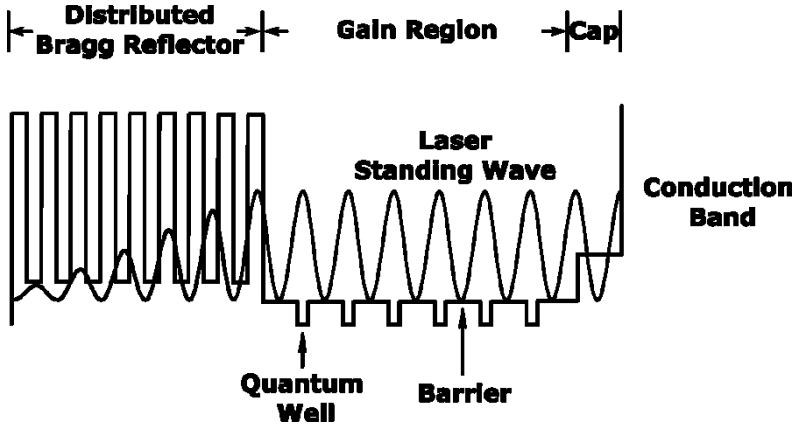

Fig. 2.3. The conduction band structure of a typical VECSEL chip and the standing wave formed in the micro-cavity.

The choice of the material for the QWs determines the emission wavelength of the device. By using epitaxy-grown QWs with different materials, it has been demonstrated that the fundamental emission wavelengths of VECSELs cover a wide spectral range, namely from about 0.6 μm in the red to 2.3 μm – even 5 μm – in the mid-infrared. The wavelength versatility provided by the QWs made of various material systems is shown in the following table.

Wavelength (μm)	0.67	0.85	0.98	1.03	1.32	1.55	2.00	2.35	5.00
QW material	AlGaInP	GaAs	InGaAs	InGaAs	GaInNAs	InGaAsP	GaInSb	GaInAsSb	PbTe
References	[34]	[35]	[36]	[32]	[37]	[38]	[39]	[40]	[41]

Table 2.1. Reported emission wavelengths of VECSELs corresponding to the materials of the QWs.

In order to provide enough gain to the laser, typically, multiple QWs are grown in the VECSEL structure. Increasing the number of QWs leads to a higher gain, while it is also increasing the lasing threshold [7]. From this point of view, one should incorporate a suitable amount of QWs into the gain structure of the VECSEL by considering the practical requirements and technical difficulties

at the design stage. For example, the VECSEL chip which produces record-high 106 W output power consists of 10 InGaAs QWs surrounded by GaAsP barriers [32].

The arrangement of the QWs is one of the most important factors for the performance of the VECSEL. Unlike in vertical-cavity surface-emitting-lasers (VCSELs), in VECSELs there is no second DBR structure on the top of the gain region. Yet due to the Fresnel reflection at the air-semiconductor interface, a Fabry-Pérot sub-cavity is formed in the VECSEL chip between the DBR and the cap layer. In this sub-cavity, the QWs are typically placed at the antinodes of the optical mode's electric field standing wave, while the standing wave typically reaches its maximum at the chip surface, as shown in Fig 2.3. Such arrangement is usually referred to as a resonant periodic gain (RPG) structure, which was first introduced to the VCSEL community in the end of the 1980s [42], [43]. Since the electric field of the interested light reaches its maximum at the positions of the QWs, the longitudinal confinement factor (LCF), which is defined as the proportion between the optical energy confined in the QWs and the total optical energy in the structure, is drastically enhanced [44]. The model gain of the device is then significantly increased, thanks to its linear dependence on the LCF. Indeed, the RPG structure has been successfully applied in many cases aiming for high output powers, including the aforementioned work that exceeded 100 W output power in CW multimode operation [45]. It is also worth noting that the spectral filtering effect of the sub-cavity, originating from the RPG arrangement, reduces the spectral width of the laser emission. This feature can be helpful to implement high-power single-frequency VECSELs [17].

In the resonant RPG structure, the LCF is typically enhanced and exhibited as a sharp peak in the spectrum [28]. As a consequence, the output power and the emission wavelength of the device are sensitive to the temperature change in the gain region since the LCF shifts spectrally with the temperature. Thus, it is very important to apply suitable thermal management techniques [33], [46], [47].

Although the resonant RPG arrangement is able to enhance the model gain, it may not be the best choice for VECSELs intended for other practical purposes. For instance, mode-locked VECSELs require a broad gain bandwidth to achieve mode-locked operation with short pulse duration, which can be hindered by the spectral narrowing that results from the RPG structure [48], [49]. Therefore, the VECSELs for mode-locked operation are usually designed as anti-resonant chips, which means that the standing wave of the sub-cavity is at its minimum at the chip surface, instead of at its maximum as in the aforementioned case. Besides the broad gain bandwidth, this arrangement also

provides a negligible group delay dispersion (GDD) in the chip, which is ideal for mode-locked operation [50]–[52].

2.3 Basic Operation Principle

Based on the aforementioned sections, the operation principle of an optically pumped VECSEL is explained in the following.

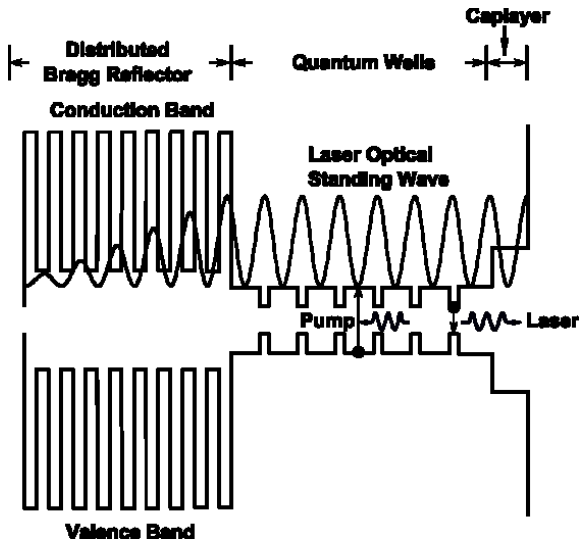

Fig. 2.4. The band structure of a VECSEL with RPG arrangement.

The pump beam induces photons with a higher energy than the bandgap of the barriers of the QWs in the gain region. Unlike solid-state disk lasers, the semiconductor materials exhibit a strong absorption for those photons, typically in the order of 10^{-4} cm^{-1} [7]. Therefore, single-pass pumping is sufficient in most cases. Subsequently, the carriers, in this case electrons and holes, are excited from the barriers and rapidly diffuse to QWs whose band gap is smaller than that of the barriers. This process is non-radiative and conveys a major part of the dissipated heat of the active region to the whole system. The confined carriers in the QWs have a certain probability of emitting photons through radiative recombination, which could be either spontaneous emission or stimulated emission. This provides the gain of the laser. In the meantime, the cap layer stops the carriers from diffusing to the chip-air interface. By using the RPG arrangement, the optical wave which is reflected by the DBR forms a standing wave between the DBR and the cap layer. The modal gain is doubled in comparison with a non-resonant structure [44]. The DBR and the external cavity mirror

form the optical resonator, which controls the transverse modes and the propagation direction of the laser. For instance, in a simple linear cavity with only one cavity mirror (cf. Fig. 2.1. (a)), fundamental transverse mode operation can be achieved, and the output laser beam emits perpendicularly from the chip surface. Typically, the gain in a single path in the thin chip is only a few percent. Hence, the transmission of the output cavity mirror is usually chosen to be on the same level in order to achieve the optimum output power.

3. Single-frequency Operation and Frequency Stabilization of VECSELs

A single-frequency laser operates on only one resonator mode, which is to say, fundamental transverse mode, single longitudinal mode, and single polarization mode simultaneously. The most attractive feature of this kind of lasers is their quasi-monochromatic laser output, which exhibits very low noise and therefore a very narrow linewidth. Thanks to this, single-frequency lasers are considered as irreplaceable components for applications in a wide range of areas, from spectroscopy to metrology, as well as in optical free-space telecommunication and laser cooling. With technology having advanced rapidly in recent years, higher demands have been placed on the single-frequency lasers regarding performance. For instance, narrower linewidth, higher power, broader tuning range as well as wavelength accessibility is sought, while the devices should become more compact and more cost-efficient.

As mentioned, VECSELs were invented to combine the good beam quality of disk lasers and the wavelength versatility of semiconductor lasers. Therefore, VECSELs are inherently designed for single-transverse-mode operation, which is already an important step to single-frequency operation, although multimode operation can be easily enforced. Additionally, the open cavity of the VECSEL ensures various methods to achieve single-longitudinal-mode as well as single-polarization-mode operation. Indeed, shortly after the invention of the first VECSEL [3], single-frequency operation and frequency stabilization were realized by Holm et al. in 1999, at an emission wavelength of 870 nm [53]. In the work at hand, the fundamental transverse mode operation is achieved by matching the pumped region with the TEM_{00} mode on the chip surface. Then, a piece of etalon as well as a Lyot filter, which is made of a stack of birefringent filters, are inserted in the Z-shaped cavity to confine the longitudinal modes and polarization modes. With an output power of 42 mW and a linewidth of 3 kHz, this work demonstrates the great potential of single-frequency VECSELs to the laser community. Thereafter, single-frequency VECSELs have been intensively investigated in view of different wavelength regions: In the visible range, Morton et al. successfully achieved single-frequency operation at 670 nm [34]; for around 1 µm single-frequency emission, several works with high output powers have been reported since GaAs/AlAs has become one of the most well developed material system for VECSELs [17], [54]–[57]; single-frequency laser emission at 1.5 µm was realized by Ratanmaki et al. [58]; single-frequency

VECSELs at 2.3 μm were also reported in several works as they can be employed for methane sensing [59]–[62].

Apart from the outstanding wavelength versatility mentioned above, a high output power is one of the most attractive features of single-frequency VECSELs. Thanks to the accessible external cavity, different wavelength selective elements, such as etalons [63], birefringent filters [17], gratings [64], or even the air-etalon formed between the VECSEL-chip and the external cavity mirror [59], can be used to achieve single-frequency operation. Until today, tens of watts output power with sub-MHz linewidth have been obtained from such high-power and highly coherent single-frequency VECSELs [17], [57]. On the other hand, with the help of frequency-stabilization techniques, VECSELs with kHz linewidth have been demonstrated [53], [60], [61], [65].

In this chapter, different methods to implement single-frequency VECSELs will be introduced, followed by an overview on the high-power devices. Then, the basics of frequency stabilization will be discussed and the results regarding frequency-stabilized VECSELs will be summarized.

3.1 Approaches to Achieve Single-frequency Operation

To understand single-frequency operation of lasers, the possible modes in a resonant cavity should first be considered. As it is shown in Fig. 3.1 (a), there are several standing waves along the axis of a resonant cavity, which are reinforced by constructive interference after many reflections from the cavity's reflecting surfaces. Those are the longitudinal modes of the cavity. The frequency difference of two neighboring modes is determined by the cavity length L (Fig. 3.1 (b)):

$$\Delta\nu_c = \frac{c}{2nL} \tag{3.1},$$

where c is the speed of light, n is the refractive index of the medium. The frequency of a longitudinal mode with an order of q is given by:

$$\nu = q\frac{c}{2nL} \tag{3.2}.$$

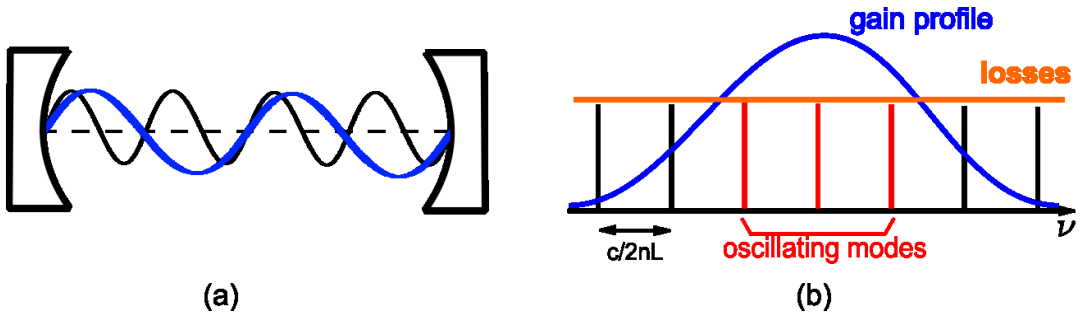

Fig. 3.1. (a) Two possible standing waves in a resonant cavity.
(b) Possible oscillating longitudinal modes of a laser.

In most free running solid state lasers and semiconductor lasers, the gain profile is as broad as several nanometers, as shown in Fig. 3.1(b). Thus, there can be many longitudinal modes located inside the gain profile, and they are the oscillating modes. In contrast, the other modes suffering more loss than gain are not able to oscillate.

Likewise, there are also several possible electromagnetic field patterns that can occur in the resonant cavity, due to the confinement in the plane perpendicular to the cavity axis. They are referred to as transverse modes and usually classified as TEM_{mn} modes, where m and n are integers and indicate the orders of the modes. If the resonant cavity has two mirrors with a radius of curvature r, the resonance frequency of a certain mode can be expressed as:

$$\nu_{qab} = \frac{c}{2nL}\left[q + (1+a+b)\frac{\arccos\left(1-\frac{L}{r}\right)}{\pi} \right] \qquad (3.3),$$

where q denotes the longitudinal mode number, a, b are the indices of the TEM orders, respectively, n is the refractive index of the medium, and L the cavity length. The higher order oscillating modes ($a+b\neq 0$) in a resonant cavity are plotted as Fig. (3.2):

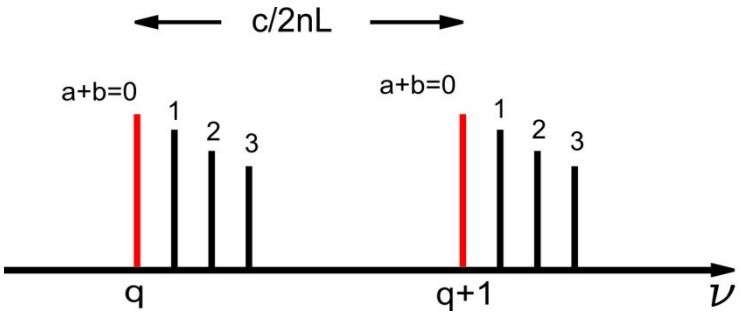

Fig. 3.2. Transverse modes (black) and longitudinal modes (red) in a typical resonant cavity.

For disk lasers, it is relatively easier to achieve a TEM_{00} mode compared to single-longitudinal-mode operation. This can be done by matching the pump region to the TEM_{00} mode size on the chip. The effect is a high gain for the fundamental transverse mode and a great loss for the higher order modes. Another approach to achieve a TEM_{00} mode uses the insertion of a pinhole with a small aperture at some point on the axis of the resonant cavity [66]. As the aperture decreases, the difference between the losses of the fundamental transverse mode and the higher order transverse modes increases. Thus, the higher order modes are suppressed, while the TEM_{00} mode is left nearly unaffected.

To achieve single-frequency operation after having maintained the laser operation at the fundamental transverse mode, methods to reach single longitudinal mode operation are required. The most commonly used methods include the insertion of intracavity elements (e.g., etalons, birefringent filters, and gratings) and the shortening of the cavity length. These methods will be introduced in detail in the following chapters.

3.1.1 Birefringent Filters (BRFs)

A birefringent filter (BRF) consists of a thin plate made of birefringent material, typically quartz. Usually, it is placed inside the laser cavity at Brewster's angle (θ_B) to the beam direction (cf. Fig. 3.3 (a)). Thus, a light with p-polarization (electric field polarized in the plane defined by the incident ray and the surface normal) will not be reflected, whereas s- and non-polarized light will be partially reflected. We assume, first, the incoming beam is p-polarized to the BRF. With the optical axis of the BRF being in the surface plane, the beam splits into two parts inside the BRF: ordinary ray and extraordinary ray. As it is shown in Fig. 3.3 (b), since the refractive indices for the two components, n_o and n_e, are different, the ordinary ray and the extraordinary ray experience different phase shifts inside the plate. The difference is given by:

$$\Delta\phi = \frac{2\pi}{\lambda}(n_e - n_o)d \qquad (3.4),$$

where λ is the wavelength of the beam and d is the thickness of the BRF.

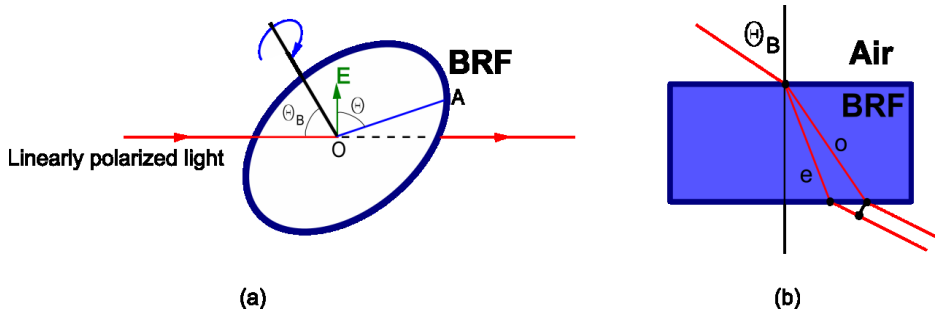

Fig. 3.3. Operation principle of a birefringent filter: (a) A linearly polarized light is incident on a BRF (blue circle) at Brewster's angle; (b) the o- and e-ray experience different refractive indices in the BRF.

After passing through the plate, unless $\Delta\Phi$ is an integer number of 2π, the two components combine to an elliptically polarized beam. Since the latter is inside the resonant cavity of a laser, it will return to the surface of the BRF after half a round trip. This time, there will be loss for the beam from the reflection, for it is not p-polarized any more. If the loss of a single round trip is higher than the gain, laser operation at this wavelength is not possible. If $\Delta\Phi$ is an integer number of 2π, the beam remains unchanged after passing through the BRF and therefore suffers no loss. In this way, the transmission spectrum exhibits a comb-like pattern over wavelength for a fixed angle between the optical axis (OA) (cf. θ in Fig. 3.3 (a)). For example, Fig. 3.4 presents a simulation for a 3-mm-thick quartz BRF at θ=45°.

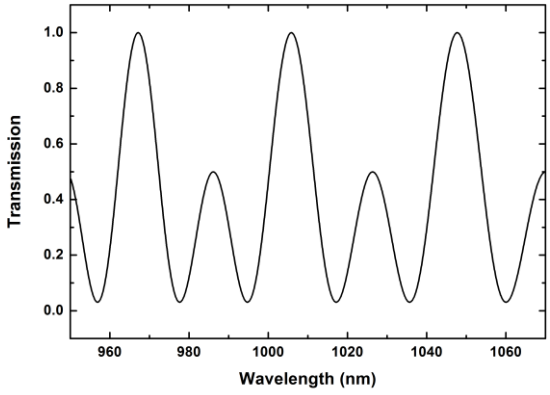

Fig. 3.4. Wavelength dependent transmission spectrum of a 3-mm-thick quartz BRF.

Assuming that $(n_e–n_o)$ does not change over the wavelength range of interest, the frequency difference between two neighboring transmission maxima is constant. This is commonly called free spectral range (FSR) of a BRF, which is given by:

$$\Delta\nu_{fsr} = \frac{c}{(n_e - n_o)d} \tag{3.5}$$

From Fig. 3.5 we can see that the free spectral range of the BRF $\Delta\nu_{fsr}$, in order to allow only one transmission peak of the BRF inside the gain profile of the laser, requires

$$\Delta\nu_{fsr} \geq \frac{\Delta\nu_{gain}}{2} \tag{3.6},$$

where $\Delta\nu_{gain}$ is the bandwidth of the gain profile.

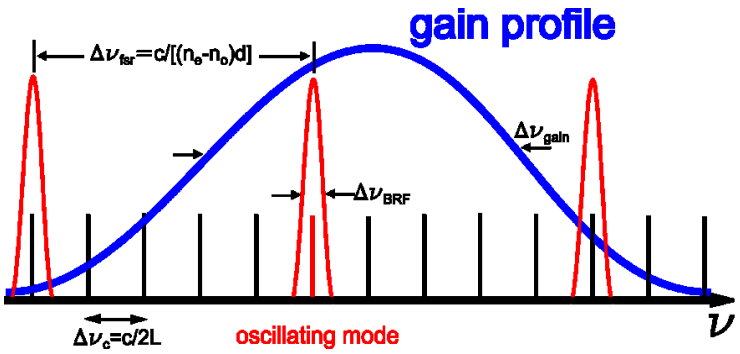

Fig. 3.5. Single longitudinal mode selected by a BRF in a broad gain profile.

Furthermore, the laser will be forced into single longitudinal mode operation if the transmission peak of the BRF overlaps with only one longitudinal mode inside the gain profile of the laser, which refers to the mode in red shown in Fig. 3.5. Similar to Eq. (3.6), the requirement is given by

$$\Delta\nu_{BRF} \leq 2\Delta\nu_{c} \tag{3.7},$$

where $\Delta\nu_c$ is the longitudinal mode spacing of the laser and $\Delta\nu_{BRF}$ is the bandwidth of the transmission peak of the BRF.

Besides its function as a wavelength selective element, another useful property of the BRF is the wavelength tunability. As n_e is a function of θ, the rotation of the BRF changes the difference between the phases of the o- and e-ray. The transmission peak of the BRF is therefore shifted. In this way, the laser spectrum is forced to shift with the transmission peak of the BRF from one longitudinal mode to another within the gain bandwidth, and thereby the laser wavelength is tuned. However, the sensitivity of the tuning is not only defined by the BRF itself but rather determined by the whole laser setup.

3.1.2 Etalons

Another kind of often-used intracavity element for single-frequency operation is etalon. It is also referred as Fabry-Pérot etalon since it shares the basic operation principles with the Fabry-Pérot

interferometer. An etalon consists of a parallel-plane plate made of transparent material, typically fused silica or glass for visible and NIR wavelengths. The two parallel surfaces are often coated with high-reflectivity coatings in order to obtain a better performance.

To understand the operation principle of the etalon, we can first assume that a plane wave with the electric field amplitude of E_0 is incident to the etalon at angle θ' to the normal of the two surfaces. As illustrated by Fig. 3.6, the electric field of the first transmitted beam is given by [67]:

$$E_1 = E_0 t_1 t_2 \exp(i\Phi') \tag{3.8},$$

where t_1 and t_2 are the transmissions of the electric field for the two surfaces respectively, and Φ' is the phase shift for the single pass through the etalon.

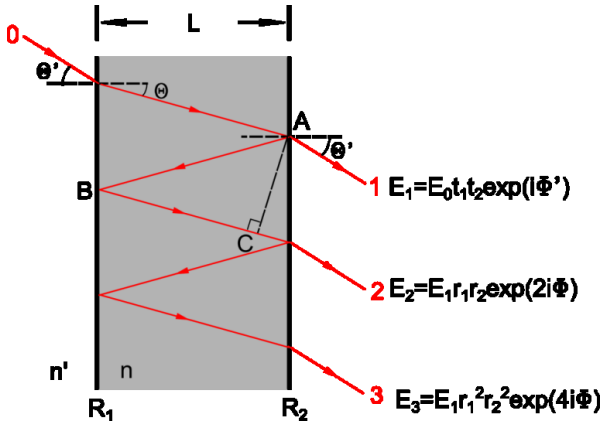

Fig. 3.6. Multiple reflections inside a Fabry-Pérot etalon.

For the second and third beam in the etalon, the electric fields are given by:

$$E_2 = E_1 r_1 r_2 \exp(2i\Phi) \tag{3.9},$$

$$E_3 = E_1 r_1^2 r_2^2 \exp(4i\Phi) \tag{3.10},$$

where r_1 and r_2 are the reflectivity of the electric field for the two surfaces respectively; 2Φ is the phase shift between two neighboring output beams, which can be written as

$$2\Phi = \frac{2\pi}{\lambda}(L_{AB} + L_{BC}) \tag{3.11},$$

where L_{AB} and L_{BC} are the lengths of AB and BC in the figure. Since θ can be given by the Snell's law,

$$n'\sin\Theta' = n\sin\Theta \tag{3.12},$$

we have:

$$\Phi = \frac{2\pi nL\cos\Theta}{\lambda} \tag{3.13},$$

where n and n' are the refractive indices of the etalon material and air, and λ is the wavelength of the beam. Taking all the output beams into account, the real output beam should be the sum of them. Thus, the total electric field is written as

$$E_{tot} = \sum_{l=1}^{\infty} E_l = [E_0 t_1 t_2 \exp(i\Phi')] \sum_{m=0}^{\infty} (r_1 r_2)^m \exp(2mi\Phi) \tag{3.14}.$$

The sum of the terms given in equation 3.14 can be evaluated by using

$$\sum_{m=0}^{\infty} q^m = \frac{1}{1-q} \tag{3.15},$$

where

$$0 < q = r_1 r_2 \exp(2mi\Phi) < 1 \tag{3.16}.$$

Hence we have

$$E_{tot} = E_0 \exp(i\Phi') \frac{t_1 t_2}{1-(r_1 r_2)\exp(2i\Phi)} \tag{3.17}.$$

Since the transmission of the power through the etalon is given by

$$T = \frac{|E_{tot}|^2}{|E_0|^2} \tag{3.18},$$

and for both surfaces $r_1^2=R_1$, $r_2^2=R_2$, $t_1^2=T_1=1-R_1$, $t_2^2=T_2=1-R_2$ we obtain

$$T = \frac{(1-R_1)(1-R_2)}{\left[1-(R_1R_2)^{1/2}\right]^2 + 4(R_1R_2)^{1/2}\sin^2\Phi} \tag{3.19}.$$

From Eq. (3.19) and Eq. (3.13) we are able to plot the transmission spectrum over frequency with different surface reflectivity of etalons. Fig. 3.7 shows that the transmission spectrum for a certain etalon is comb-like, which is similar to what we have already seen in chapter 3.1.1.

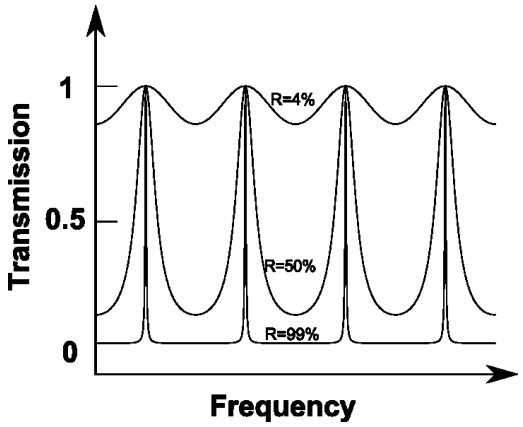

Fig. 3.7. Transmission spectrum over frequency of etalons with different surface reflectivity.

The evenly spaced transmission maxima are reached when $\sin^2\Phi=0$. Thus, the frequencies of the transmission maxima are given by

$$\nu_q = q\frac{c}{2nL} \tag{3.20},$$

where q is an integer number; n is the refractive index of the etalon material; L is the thickness of the etalon. Similarly to that of a BRF, the frequency difference between two neighboring transmission maxima is defined as the free spectral range of the etalon and it is given by

$$\Delta\nu_{fsr} = \frac{c}{2nL} \tag{3.21}.$$

To make sure that there is only one transmission peak in the range of the gain, the free spectral range of the etalon should satisfy

$$\Delta\nu_{fsr} \geq \frac{\Delta\nu_{gain}}{2} \tag{3.22},$$

where $\Delta\nu_{gain}$ is the gain bandwidth of the laser.

In order to calculate the bandwidth of the transmission peak, we assume that the reflectivity of the surface is high enough, which is to say $R_1=R_2\approx 1$. Also, from the half to the top of the peak, there is only a negligible change of Φ, which means $\Phi<<\pi$. Hence we have $\sin\Delta\Phi\approx\Delta\Phi$. As $T(\Delta\Phi)=0.5T$, we obtain

$$\Delta\Phi = \pm\frac{[1-(R_1R_2)^{1/2}]}{2(R_1R_2)^{1/4}} \tag{3.23}.$$

Because of the symmetrical shape of the peak, the full width of the peak can be expressed as

$$\Delta\Phi_{eta} = \frac{[1-(R_1R_2)^{1/2}]}{(R_1R_2)^{1/4}} \tag{3.24}.$$

In equation 3.13, as the incident angle θ is small, we obtain the bandwidth of the etalon in frequency

$$\Delta\nu_{eta} = \frac{c}{2nL}\frac{1-(R_1R_2)^{1/2}}{\pi(R_1R_2)^{1/4}} \tag{3.25}.$$

Equation 3.23 shows that for a certain etalon, the bandwidth is determined by the reflectivity of both its surfaces. This can also be seen from figure 3.7, where higher reflectivity leads to sharper transmission peaks [68].

Similarly to the discussion of birefringent filters, the requirement for only one longitudinal mode of the laser to overlap with one transmission peak is

$$\Delta\nu_{eta} \leq 2\Delta\nu_c \tag{3.26},$$

where $\Delta\nu_c$ is the longitudinal mode spacing of the laser. If both equations 3.20 and 3.24 are satisfied, only one longitudinal mode of the laser is allowed to oscillate in the gain profile (cf. Fig. 3.5). In this way, the laser can be forced into single-longitudinal-mode operation. Therefore, a thin etalon can be employed to obtain a large free spectral range, and both its surfaces can be coated with high-reflectivity coating to narrow the bandwidth.

3.1.3 Gratings

An ideal grating can be considered as a plane with a set of evenly spaced slits on it. According to the Huygens-Fresnel principle, each point on the wavefront of a propagating wave can be considered to act as a point source, and the wavefront at any subsequent point can be found by adding together the contributions from each of these individual point sources. Thus, when a plane wave with wavelength λ is incident on the grating, the slits work as point sources from which the light propagates into all directions. At any point in space, the lights from different slits may interference. When the path difference between the lights from neighboring slits is integer times of λ, constructive interference will occur. If θ_m is defined as the angle between the diffracted beam and the grating's normal factor, the maxima due to constructive interference occurs when

$$d \sin\theta_m = m\lambda \tag{3.27},$$

where d is the spacing between two neighboring slits; m is an integer and usually referred to the diffraction order. For an incident plane wave with incident angle of θ_i, the equation is given by

$$d\left(\sin\theta_m + \sin\theta_i\right) = m\lambda \tag{3.28}.$$

Then we obtain the diffracted angle θ_m as a function of λ:

$$\theta_m = \arcsin\left(\frac{m\lambda}{d} - \sin\theta_i\right) \tag{3.29}.$$

Equation 3.29 shows the dispersive character of gratings, i.e., gratings are able to separate the incident light into different wavelength components.

In practice, the slits can be replaced by any regular structure with the same spacing since the phase relationship between light scattered from the neighboring structures of the grating remains the same. When a grating is used as an intracavity element, as it is shown in Fig. 3.8, only the light with the wavelength that satisfies Eq. (3.29) can oscillate in the resonant cavity, while other lights suffer losses due to their different diffracted angles.

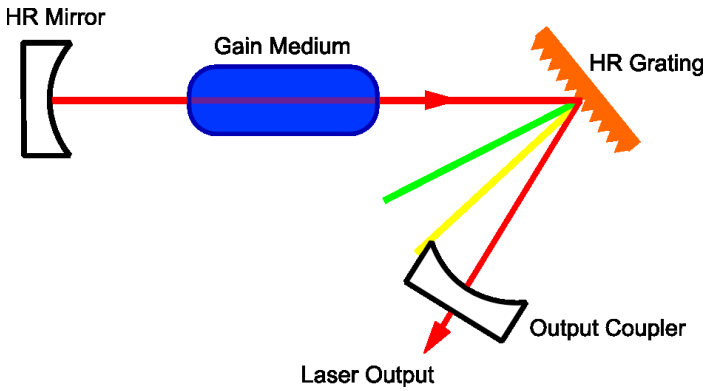

Fig. 3.8. High reflectivity grating as wavelength selective element in a laser setup.

In order to achieve single-frequency operation and obtain narrow linewidth laser emission, the resolution of the grating is required to be high. Since the resolution is proportional to the number of the slits, it is necessary to arrange the slits as closely as possible. For instance, approach has been made to form a 20 nm deep and 520 nm period grating by reactive ion etching (RIE) on a dielectric mirror [69]. With an incident angle of 7.64°, this results in a narrow peak (peak width narrower than 1 nm) with reflectivity over 99% at 1058 nm. In this work, single-longitudinal-mode emission with a linewidth of 90MHz is obtained.

However, the main drawback of gratings lies in the relatively high loss due to scattering. Thus, this method may be not ideal for the lasers with low round-trip gain. Furthermore, from the example above we can see that the high reflectivity grating must be carefully designed and fabricated. Consequently, the cost of a high-reflectivity grating is usually much higher than that of the BRFs and etalons.

3.1.4 Short Cavity Method

Apart from the intracavity elements mentioned previously, there are other methods to achieve single-longitudinal-mode operation of VECSELs. In 2005, Ouvrard et al. presented a single-frequency VECSEL at 2.3 μm with a cavity length of 15 mm [59]. Since the spacing of the longitudinal modes is inversely proportional to the cavity length (cf. Eq. (3.1)), the short cavity length leads to a large longitudinal-mode spacing. When the mode spacing is increased to such a value so that only one mode locates inside the gain profile, single-longitudinal-mode operation will be achieved naturally and no intracavity filter is required. Apart from laser emission with narrow linewidth, this method also provides the possibility for very compact laser systems. For instance, in 2008, Garnache et al. demonstrated a very compact single-frequency VECSEL with a cavity length of only 9 mm [70].

However, the short-cavity design results in a small fundamental transverse mode on the VECSEL chip surface, e.g., 40-100 μm in diameter in the cases of Ref [59] and [70]. The relatively small gain volume makes it difficult for the device to produce high output power under single-frequency operation. One way to circumvent this problem was proposed in 2010 by Laurain et al., who completed the external cavity with a flat mirror. Thanks to the positive thermal lens introduced by the pumping, the authors were able to use a pump spot of 233 μm in diameter to achieve fundamental transverse mode operation. Consequently, the output power was elevated to 2.1 W [71], [72].

3.2 High-power Single-frequency VECSELs

Considering that single-frequency VECSELs inherited a part of their device design from solid-state disk lasers, they have been expected to produce high output powers since the beginning of their invention. Indeed, researchers have been striving to achieve higher output powers in different

spectral regions. Table 3.1 shows the highest output powers to date from single-frequency VECSELs at different emission wavelengths.

Wavelength (nm)	Output Power (W)	Sampling time (s)	Linewidth (kHz)	Year	Reference
678	0.01	NA	200	2007	[73]
852	0.017	NA	300	2008	[63]
1013	23.6	100 μs	88	2014	[17]
1050	4.6	27 ms	75	2012	[55]
1180	11	NA	NA	2013	[56]
1560	1	NA	13	2013	[74]
2300	1.1	100 μs	20	2013	[62]

Table 3.1. The highest output powers from single-frequency VECSELs at different emission wavelengths.

From this table we can see that the highest single-frequency output powers range from 10 mW and 17 mW at 678 nm and 852 nm to 11 W and 23 W at 1013 nm and 1180 nm. This huge difference reflects the difference of the highest model gain at those wavelengths. For instance, for multimode-red-emitting VECSELs, an output power of only 1.2 W has been reported at a very low temperature of -31 degrees, while in the NIR region 106 W multimode output power has been achieved at 3 degree. That is to say, the achievable single-frequency output power is usually correlated to the highest multimode output power. Regarding the reason, as has been pointed out in chapter 3.1: To achieve single-frequency operation, only TEM_{00} mode is allowed, which requires a pump spot no larger than the fundamental transverse mode on the chip surface. Therefore, the gain volume is smaller than that in multimode operation. Furthermore, in order to limit the laser to single longitudinal mode, it is necessary to introduce losses to suppress the undesired longitudinal modes, e.g., by means of inserting intracavity elements. Consequently, the single-frequency output power is always reduced from the power level of multimode operation. From this perspective, we can see the difficulty lying in the way to high-power single-frequency VECSELs: On the one hand, a high modal gain is required in order to produce high power; on the other hand, the high modal usually results in multiple modes rather than a single mode oscillating in the cavity, which should be suppressed by more loss. Hence, the key consideration for high-power single-frequency devices is how to make the trade-off between the gain and the loss.

As an example, we will here present the considerations taken in the work where the record-high 23.6 W single-frequency output power has been achieved [17]. The gain chip employed in this

work has the same design regarding the gain region and DBR as the one that produced 106 W output power in multimode operation. The chip is placed in a V-shaped cavity and acts as a folding mirror, as shown in Fig. 3.9. In such a cavity, the photons travel through the gain region four times in one round-trip, which is twice as often as in a cavity where the chip serves as an end mirror [75] – that is to say, the round-trip gain is doubled. The 140 mm long cavity results in a TEM_{00} mode of 630 µm in diameter on the chip surface. The pumped area is approximately 500 µm in diameter. On the one hand, it is 20% smaller than the TEM_{00} mode, which is able to ensure the fundamental transverse mode operation. On the other hand, for this particular chip, the pumped area is the largest spot that will not trigger lateral lasing [76]. Hence, in terms of the gain, we use a large gain volume of a high-gain chip in a double-pass cavity configuration. In order to introduce the proper amount of loss to the system, an output coupler with 5% transmission is chosen. The relatively high transmittance of the resonator also grants high-percentage output. A 10 mm thick BRF is inserted in the long arm of the cavity at its Brewster's angle to confine the longitudinal modes. Since no further frequency-selective elements are employed, the intracavity scattering losses and absorption are kept to the minimum.

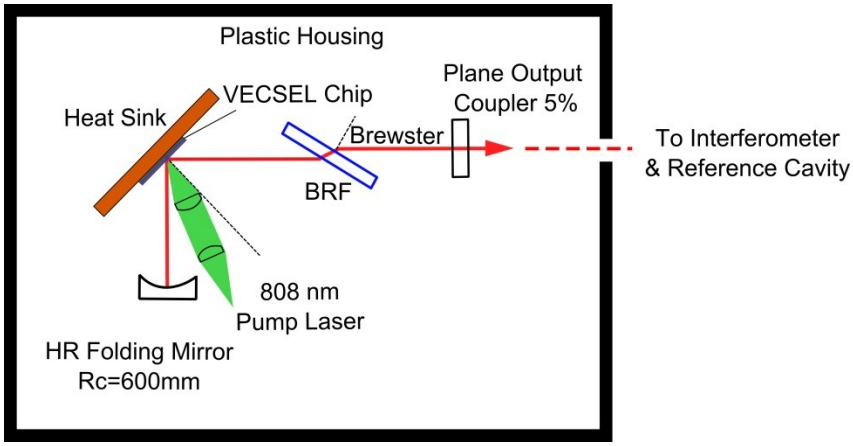

Fig. 3.9. Schematic drawing of the single-frequency VECSEL setup which produces over 23 W output power [17].

Indeed, the high-power single-frequency devices are considered as very promising candidates in many application fields. For instance, the high intensity output with very narrow spectral linewidth can be used to create an artificial star image in the outer atmosphere [77]. Referred to as "Laser guide star", it serves as a wavefront reference source in order to correct atmospheric distortion of light [78]. In the area of free-space communication, single-frequency lasers with tens of Watts of output power are also desirable since, in this case, the amplifier is no longer necessary.

3.3 Frequency Stabilization

Ideally, a single-frequency laser emits a perfect sinusoidal oscillation of the electric field at its output and an infinitely narrow linewidth. However, due to the random phase of photons added by the spontaneous emission, there is a fundamental limit to the laser linewidth, which is referred to as the Schawlow-Townes linewidth, given by [79]:

$$\Delta\nu_{Laser} = \frac{4\pi h\nu}{P_{out}}(\Delta\nu)^2 \tag{3.30},$$

where $\Delta\nu$ is the half bandwidth of the resonance at half maximum intensity, and P is the output power. Yet, for most lasers, this fundamental limitation level is fairly low. For instance, for a free-running 15 W single-frequency VECSEL, the spectral density of frequency noise induced by the Schawlow-Townes limit is less than 10^{-10} of that by the pump induced thermal fluctuation below 100 kHz [65]. Hence, the real laser linewidth of a single-frequency laser is dominated by technical noises, such as acoustic noises, mechanical vibrations, and thermal fluctuations. To take the example of the work demonstrating the 23 W single-frequency VECSEL: Here, the linewidth is deduced at different sampling time by Allan deviation [80]. As the sampling time increases, different kinds of technical noises start to broaden the laser linewidth. The linewidth over the sampling time is plotted in Fig. 3.10. Here, the two steep slopes in the curve indicate two major sources of noise: For sampling times ranging from approximately 1 ms to 10 ms (cf. the blue area in the figure), the fast increment of the linewidth is caused by the acoustic and mechanical noise from the water cooling system, which locates in the millisecond domain; for sampling times longer than 0.1 second, it is the thermal fluctuation in the setup that causes the increment.

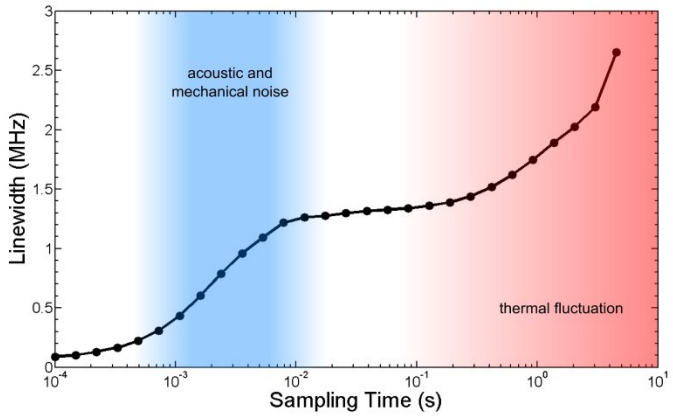

Fig. 3.10. Laser linewidth of a free-running single-frequency laser as a function of the sampling time [17].

Since many applications require lasers with narrow linewidth, it is desirable to suppress the technical noises by frequency stabilization. Typically, the frequency stabilization techniques can be divided into two types: passive and active. For passive frequency stabilizations, the equipment and techniques are applied to the laser setup to reduce the ambient noises and suppress the long-time frequency drift. For instance, components made of stiff material can be used to reduce the mechanical vibration; the setup can be sealed in a box, or even a vacuum housing, where the acoustic noise, the environmental thermal fluctuation, and the air pressure change can be well isolated. Although passive frequency stabilization is able to lower the noise level and slow the frequency-drift rate, it cannot correct the existing error of the lasing frequency.

This is where active frequency stabilizations come into play. The active frequency stabilization techniques typically employ a feedback loop, which is shown in Fig. 3.11 [81]. Here, the laser goes through a reference, detected by a detector, and generates an error signal, which is usually an electronic signal and represents the difference between the current laser frequency and the desired frequency. After the error signal has been fed into the electronic servo control, the latter will manipulate the parameters of the laser to actively correct the lasing frequency.

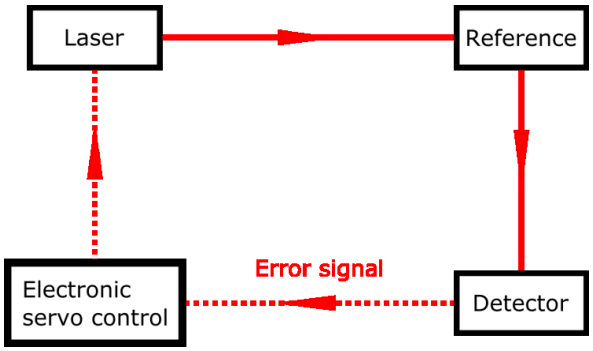

Fig. 3.11. A feedback loop for laser frequency stabilization. The solid red lines indicate optical paths, while the dotted red lines represent electronic signals.

Fig. 3.12 shows the schematic drawing of our frequency-stabilized single-frequency VECSEL, with stabilization being achieved both passively and actively. In terms of passive stabilization techniques, the laser setup is surrounded by a plastic housing, which has walls of 20 mm thickness, so that it is well isolated from the ambient acoustic and thermal noises. Soft pipes are employed in order to minimize the mechanical vibration coupled from the water cooling system to the laser. To additionally implement active frequency stabilization, a Fabry-Pérot cavity is set up as frequency reference. Assuming the desirable frequency is at half of the slope of the transmission peak, a drift of the laser frequency will be reflected as a change of the transmission amplitude (cf. Fig. 3.7). That is to say, by measuring the transmitted laser power after the reference cavity, the variation of the laser frequency can be determined. To improve the stability, the reference cavity is also sealed in a plastic housing similar to that of the laser cavity. The finesse of the reference cavity is set to 100, which provides a moderate slope of the transmission peak. Part of the laser beam propagates through a tunable attenuator and is measured by a photodiode. In this way, the locking point of the reference cavity is set to half of the transmission peak. The advantage of this method is that the output power fluctuation of the laser has the same influence on the measurement results of the two diodes, which means the power fluctuation does not affect the frequency reference. Then, the signals from the two diodes are fed into a universal Proportional-Integral-Derivative (PID) controller, which generates the error signal. According to the error signal, a piezo controller drives the piezo transducer, on which a cavity mirror of the laser is mounted, to change the laser cavity length. Consequently, the drifted laser signal is pulled back to the locking point.

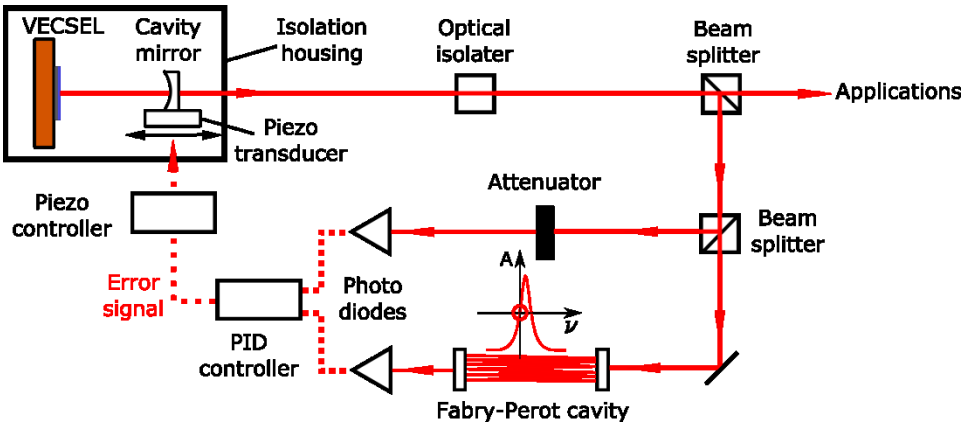

Fig. 3.12. Schematic drawing of a frequency-stabilized single-frequency VECSEL. The solid red lines indicate optical paths, while the dotted red lines represent electronic signals.

To demonstrate the results of the frequency stabilization, the transmitted signal after the reference cavity is recorded to analyze the stabilized laser linewidth. Fig. 3.13 (a) shows that when the active stabilization is not employed, the signal drifts randomly in a wide range over 15 seconds. After active stabilization is applied, the drift of the signal is eliminated and the laser is locked for over 20 seconds, as shown in Fig. 3.13 (b).

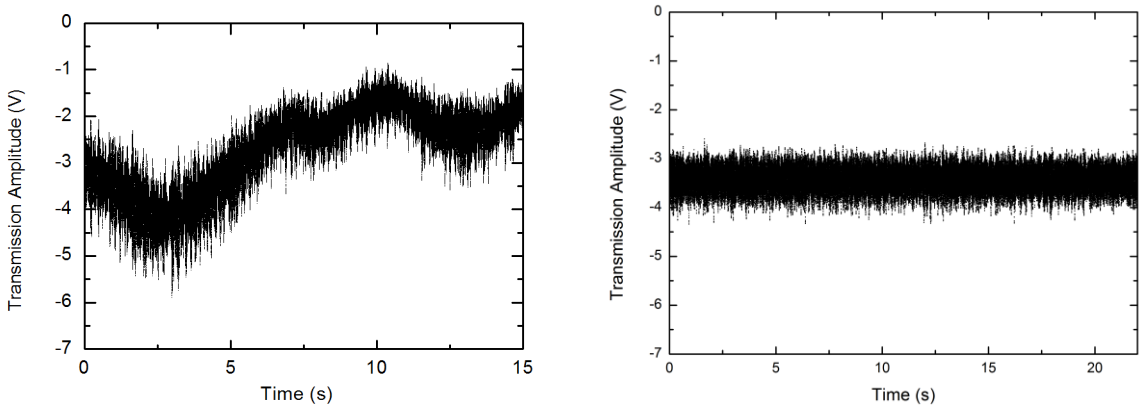

(a) (b)

Fig. 3.13. The transmission signal from the reference cavity (a) when active stabilization is not applied and (b) after active stabilization is applied.

For comparison, the actively stabilized signal is also characterized when passive stabilization is reduced, by removing the isolation housing around the laser setup. Similar to the case in Fig. 3.10, Allan deviation is applied to deduce the laser linewidth at different sampling times for the actively stabilized VECSEL, for the passively stabilized VECSEL as well as for the both actively and passively stabilized VECSEL [17], [80]. Fig. 3.14 shows that at sampling times ranging from 10^{-4} s to 1 s, passive stabilization results in a linewidth (blue curve) that is 30% narrower than that of the

active stabilization (green curve). This indicates that the noises in the range from 10 kHz to 1 Hz are strongly reduced by passive stabilization, whereas active stabilization is not equally effective in this range. However, since the passive technique cannot correct the existing error, the drift of the laser frequency increases drastically for sampling times longer than 1 s, which can be attributed to the thermal fluctuation [62]. Yet, as active stabilization is able to stop the frequency drift, the linewidth of the actively stabilized laser remains around 3.5 MHz. The red curve in Fig. 3.14 represents the laser linewidth when the laser is both actively and passively stabilized. By comparing the red curve to the green one, we notice the linewidth can be narrowed by over 50% at all sampling times, which confirms the importance of passive stabilization. For the red and blue curves, the linewidths at sampling times between 10^{-4} s and 10^{-3} s are quite similar, whereas the difference between them starts emerging from 10^{-3} s and keeps increasing as the sampling time extends. Hence, we can see that active stabilization is able to effectively narrow the laser linewidth at a response frequency of 1 kHz and lower. This frequency is limited by the response speed of the piezo transducer and its corresponding electronics.

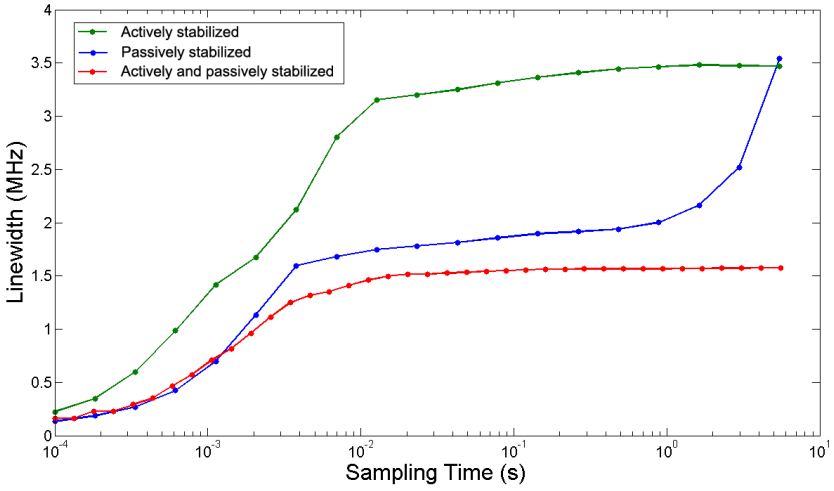

Fig. 3.14. Laser linewidth at different sampling times for the actively stabilized VECSEL, for the passively stabilized VECSEL as well as for the both actively and passively stabilized VECSEL, respectively.

To summarize, in order to obtain a narrow laser linewidth from a single-frequency VECSEL, suitable passive stabilization techniques should first be applied to reduce the ground noise level. Based on this, active stabilization can be employed to stop the frequency drift and to further narrow the linewidth. The dynamic range of active stabilization is usually limited by the hardware, whereas the susceptibility is determined by the specific method to generate the error signal. For future work, more advanced techniques for active stabilization can be employed, such as the Hänsch-Couillaud

method and Pound-Drever-Hall method to achieve VECSELs with kHz, even sub-kHz, linewidth [82], [83].

4. Dual-wavelength and Terahertz Emitting VECSELs

The development of the VECSELs has drawn more and more attention, thanks to their applicability. For instance, the open cavity design grants VECSELs the possibilities to employ intracavity elements, e.g., frequency selective filters and non-linear crystals, etc. Also considering the excellent beam quality and the achievable high intracavity power, VECSELs are recognized as promising candidates for different types of intracavity frequency conversion schemes [84]–[89]. Especially in the fields of terahertz technology, where many applications are expected [90]–[94], a term is named as "THz gap", which refers to the difficulty to generate, manipulate and detect the THz radiation between 0.1 and 10 THz [95]. Since the current approaches among the microwave technologies in the lower frequencies of the electromagnetic spectrum all exhibit certain practical drawbacks, researchers attempt to overcome this obstacle with the help of difference-frequency generation (DFG) in the optical regime. As DFG requires two different well-spaced frequencies available in a nonlinear crystal, it would be desirable that VECSELs are able to operate on two frequencies simultaneously. Furthermore, in terms of applications, an ideal dual-wavelength VECSELs should also include key features such as high-power efficient room-temperature operation, compactness, cost-effectiveness etc. Indeed, a great amount of efforts have been made to reach these goals. In 2010, Scheller et al. demonstrated the first THz-emitting VECSEL – referred to as "TECSEL", based on DFG in a dual-wavelength VECSEL [18]. At room temperature, milliwatt-level THz power has been reported from this work, which attracts the attention from both the THz and the VECSEL community. Thereafter, several investigations have been performed to characterize the performance of the TECSEL and to improve its design and its features [19]–[21], [96].

In this chapter, different approaches to implement dual-wavelength VECSELs will be introduced and compared. Alternative dual-wavelength concepts will be considered with the aim to improve DFG from VECSELs. With respect to THz emission, we will revisit the previously achieved TECSEL concept. The existing characterization of the TECSELs will be complemented by the recent study of the beam quality of the THz signal generated from intra-cavity DFG in a periodically-poled lithium niobate (PPLN) crystal.

4.1 Approaches to Implement Dual-wavelength VECSELs

4.1.1 Intracavity Etalon Approach

In section 3.1.2 we have discussed the properties of an etalon as frequency selective element. Similar to the case of single-frequency operation, the etalon is inserted in the external cavity to control the longitudinal modes. For single-frequency operation, only one transmission peak of the etalon is allowed in the gain spectrum of the VECSEL (cf. Fig. 3.5). In the case of dual-wavelength operation, the gain profile of the gain chip should be broader than the FSR of the etalon, in order to cover two transmission peaks. However, it should be narrow enough with respect to the magnitude of two FSR, in order to prevent oscillation of three wavelengths in the resonator. With a proper etalon fulfilling this requirement, dual-wavelength operation is relatively easy to implement in this manner. The first realization of this approach was shown by Fan et al in 2007 [75]. As shown in Fig. 4.1, a 150-µm-thick etalon is employed to create a wavelength separation of 2.1 nm. It is also worth noting, that a Brewster window is inserted in the cavity for polarization control. The dual-wavelength laser is therefore linearly polarized, which is ideal for type-I frequency conversion.

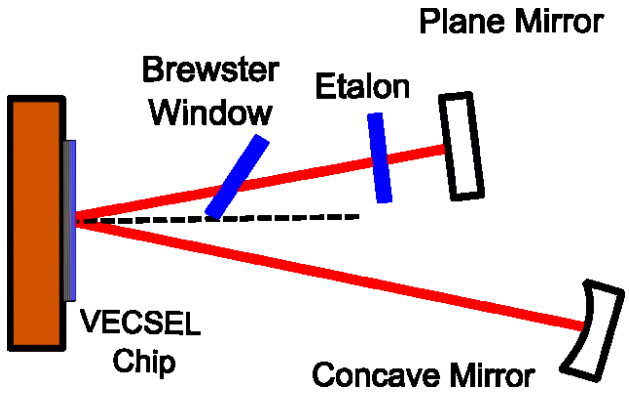

Fig. 4.1. Schematic drawing of a dual-wavelength VECSEL achieved with an intracavity etalon.

Thanks to its simplicity, this approach has been applied to the first TECSEL, which was demonstrated as a compact, room-temperature, and high-power CW THz source by Scheller et al. [18]. Thereafter, several works have been conducted to characterize and improve the design, including the study of the dynamics in the dual-wavelength regime [19]–[21]. This investigation points out that each emission wavelength of a two-color output contains several modes, and that the stability of the two wavelengths relies on the number of the modes. That is to say, in order to

produce stable dual-wavelength emission, the spectral width of each color should be as broad as possible. Hence, in terms of THz generation, it is hard to provide THz signal with narrow linewidth with this approach, since THz radiation is generated by mixing the two wavelengths in a nonlinear crystal. Another limitation of this design is given by the fact that only one gain chip is employed. On the one hand, one chip sets the upper limit to the achievable intracavity power. On the other hand, the gain bandwidth of one single chip is only a few nanometers, which makes it impossible to achieve dual-wavelength operation with a wider spectral separation than the gain bandwidth of that chip.

4.1.2 Dual-gain-region VECSELs

Aiming for intracavity frequency conversion, the ideal dual-wavelength laser should provide two coaxial emission wavelengths simultaneously oscillating in the same resonator. The number of the intracavity elements should be kept at a minimum, since the losses introduced by them will decrease the achievable intracavity circulating power. Therefore researchers brought forth the idea to integrate two lasers with different emission wavelengths into one. Indeed, in 2004 Morozov et al. presented a theoretical model, where two different kinds of quantum wells are arranged in one VECSEL chip [88]. Shortly afterward, the design was realized by Leinonen et al. [97]. The band structure of the specific gain chip is shown as Fig. 4.2. Four quantum wells made of $In_{0.17}Ga_{0.83}As$ are located in section I and III, emitting short wavelength λ_S, while four quantum wells of $In_{0.23}Ga_{0.77}As$ in section II, emitting long wavelength λ_L. The quantum wells for λ_L are placed at nodes of the standing wave profile of λ_S, in order to minimize the absorption of λ_S. Two blocking layers are grown at the boundaries of the sections to avoid the dissipation of carriers in sections I and III by flowing from the shallow quantum wells to the deep ones.

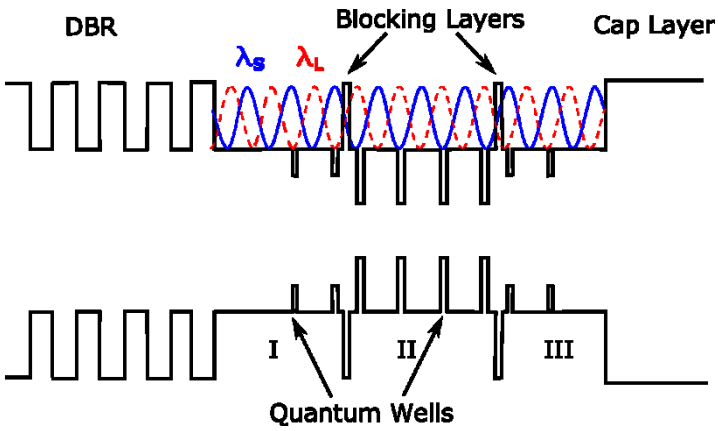

Fig. 4.2. Band structure diagram of a gain chip with two types of quantum wells [22]. The solid blue line indicates the standing wave form of the short wavelength, while the red dotted line for that of the long wavelength.

In this work, an output of 140 mW was obtained for λ_S =984 nm and 115 mW for λ_L =1042 nm. Two years later, with a similar design, the output power was pushed to Watts-level, which is 0.75 W at λ_S =966 nm and 1.38 W at λ_L =1047 nm [22]. Compared to other approaches to achieve dual-wavelength operation, also considering the low efficiency of intracavity conversion, the output power is not quite satisfying. Moreover, this approach requires a very precise chip design to produce two emission wavelengths with comparable powers. For the growth of the chip, molecular beam epitaxy (MBE) with very accurate control of the growth rate (better than 1 %) is usually required [98]. Although the two emission wavelengths are not tunable for a specific chip, this approach shows its potential as a compact dual-wavelength laser.

4.1.3 T-shaped Cavity Dual-chip Device

Considering the relatively low efficiency of difference-frequency generation in a nonlinear crystal, it is desirable that the dual-wavelength lasers are able to provide high optical powers. Hence, a two-chip design comes into consideration in the VECSEL field. On the one hand, two employed chips leads to a larger gain volume than a single chip, which means higher gain for the system. On the other hand, with two chips it is possible to distribute the excessive heat generated during the laser operation into two heat sinks, which offers a better thermal management than in the single chip design for the same total pump power. The two-chip configuration was first realized in 2012 by Hessenius et al. [99]. As shown in Fig. 4.3, two individual cavities are combined by a polarizing beam splitter (PBS) to form a T-shaped cavity. A piece of BRF is placed at its Brewster's angle in

the linear cavity, in order to produce p-polarized emission (λ_1). Another BRF is located at its Brewster's angle in the other plane of the L-shaped cavity, which results in s-polarized emission (λ_2). After propagating through the PBS and being reflected by the PBS, the p- and s-polarized beams, respectively, overlap with each other in the resonator section between the PBS and the concave mirror.

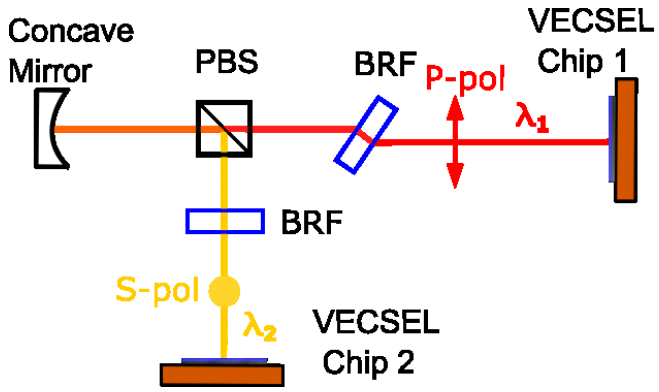

Fig. 4.3. Schematic drawing of a dual-wavelength VECSEL with T-shaped cavity design.

In this work, nearly equal power at each wavelength with a combined dual-wavelength CW output power in excess of 13 W was reported. This power level is promising for frequency conversions either inside or outside the cavity. Another advantage of this design, which is the versatility of the two emission wavelengths, arises from the independence of the two cavities. By employing different gain chips, the two wavelengths can be varied and so can the spacing between them. Furthermore, as discussed in chapter 3.1.3, the rotation of the BRF enables fine tuning of each wavelength. Feasible sum-frequency generation produced ~490 nm (blue) and ~532 nm (green) signal, as has been demonstrated in the following investigations by Lukowski et al. [25]. However, drawbacks are not avoidable in this kind of configuration. For instance, the PBS plays a critical role in this cavity and a very precise anti-reflection coating is required for its surface to minimize the losses. More importantly, since the polarizations of the two emission wavelengths are perpendicular to each other, this design is only suitable for type-II frequency conversion schemes. For applications favoring or requiring type-I frequency conversions, an alternative solution should be found.

4.1.4 Serially-connected Two-chip VECSEL

Inspired by the dual-gain-region approach, our aim was to combine this kind of design with a multiple-chip configuration. That is to say, two different gain chips are serially connected in one cavity, as shown in Fig. 4.4. Similarly to the T-cavity approach, the total gain of the system is elevated by the usage of the two chips and the pump induced heat can be dissipated by two heat sinks. Also, the spacing between the two wavelengths can be controlled by the choice of different chip-sets. Furthermore, since the chips perform as folding mirrors in the cavity, the emission wavelengths shift as a function of the chosen angles on the VECSEL chips, which can be utilized as an additional means of wavelength fine tuning in such a dual wavelength VECSELs [100]. The theoretical analysis will be given in chapter 5. In this case, the only difference between the designs of the two employed is the slightly different indium content in the QWs. With cavity angles of α=45° and β=20°, the actual emission wavelengths are 1023 nm and 1013 nm, respectively.

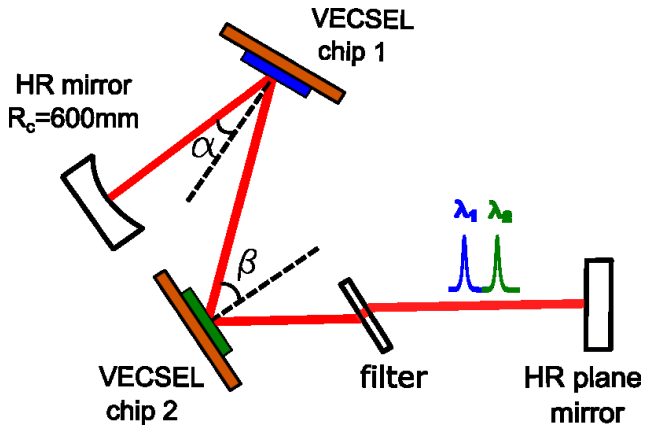

Fig. 4.4. Schematic drawing of a serially-connected two-chip dual-wavelength VECSEL

One important concern about this design relates to the question, how the profile of the total gain in this shared cavity is. To answer this, a 1-mm-thick BRF is inserted into the cavity. Since the FSR of the BRF is quite broad (~100 nm), only one lasing wavelength is observed. The laser output in this case can be considered as the convolution between the model gain of the two chips and the filter function of the BRF. Hence, the measure of the output power over the wavelength is able to reveal the shape of the gain profile. At a net pump power of 78 W, the wavelength tuning curve is plotted in Fig. 4.5. The two peaks represent the gain maxima of the two different chips, respectively, i.e., the gain of the chips actually combined together. One also notices, that the two

peaks are not completely separated, which means that there is an overlapping part in the combined gain profile.

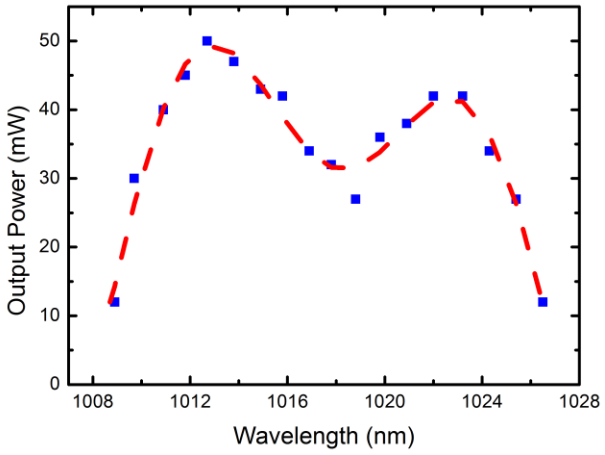

Fig. 4.5. The wavelength tuning curve of the serially-connected VECSEL chips reveals the combined gain profile of the two chips.

In a consecutive step, the 1-mm thick BRF is replaced by a 10-mm one, the FSR of which amounts to 10 nm and corresponds to the wavelength gap between the two gain-maxima. This filter does not only maintain the separation of the two emission wavelengths, but also controls their polarization, which is important for type-I frequency conversion. When only one of the two chips is pumped, only one color lasing can be obtained in each case, which is recorded as the blue and green curves, respectively, as shown in Fig. 4.6. Regarding the high power operation of the two curves, thermal roll-over comes into play when the pump powers are increased to 72 W and 45 W, respectively. The considerable difference in maximum powers mainly originates from the different chip surface quality of the two chips. As the chips are pumped simultaneously, the pump intensities on the two chips are adjusted to ensure the two emission wavelengths having comparable amplitudes. Shown as the red curve in Fig. 4.6, stable dual-wavelength operation can be observed starting from a net pump power of 47 W, given by the sum of the two net pump powers. With this laser configuration, 622 W of dual-wavelength intracavity power has been achieved at 99 W net pump power. When the pump powers are further increased, the lasing intensity from chip 2, i.e. the signal related to the chip's emission wavelength, increases significantly less than that from chip 1. Since the amplitudes of the two colors are no longer comparable, further points are not included in this plot.

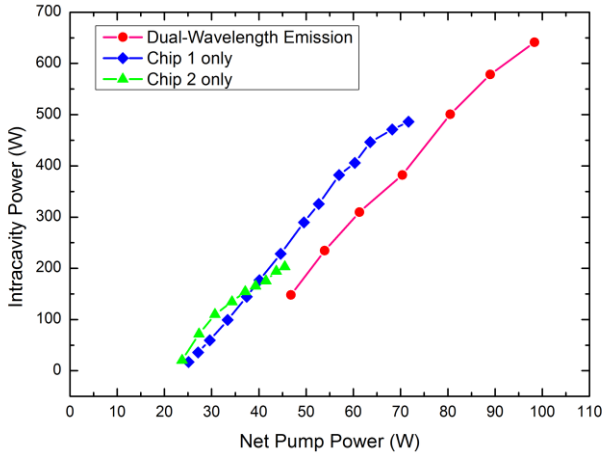

Fig. 4.6. Intracavity powers of single-chip as well as dual-wavelength operation as a function of the respective net pump power.

Naturally, the high intracavity power of the dual-wavelength emission suggests the possibility to perform intracavity frequency conversions. Therefore a piece of $LiNbO_3$ crystal (with the same design as in Ref. [18]) is inserted in the cavity, as shown in Fig. 4.7 (a). As the dual-wavelength operation starts, the green lights resulting from second-harmonic generation (SHG) and sum-frequency generation (SFG) can be readily detected, which are shown in Fig. 4.7 (b). The two peaks on the sides correspond to SHG from the two fundamental wavelengths, while the central peak is the result of SFG involving both wavelengths.

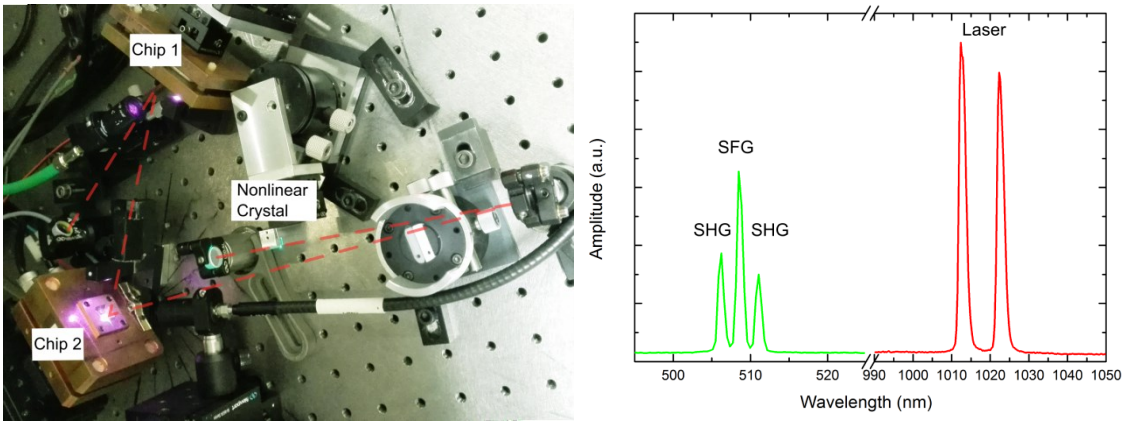

(a) (b)

Fig. 4.7 (a) Photo of the serially-connected two-chip dual-wavelength VECSEL for intracavity frequency conversion. The red dotted line denotes the laser cavity. (b) The dual-wavelength laser spectra (red, right side of spectrum) and their corresponding SHG as well as SFG spectra (green, left side).

Although the setup provides linearly polarized dual-wavelength high intracavity power, no THz signal has been detected from the aforementioned device, yet. This is attributed to the employed

$LiNbO_3$ crystal, the poling period and poling slanting angle of which sets its optimum operation frequency to 1.05 THz, while the design frequency of the current setup is 2.90 THz. Besides the inefficient conversion, the $LiNbO_3$ exhibits relatively high absorption at this wavelength, which makes THz generation more difficult. Hence, the choice of a suitable nonlinear crystal will be the subject of further endeavors to achieve efficient THz generation.

Despite the many advantages, the disadvantages of this configuration should also be addressed briefly in this section. When no filter is employed and the two emission wavelengths are close to each other (typically when the spacing < 5 nm), the two lasing colors tend to merge into one wavelength, which locates in between the original wavelengths. The reason should be attributed to the overlapped gain in this case: the shorter wavelength starts to in-well pump the longer wavelength and eventually they lase at the same wavelength in the overlapping zone of the gain profiles [101], [102]. To avoid this, either the wavelength spacing should be increased, or suitable filters should be used to separate the two wavelengths. In the aforementioned case, where the wavelength spacing is set to 10 nm and a BRF is used to maintain a separation of the two colors, there is still an overlapping part between the two chips. This results in anti-phase amplitude fluctuation between the two emission wavelengths, which is similar to the previous investigations [21], [26]. As pointed out by Ref. [20], in terms of statistics, when the two colors contain more longitudinal modes, the competition between them is less. Therefore, anti-phase amplitude fluctuation can be reduced at a high pump power level.

To summarize, the flexible, compact, serially-connected two-chip cavity design is able to provide linearly polarized dual-wavelength emission with high intracavity power and tunable wavelength spacing, which can be tailored by the choice of the chip-sets and filters. Fine tuning of the wavelength spacing is possible by changing the cavity angles on the two chips. Hence, this configuration can be readily applied to different kinds of type-I frequency conversion schemes.

4.2 Terahertz Emitting VECSELs

4.2.1 Previous Results of Terahertz Emitting VECSELs

In 2010, Scheller et al. demonstrated the first terahertz source based on VECSELs [18]. As discussed in section 4.1.1, the dual-wavelength operation is realized by the insertion of an etalon.

The chosen frequency differences of the two wavelengths as presented in that work are 1 and 1.9 THz, corresponding to etalons with a thickness of 100 μm and 54 μm, respectively. A 5 mol % MgO doped lithium niobate crystal with slant stripe periodic poling is placed in the laser cavity as the nonlinear medium for DFG [103], [104]. Owing to the phase matching condition in the nonlinear crystal, the generated THz signal is emitted perpendicularly to the laser propagation direction, which simplifies the detection and application of the THz beam. At room temperature, the THz signal at 1.9 THz exceeds 2 mW at an intracavity power of 500 W, while the measured power reached 0.5 mW at 1 THz.

Undoubtedly, this work attracted the attention from both the THz and the VECSEL community. A number of following investigations were carried out to deepen the understanding and to improve the performance. Chernikov et al. employed a streak camera to obtain wavelength- and time-resolved "recordings" of the laser emission [19]. Analyzed via a quantitative statistical approach, the data confirms that the dual-wavelength VECSEL operates stably for a wide range of pump powers, while unstably for extreme pump powers, i.e., near the lasing threshold or thermal roll-over. Later on, Wichmann et al. extended the investigations to multi-mode characterizations using single-color and free running VECSELs with varied cavity length [20] and the study of anti-phase dynamics in two-color operation [21]. With the help of the streak camera and the optical Michelson interferometer, the evolution of multi-mode operation of the VECSEL was studied systematically. The results show that each longitudinal mode exhibits random intensity fluctuations, while they cancel out each other when the number of the modes is sufficiently high. Hence, it has been found that stable dual-wavelength operation requires a high number of oscillating longitudinal modes within each color.

Wichmann et al. also characterized the bandwidth of the emitted CW THz signal from the TECSEL with the help of a self-built THz Michelson interferometer [96]. The multi-mode CW THz signal is found to result from the two simultaneously lasing groups of longitudinal VECSEL modes. Furthermore, the power-dependent experiments reveal a clear correlation between the THz signal bandwidth and the number of optical modes oscillating in the dual-wavelength VECSEL.

4.2.2 Beam Quality of the THz Signal from a TECSEL

As summarized in the last section, efforts have been made to improve the understanding and the performance of the TECSEL. Yet, one important property remains unclear – that is, the beam

quality of the emitted THz signal from the TECSEL. This is particularly of interest for applications for which a well defined beam profile is desired.

Typically, the beam quality of an optical beam can be quantified by the M^2 factor, which reflects the degree of variation of a beam compared to an ideal Gaussian beam at the same wavelength [105]. For a perfect Gaussian beam, the variation of the beam width ω(z) with the distance along the propagation direction is given by

$$\omega^2(z)=\omega_0^2+\left(\frac{\lambda}{\pi\omega^2}\right)^2(z-z_0)^2 \tag{4.1},$$

where z_0 is the location of the Gaussian beam waist. On the other hand, any real beam is more divergent than a Gaussian beam. Hence, with the help of Eq. (4.1), the beam widths of an arbitrary beam at x- and y-axis can be expressed as

$$\omega_x^2(z)=\omega_{0x}^2+M_x^4\bullet\left(\frac{\lambda}{\pi\omega_x}\right)^2(z-z_{0x})^2 \tag{4.2},$$

and

$$\omega_y^2(z)=\omega_{0y}^2+M_y^4\bullet\left(\frac{\lambda}{\pi\omega_y}\right)^2(z-z_{0y})^2 \tag{4.3},$$

where M_x and M_y are beam quality parameters characteristic of the particular beam. That is to say, the parameters M_x^2 and M_y^2 give a measure of the quality of the beam: the closer the parameters are to unity, the closer is the beam to the perfect Gaussian beam. From the technical point of view, in order to measure the M^2 factor of an arbitrary beam, a comparison between the arbitrary beam and the Gaussian beam needs to be undertaken. This can be achieved by focusing such beams and then comparing their beam waists as well as divergent angles with each other. As shown in Fig. 4.8, the beam diameters versus the propagation distance of a Gaussian beam and a beam with M^2=1.5 are plotted near the beam waist. In Fig. 4.8 (a), when the divergent angles (dash-dotted lines) of two beams are the same, the beam with smaller beam waist has the better beam quality. On the other hand, as we can see in Fig. 4.8 (b), when the beam waists of two beams are the same, the one with smaller divergent angle represents better beam quality.

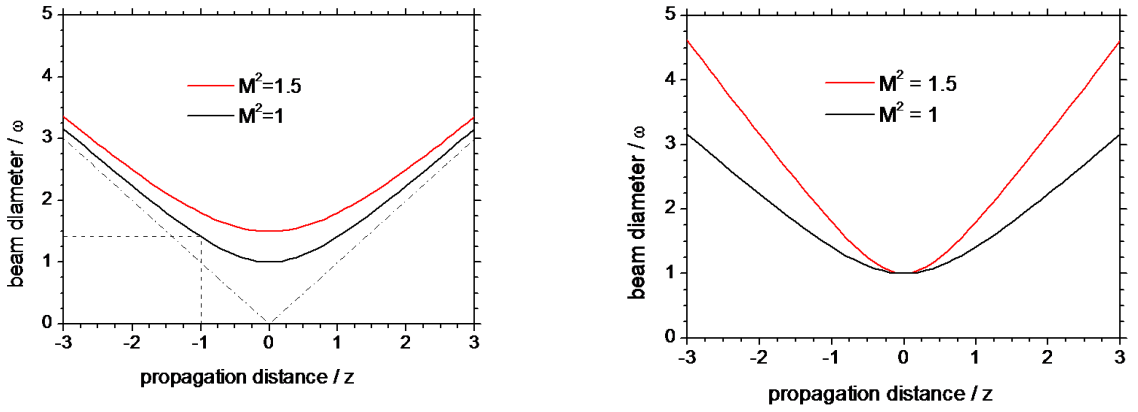

(a) (b)

Fig. 4.8. Comparison between a Gaussian beam and a beam with M^2=1.5. (a) Both beams have the same divergent angle, but different waist. (b) Both beams have the same beam waist but different divergent angle.

Therefore, to measure the exact M^2 factor of a beam, the beam widths at different positions should be determined. Here, according to the ISO international standard 11146, the beam width is defined as the second moment width D4σ, where σ is the standard deviation of the horizontal or vertical marginal distribution [106], [107]. The D4σ beam width in the x-dimension is given by

$$D4\sigma = 4\sqrt{\frac{\int_{-\infty}^{\infty}\int_{-\infty}^{\infty} I(x,y)(x-\bar{x})^2 dxdy}{\int_{-\infty}^{\infty}\int_{-\infty}^{\infty} I(x,y)dxdy}} \tag{4.4},$$

where I(x,y) represents the beam profile, and

$$\bar{x} = \frac{\int_{-\infty}^{\infty}\int_{-\infty}^{\infty} I(x,y)xdxdy}{\int_{-\infty}^{\infty}\int_{-\infty}^{\infty} I(x,y)dxdy} \tag{4.5},$$

is the centroid coordinates of the power density distribution. Also according to the ISO international standard 11146, the D4σ widths should be measured at 5 axial positions within one Rayleigh range from the beam waist, as well as at 5 axial positions at least one Rayleigh range away from the beam waist. Here, the Rayleigh range is defined as the distance along the propagation direction of a beam from the waist to the place where the area of the cross section is

doubled. Finally, the measured points should be fit by curves according to Eq. (4.2) as well as Eq. (4.3), and the M^2 values for x- and y-axis of the beam can be obtained.

The aforementioned criteria and principles have been used to perform such an M^2 measurement for the TECSEL and the results are summarized in the following. The experimental setup employed for this measurement is shown in Fig. 4.9. The TECSEL encircled by the red dashed lines in this image exhibits a design similar to the first reported TECSEL according to Ref. [18]. Here, dual-wavelength operation is enforced by the usage of an intracavity etalon. The lithium niobate crystal is placed close to the end mirror, where the beam waist of the laser reaches its minimum. Due to the thickness of the etalon and the periodic poling of the crystal, THz signal at the design frequency of 1.05 THz is emitted perpendicularly to the laser propagation direction. Since the THz beam is collimated in the horizontal direction but divergent in the vertical direction, a cylindrical lens made of high-density polyethylene (HDPE) is used to collimate the beam.

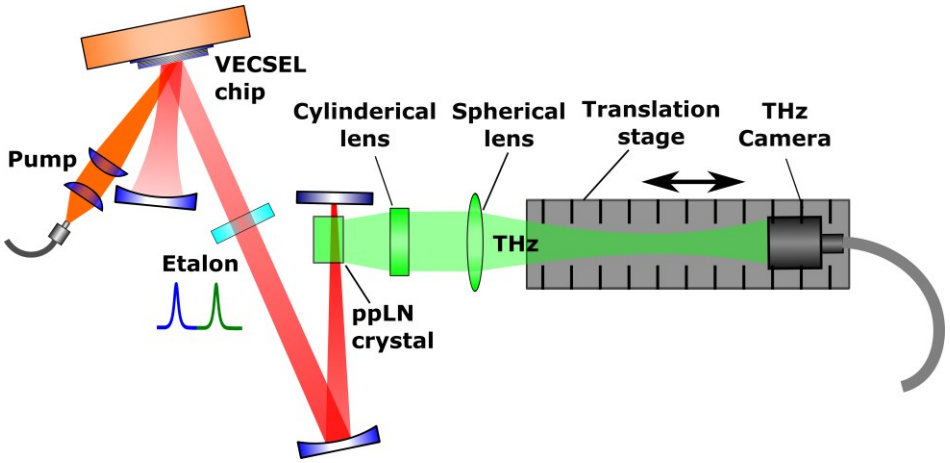

Fig. 4.9. Schematic drawing of the TECSEL setup (circled by the red dashed lines) as well as the THz beam profiler setup (circled by the green dashed lines).

The THz signal is then characterized by the custom-made THz beam profiler (circled by the green dashed lines), which consists of a focusing spherical lens and a commercial THz camera mounted on a translation stage. Unlike the common CCD camera in a commercial beam profiler, the employed camera for THz wavelength uses micro-bolometer arrays for imaging, which provides 384×288 pixels. With original imaging optics of the THz camera, a picture of the TECSEL is taken, as shown in Fig. 4.10 (a). The bright spot on the right part of the picture represents the THz signal generated in the nonlinear crystal, while the faint spare around it comes from the cylindrical lens. The other faint image on the left side of them is the end mirror of the laser cavity, which is observed by the camera because it is slightly heated by the high-intensity laser. As for the THz

beam profiler, the original optics are removed and the camera is placed after the focusing lens on the translation stage. A representative picture is taken in this case and shown as Fig. 4.10 (b). As we can see, although the beam cross section can be clearly observed, the background noise level is relatively high. According to eq. (4.4), the second-moment-based beam width definition heavily weights the tails or outer wings of the intensity profile. Accordingly, the background noise strongly influences the calculation of the second-moment width derived from beam profile measurements. Hence, an additional processing of the measured raw images has been applied.

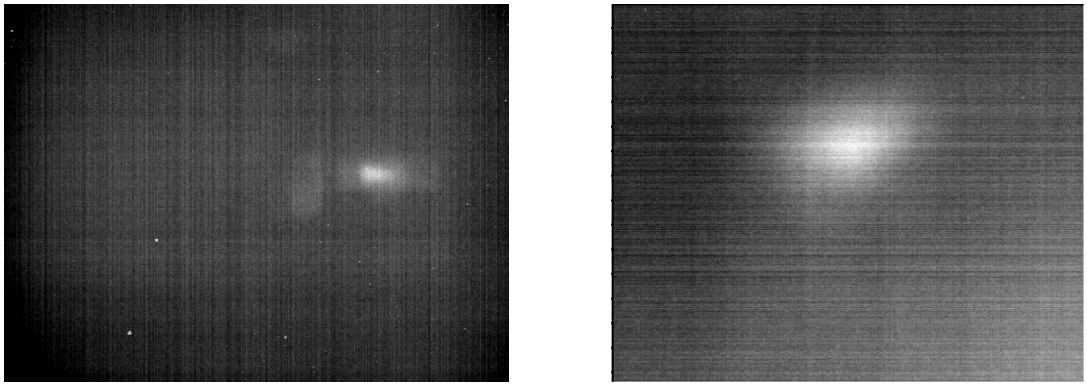

(a) (b)

Fig. 4.10 (a) A picture of the TECSEL taken by using the THz camera with its original optics. The bright spot represents the emitted THz signal from the PPLN crystal. (b) A raw image taken without using the camera optics. The background noise level is relatively high without any further processing.

For the image processing, the background pictures are taken each time after the beam profile was recorded, by only blocking the intra-cavity laser path during the measurements. In this way, the background pictures includes the thermal background noise from the TECSEL setup and ambient, which strongly disturbs the resulting image recorded with the THz camera. Then, the background data is used for the subtraction of the background noise and the intrinsic patterns in the image caused by the camera. At last, the region of interest from the image is selected. Exemplarily, a processed image is shown as the inset of Fig. 4.11. The cross sections in x- and y-direction show the beam profiles that can be each well approximated by a Gaussian profile, respectively.

Then the D4σ widths at different positions along the beam path are calculated based on Eqs. (4.4) and (4.5), and fit according to Ref. [108] for both the x- and the y-direction, as presented in Fig. 4.11. For comparison, the dashed lines in Fig. 4.11 represent the ideal Gaussian beam (M^2=1) with the same divergent angle as the measured solid lines, while the dotted lines show the geometrical limits.

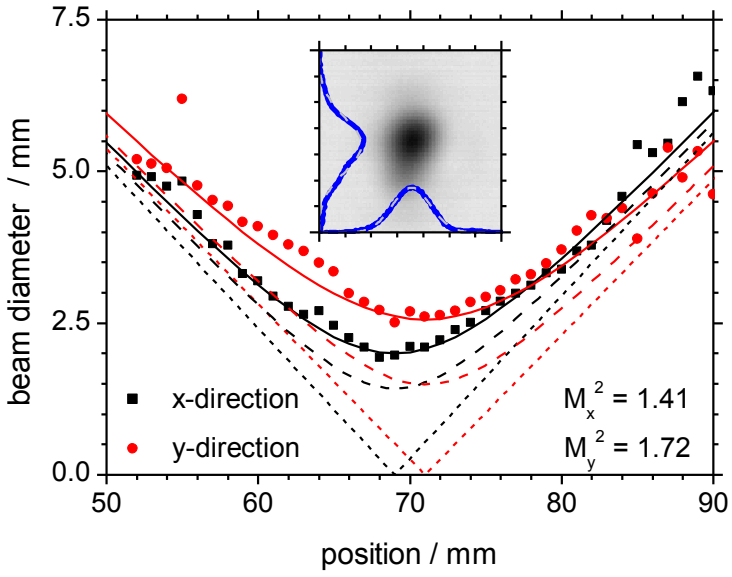

Fig. 4.11. Beam width along the propagation direction of the TECSEL's THz signal for x- and y-direction. The inset shows a processed image of the beam profile at a propagation position of 70 mm, corresponding to the beam waist [27].

The deduced beam quality M^2 factor values for x- and y-direction amount to 1.41 and 1.72, respectively, which reflect the good beam quality of the CW THz signal emitted from the TECSEL [27]. From the results it can be seen, that the beam quality for y-direction is not as good as that for the x-direction. Also, the axial positions of the beam waists for the two directions are not equivalent. These issues can be attributed to the imperfect cylindrical lens and the high divergence in y-direction. Hence, for future development of such devices, the cylindrical lens should be improved. Furthermore, the laser cavity geometry and the design of the nonlinear crystal can be further optimized, in order to achieve a more circular cross section of the generated THz beam.

5. Detuning and Angle-dependent Performance

In the previous chapters, we have demonstrated experimental highlights in the area of single-frequency and dual-wavelength VECSELs. To step further from the aforementioned milestones, the researchers have been constantly making efforts, not only by improving the experimental designs and techniques but also by deepening their understanding of the theory of VECSELs. In this chapter, we will focus on an important yet less-discussed concept, namely the spectral detuning between the micro-cavity resonance and material gain in the VECSEL. The definition and determination of the detuning will be given in the first part. Then the detuning of the device will be altered by varying the cavity angle of a V-shaped external cavity. In this way, the impact of different detunings on the performance of VECSELs will be experimentally evidenced especially for high-power operation. In the end of the chapter, this approach of a varied cavity angle will be further investigated as a method to extend the wavelength coverage of a VECSEL gain chip.

5.1 The Definition of Detuning

To understand the detuning of a VECSEL, the modal gain should first be addressed. As pointed out by Tropper et al., the modal gain can be considered as one of the most dominant factors regarding the output power as well as emission wavelength from a VECSEL [28]. It can be expressed as

$$\langle G \rangle = G_0 V^{-1} \Gamma_z \tag{5.1},$$

where G_0 is the material gain, V^{-1} represents the gain volume, and Γ_z is the longitudinal confinement factor (LCF).

Hence, the improvement of the modal gain should address these three factors. Indeed, been a great amount of work carried out to increase the material gain by means of epitaxial growth, theoretical modeling, and the application of various gain designs. For the gain volume, efforts have been made to reduce the thermal resistance of the device, which appears to be an essential and limiting factor to the gain volume [33], [45], [47], [109]. The LCF is defined as the proportion between the confined optical energy in the quantum wells and the total optical energy in the whole device, given by

$$\Gamma_z = \frac{\sum_q \left| E^+(z_q) + E^-(z_q) \right|^2}{\left| E_0^+ \right|^2 + \left| E_0^- \right|^2} \tag{5.2},$$

where $E^+(z_q)$ and $E^-(z_q)$ indicate the electric fields in the quantum well located at position z_q from the incident and reflected directions, while E_0^+ and E_0^- indicate the electric fields in the whole structure from both directions.

Then the detuning can be defined as the wavelength difference between the QW emission wavelength and the LCF wavelength, which is given by

$$\Delta\lambda_{\text{det}} = \lambda_{PL} - \lambda_{LCF} \tag{5.3},$$

where λ_{PL} is the wavelength of the photoluminescence (PL) maximum of the gain region, and λ_{LCF} the wavelength of the longitudinal confinement factor resonance at 20°C.

There are several common approaches to access both λ_{PL} and λ_{LCF} [5] [110]. In this work, we use a direct and accurate method, which works by measuring the QW photoluminescence (PL) and reflectivity of the final laser structure and then comparing it with the simulated reflectivity and LCF. It is worth noting that in order to avoid the Fabry-Pérot resonance from the micro-cavity, the VECSEL sample is illuminated under normal incidence at its edge, and the PL emitted from that edge is detected perpendicularly. Apart from the measurement of the reflectivity of the gain mirror, HR-XRD measurements are performed to obtain the layer thicknesses and compositions as initial values for the simulation of the reflectivity, which is presented as the transfer matrix method in Ref. [28]. In this way, the detuning of this representative chip, which has been employed in the previous work of high-power single-frequency VECSEL, is quantified with -40 nm [17].

5.2 The Impact of the Detuning

The influence of the detuning on the performance of the laser can be understood with the help of the schematic illustration in Fig. 5.1. Assuming that the detuning of the VECSEL chip has a negative value, this means that the QW emission wavelength λ_{PL} is shorter than the LCF wavelength λ_{LCF} when the chip is not pumped at room temperature (cf. Fig. 5.1 (a)). When the pumping starts and the temperature of the gain region rises, λ_{PL} and λ_{LCF} both shift to longer wavelengths. However, λ_{PL} and λ_{LCF} have different drifting rates (approximately 0.3 nm/K and

0.1 nm/K respectively). Hence, as the pump power increases, a small part of the spectral peak of the QW emission overlaps with that of the LCF wavelength (cf. Fig. 5.1 (b)). According to Eq. (5.1), the overlapping area indicates the modal gain of the laser. When the modal gain exceeds the loss, the laser reaches the threshold, and lasing starts. As the temperature rises with the further pumping, the gain keeps increasing until the maximum overlap of the two peaks is attained, which leads to the maximum output power (cf. Fig. 5.1 (c)). If the pump power is further increased, λ_{PL} shifts beyond λ_{LCF}. Since the overlapping area shrinks, the modal gain drops, and eventually, the laser reaches the thermal roll-over (cf. Fig. 5.1 (d)). Hence, for a certain VECSEL, the detuning determines the pumping/thermal requirements to reach the lasing threshold, optimum lasing, as well as thermal roll-over.

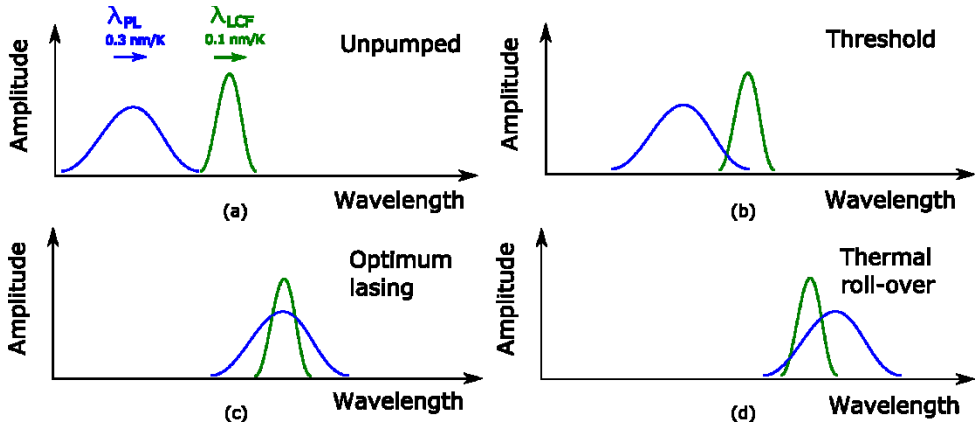

Fig. 5.1. Schematic illustration of the relationship between the QW emission wavelength (λ_{PL}, blue peak) and the LCF wavelength (λ_{LCF}, green peak) under different conditions: (a) not pumped, (b) at lasing threshold, (c) at optimum lasing, (d) at thermal roll-over.

In 2010, Hader et al. presented a detailed theoretical analysis of the detuning-dependent performance of VECSELs [29]. This works predicted that a large detuning is optimal for high power operation, i.e. LCF maximum and QW gain overlap perfectly at the point of thermal roll-over as desired. This is in agreement with previous high-power results obtained by using the aforementioned VECSEL chip or a chip from the same wafer [17], [32].

Until now, to our knowledge, the only experimental study of detuning has been carried out by Wang et al., where three VECSELs with different detunings were investigated [111]. Therefore, three chips from different wafers were produced. However, due to the further processing of the VECSELs, there is an unavoidable variation of the chip quality, especially during the flip-chip bonding and the removal of the capping layer. So in order to avoid chip-to-chip fluctuations, it is

desired to manipulate the detuning of one specific laser sample while the change of the performance is studied.

Here, we employ a V-shaped external cavity (cf. Fig. 5.2 (a)) to alter the detuning of one VECSEL chip: If the chip is operated to function as the folding mirror, the oblique angle of incidence results in a blue shift of the reflectivity curve and, more importantly, also of the LCF [100]. This effect can be accurately calculated with the transfer matrix method. As shown in Fig. 5.2 (b), when the angle is varied from 0° to 60°, the LCF maximum changes from 1035 nm to 1004 nm, while its magnitude of 4 is maintained [110]. Consequently, the detuning can be altered between -40 nm and -9 nm, which is to say, covering a large range in the theoretical investigations by Hader et al. [109].

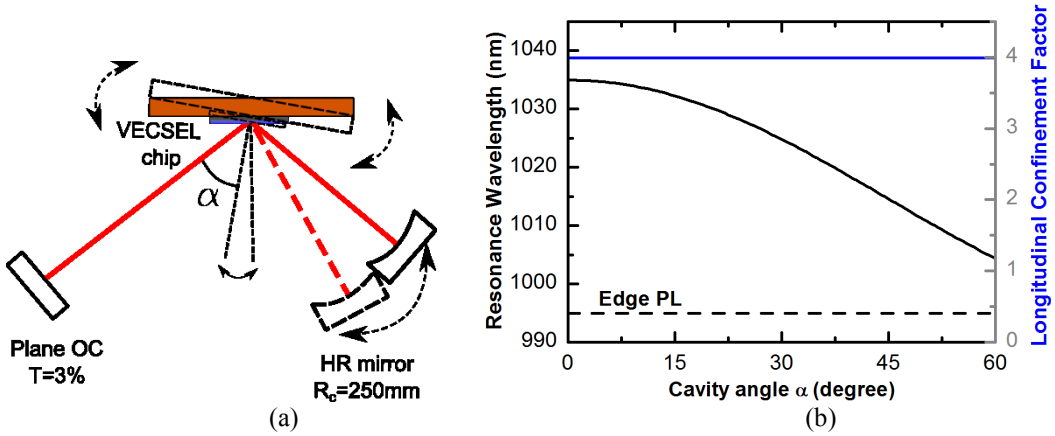

Fig. 5.2 (a) Schematic drawing of the V-shaped cavity in the experimental setup; (b) calculated LCF peak wavelength (left) and peak value (right) as a function of the V-cavity angle α, respectively.

At first, a certain technical consideration should be addressed: As the incident angle of the V-cavity α is increased, the major axis of the fundamental transverse mode projecting on the chip surface becomes larger, whereas the minor axis remains the same. For instance, in a cavity with $\alpha = 15°$, the major axis of the TEM_{00} mode measures 420 µm and the minor axis 400 µm. When the cavity angle α is increased to 45° and the cavity length remains unchanged, the major axis of the mode is increased to 570 µm while the minor axis remains 400 µm. So in TEM_{00} operation, it can hardly be observed whether a change in the performance is due to a different overlap with the pump spot or due to the detuning. This obstacle can be overcome with a relatively large pump spot. Thereby, the higher-order transverse modes fill in the complete pump spot even if the indices of the involved TEM_{nm} modes are changing with the cavity angle. However, it is still questionable if the ratio between the pump spot size and the TEM_{00} mode size (here denoted as *p/m* ratio) plays an important role in the performance of the laser. Therefore, a control experiment is conducted as follow: In the V-cavity with $\alpha = 30°$, the cavity length is varied in order to obtain different *p/m*

ratios of 272%, 229%, and 196%, which match the *p/m* ratios that are obtained for α = 15°, α = 30°, and α = 45° at a fixed cavity length of 230 mm. As we can see from Fig. 5.3, all three power curves behave highly similarly: The difference of the maximum output powers between the three cases is less than 2%. In this way, the control test confirms the insignificance of different *p/m* ratios for high-order transverse mode operation, and hence, with a change of the cavity angle, the detuning can be varied as a sole parameter.

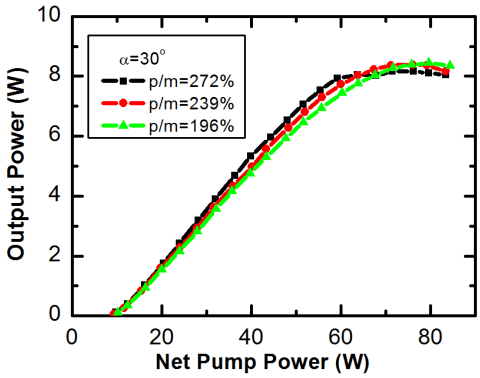

Fig. 5.3. Output powers vs. net pump powers for different pump-spot-size/TEM_{00}-mode-size ratios (*p/m* ratios) in a 30° V-cavity.

Then the influence of different detunings on the output power is investigated for the angles α = 15°, 30°, and 45°, which correspond to detunings of -37 nm, -30 nm, and -20 nm, respectively, at room temperature. For the selected cavity angles, the measured output powers as a function of the net pump power are plotted in Fig. 5.4. In the case of α=45°, the output power reaches its maximum of 5.2 W at a net pump power of 61.6 W. As the cavity angle is decreased to 30°, the detuning is increased, and so is the heat needed to reach the thermal roll-over. This results in a delayed thermal roll-over at a net pump power of 73.8 W. As a consequence, the maximum output power is increased to 7.6 W. In the cavity with α=15°, the detuning is further enlarged. Therefore, the thermal roll-over is not reached even at our maximum net pump power. The highest output power in this case is 9.0 W at the net pump power limitation of 83.6 W. By comparing the maximum output powers when α = 45° and α = 15°, an increment over 70% is noticed, which proves the importance of the detuning to the high-power operation of VECSELs.

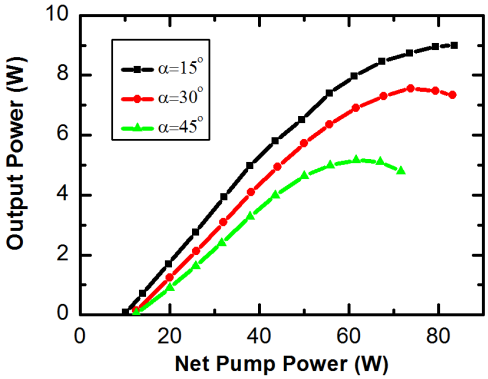

Fig. 5.4 Output powers vs. net pump powers for different V-cavities with cavity angles α=15°, 30° and 45°, respectively.

In the aforementioned three cases, the thresholds do not differ from each other notably. The main reason is that the heat sink temperature of 70°C provides a large offset to the modal gain. At low pump powers, this offset elevates the threshold in all three cases to a comparable level. Therefore, the measurement is repeated at a heat sink temperature of 20°C. Here, the thresholds show significant differences: They are 25.6 W, 13.9 W and 7.4 W, for α=15°, 30° and 45°, respectively. The influence of the detuning is then pronounced: As the detuning decreases, less pump power is required to achieve enough overlap between the material gain and the LCF to overcome the losses, which is to say, the lasing threshold is lowered.

As a short summary, the experimental results regarding both output powers and thresholds agree well with the theoretical modeling: A large detuning delays the thermal roll-over and provides the possibility to achieve high output powers at high pump powers, while a decreased detuning results in lowered requirements to reach thresholds.

5.3 Angle-dependent Performance of the VECSEL

Since the change of the V-cavity angle spectrally shifts the peak of the LCF, the emission wavelength can also be altered in this way. As the power curves in Fig. 5.4 are measured, the wavelengths are simultaneously recorded with a spectral meter, which are shown in Fig. 5.5. In the exemplary case of α = 15°, the maximum wavelength during operation ranges from 1019.4 nm to 1024.9 nm, which is due to the LCF shift caused by the rise of the temperature in the gain structure. After the cavity angle is changed to 30°, the wavelength range is red-shifted 7.0 nm, while it is

further shifted 7.4 nm in the case where α = 45°. Based on this result, we can have a glance at the broad wavelength coverage resulting from the different detunings.

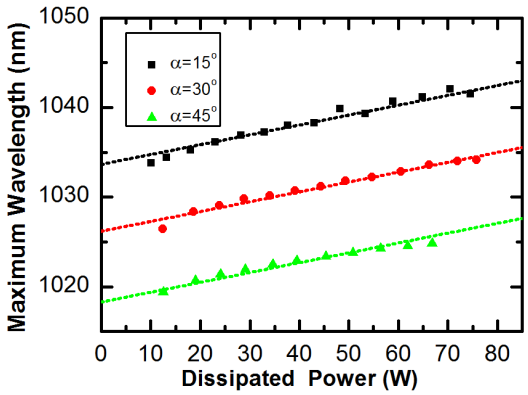

Fig. 5.5. Maximum wavelengths as a function of the dissipated power for different V-cavities, for which the cavity angle α was set to 15°, 30°, and 45°, respectively. The dotted lines represent linear fittings to the measured maximum wavelengths.

In order to investigate the wavelength tuning range with respect to different detunings, a 1 mm thick BRF is placed in the cavities at its Brewster's angle. As mentioned in chapter 3.1.1, the rotation of the BRF enables the tuning of the emission wavelength. The wavelength tuning ranges are measured at a medium net pump power of 49.1 W for all three cavities to avoid thermal roll-over. As shown in Fig. 5.6, for the cavity with α=45°, the center wavelength can be tuned from 1016.3 nm to 1033.3 nm – while for α=30° and α=15°, the tuning range covers 1022.6 nm to 1045.9 nm and 1029.6 nm to 1050.9 nm, respectively.

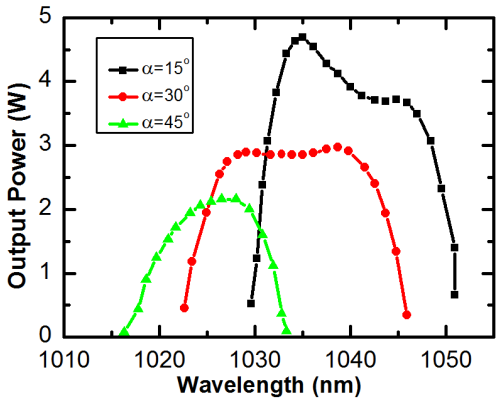

Fig. 5.6. Wavelength tuning curves of the three V-cavities, respectively, displaying output powers as a function of the center wavelength of emission at a net pump power of 49.1 W.

Here, we can see that the wavelength accessibility of one single VECSEL chip is drastically increased with the help of the cavity angle. In principle, the wavelength accessibility can be improved by additionally increasing or reducing the cavity angle. If an application is tolerant to output powers, the wavelength coverage of one single VECSEL chip can be further broadened by altering the heat sink temperature and pump powers. The combination of these techniques can be readily used in the applications which require a broad wavelength tuning range.

6. Summary and Outlook

This thesis is dedicated to experimental investigations and developments of VECSELs. Three aspects are highlighted: single-frequency operation, dual-wavelength operation, and the impact of detuning.

Chapter 3 focuses on the single-frequency VECSELs, which operate on fundamental transverse mode, single longitudinal mode, and single polarization mode simultaneously. The single-frequency operation can be achieved by employing intracavity frequency-selective elements, such as etalons, BRFs, and gratings, or by using a very short (~ mm) cavity. Since this work aims for a high-power single-frequency VECSEL, the gain chip is placed between the two external mirrors of a V-shaped cavity to double the round-trip gain. The pumped area is approximately 500 μm in diameter, which provides a large gain volume. In order to introduce a proper amount of loss to the system, a 10 mm thick intracavity BRF is used for longitudinal mode control, while an output coupler with 5% transmission is employed to increase the losses for all possible modes. Thereby, a single-frequency VECSEL with 23.6 W output power is realized. The major noise sources are identified by analyzing the laser linewidth with respect to the sample time. Furthermore, frequency stabilization techniques are applied to the free-running single-frequency laser. The passive stabilization significantly reduces the ground noise level, while the active stabilization stops the frequency drift and further narrows the linewidth.

In the future work, the thermal management of the single-frequency VECSEL should be improved. Thereby, the output power should be able to reach 30 W and even more. The setup could be isolated in a vacuum environment to upgrade the passive stabilization. Sophisticated active stabilization techniques, such as the Hänsch-Couillaud method and Pound-Drever-Hall method, are promising for the further narrowing the linewidth, which could bring the linewidth close to the Schawlow-Townes limit.

Chapter 4 presents the study of dual-wavelength VECSELs as well as of THz-emitting VECSELs. Each existing approach to implement dual-wavelength operation has its own advantage, while also exhibiting certain drawbacks. Therefore, we here demonstrate a new cavity design in which two different gain chips are serially connected in one cavity. In this way, the gain of the two chips is combined, which results in a high intracavity power of over 600 W. The wavelength spacing of the dual-wavelength emission can be flexibly altered by using different chip sets and/or intracavity filters. These features, together with the linear polarization of the output, make this design ideal for

different kinds of type-I frequency conversions, especially for intracavity DFG to generate THz. Attention is also paid to characterize the beam quality of the THz signal emitted from the existing TECSELs. For this purpose, a beam profiler is built, based on a commercial THz camera and a linear translation stage. According to the ISO standard, the deduced M^2-factor amounts to 1.41 for the x-axis and 1.72 for the y-axis. This result demonstrates the good beam quality of the THz beam.

For the next step of this work, a suitable nonlinear crystal should be chosen to perform the DFG in the serially-connected two-chip cavity. From this setup, a milliwatt-level signal at 3 THz can be expected. Additionally, different chip sets can be used to obtain dual-wavelength emissions with different wavelength-spacings, which lead to THz generation of different frequencies. With these features, the new TECSELs can be considered as good candidates to fill the THz gap. In order to heighten the beam quality of the TECSEL, the cylindrical lens after the nonlinear crystal should be improved. In this way the THz beam should be better collimated, which results in a better beam quality in the y-direction.

In chapter 5, the detuning of VECSELs is discussed and its impact on the performance of the device is experimentally demonstrated. The detuning is defined as the difference between the QW emission wavelength and the LCF wavelength. In this work, we alter the cavity angle of a V-shaped cavity in which the VECSEL chip serves as a folding mirror to change the LCF wavelength of the VECSEL. In this way, different detunings can be obtained from the same gain chip. With a large detuning of -37 nm, the maximum output power is 73% higher than that with a detuning of -20 nm. This drastic improvement is due to the delay of the thermal roll-over. In terms of the lasing threshold, it decreases from 25.6 W to only 7.4 W, as the detuning changes from -37 nm to -20 nm at room temperature. The change of the cavity angle also leads to a shift of the emission wavelength. Thereby, the wavelength accessibility of one VECSEL chip can be greatly improved. In this case, the wavelength tunability of one single chip reaches 35 nm.

The investigation of the detuning will help in the future design of VECSELs. A large detuning should be considered when the application is aiming for high output powers, while a small detuning is favorable if a low threshold is required. The introduced method can be readily applied to VECSELs with different gain media, such as type-II QWs or QDs in order to compare fundamental laser properties of such devices. Furthermore, the broadened tuning range resulting from this method is attractive for the applications that require additional wavelength accessibility.

7. Publications

A 23-watts single-frequency vertical-external-cavity surface-emitting laser

Fan Zhang, Bernd Heinen, Matthias Wichmann, Christoph Möller, Bernardette Kunert, Arash Rahimi-Iman, Wolfgang Stolz, and Martin Koch

Optics Express, vol. 22, no. 11, pp. 12817–12822, Jun. 2014.

Contribution: The experiments were planned and carried out by me under the guidance of Prof. M. Koch and Dr. A. Rahimi-Iman. Dr. B. Heinen gave his opinion on how to achieve single-frequency operation. Dr. M. Wichmann helped with the laser cavity design. The manuscript is written by me with the help of Dr. A. Rahimi-Iman. All coauthors contributed with the important ideas and the improvement of the manuscript.

A 23-watts single-frequency vertical-external-cavity surface-emitting laser

Fan Zhang,[1,*] Bernd Heinen,[1] Matthias Wichmann,[1] Christoph Möller,[1]

Bernardette Kunert,[2] Arash Rahimi-Iman,[1] Wolfgang Stolz,[1,2] and Martin Koch[1]

[1]*Department of Physics and Materials Sciences Center, Philipps-Universität Marburg, Renthof 5, 35032 Marburg, Germany*
[2]*NAsP III/V GmbH, Am Knechtacker 19, 35041 Marburg, Germany*
**fan.zhang@physik.uni-marburg.de*

Abstract: We report on a single-frequency semiconductor disk laser which generates 23.6 W output power in continuous wave operation, at a wavelength of 1013 nm. The high output power is a result of optimizing the chip design, thermal management and the cavity configuration. By applying passive stabilization techniques, the free-running linewidth is measured to be 407 kHz for a sampling time of 1 ms, while undercutting 100 kHz in the microsecond domain.

OCIS codes: (140.3570) Lasers, single-mode; (140.5960) Semiconductor lasers; (140.7270) Vertical emitting lasers.

References

1. B. Heinen, T.-L. Wang, M. Sparenberg, A. Weber, B. Kunert, J. Hader, S. W. Koch, J. V. Moloney, M. Koch, and W. Stolz, "106 W continuous-wave output power from vertical-external-cavity surface-emitting laser" Electron. Lett., **48**, 516 –517 (2012).
2. T. Leinonen, S. Ranta, M. Tavast, R. Epstein, G. Fetzer, N. Sandalphon, N. Van Lieu, and M. Guina, "High power (23W) vertical external cavity surface emitting laser emitting at 1180 nm" Proc. SPIE **8606**, 860604–860604–6 (2013).
3. A. Laurain, C. Mart, J. Hader, J. V. Moloney, B. Kunert, and W. Stolz, "Optical noise of stabilized high-power single frequency optically pumped semiconductor laser" Opt. Lett., **39**, 1573–1576 (2014).
4. A. Laurain, C. Mart, J. Hader, J. V. Moloney, B. Kunert, and W. Stolz, "15 W Single Frequency Optically Pumped Semiconductor Laser With Sub-Megahertz Linewidth" IEEE Photonics Technol. Lett., **26**, 131–133 (2014).
5. A. Rantamaki, A. Chamorovskiy, J. Lyytikainen, and O. Okhotnikov, "4.6-W Single Frequency Semiconductor Disk Laser With <75 kHz Linewidth," IEEE Photonics Technol. Lett., **24**, 1378 –1380 (2012).
6. S. Kaspar, M. Rattunde, T. Topper, B. Rosener, C. Manz, K. Kohler, and J. Wagner, "Linewidth Narrowing and Power Scaling of Single-Frequency 2.X µm GaSb-Based Semiconductor Disk Lasers" IEEE J. Quantum Electron., **49**, 314 –324 (2013).
7. Y. Kaneda, J. M. Yarborough, L. Li, N. Peyghambarian, L. Fan, C. Hessenius, M. Fallahi, J. Hader, J. V. Moloney, Y. Honda, M. Nishioka, Y. Shimizu, K. Miyazono, H. Shimatani, M. Yoshimura, Y. Mori, Y. Kitaoka, and T. Sasaki, "Continuous-wave all-solid-state 244 nm deep-ultraviolet laser source by fourth-harmonic generation of an optically pumped semiconductor laser using CsLiB_6O_10 in an external resonator" Opt. Lett., **33**, 1705 (2008).
8. M. Rahim, A. Khiar, F. Felder, M. Fill, H. Zogg, and M. W. Sigrist, "5-µm vertical external-cavity surface-emitting laser (VECSEL) for spectroscopic applications" Appl. Phys. B, **100**, 261–264 (2010).
9. W. J. Alford, G. J. Fetzer, R. J. Epstein, Sandalphon, N. Van Lieu, S. Ranta, M. Tavast, T. Leinonen, and M. Guina, "Optically Pumped Semiconductor Lasers for Precision Spectroscopic Applications" IEEE J. Quantum Electron., **49**, 719–727 (2013).
10. P. Georges, I. Sagnes, and A. Garnache, "Design of a low-threshold VECSEL emitting at 852 nm for Cesium atomic clocks" Opt. Quantum Electron., **40**, 167–173 (2008).
11. S. Ranta, M. Tavast, T. Leinonen, R. Epstein, and M. Guina, "Narrow linewidth 1118/559 nm VECSEL based on strain compensated GaInAs/GaAs quantum-wells for laser cooling of Mg-ions" Opt. Mater. Express, **2**, 1011–1019 (2012).
12. K. Gardner, R. Abram, and E. Riis, "A birefringent etalon as single-mode selector in a laser cavity" Opt. Express, **12**, 2365–2370 (2004).
13. A. Chernikov, M. Wichmann, M. K. Shakfa, M. Scheller, J. V. Moloney, S. W. Koch, and M. Koch, "Time-dynamics of the two-color emission from vertical-external-cavity surface-emitting lasers" Appl. Phys. Lett., **100**, 041114 (2012).
14. M. Wichmann, M. K. Shakfa, F. Zhang, B. Heinen, M. Scheller, A. Rahimi-Iman, W. Stolz, J. V. Moloney, S. W. Koch, and M. Koch, "Evolution of multi-mode operation in vertical-external-cavity surface-emitting lasers" Opt. Express, **21**, 31940–31950 (2013).
15. M. Scheller, J. M. Yarborough, J. V. Moloney, M. Fallahi, M. Koch, and S. W. Koch, "Room temperature continuous wave milliwatt terahertz source" Opt. Express, **18**, 27112–27117 (2010).
16. M. Mangold, V. J. Wittwer, C. A. Zaugg, S. M. Link, M. Golling, B. W. Tilma, and U. Keller, "Femtosecond pulses from a modelocked integrated external-cavity surface emitting laser (MIXSEL)" Opt. Express, **21**, 24904–24911 (2013).

17. K. G. Wilcox, F. Rutz, R. Wilk, H. D. Foreman, J. S. Roberts, J. Sigmund, H. L. Hartnagel, M. Koch, and A. C. Tropper, "Terahertz imaging system based on LT-GaAsSb antenna driven by all-semiconductor femtosecond source" Electron. Lett., **42**, 1159 (2006).
18. K. G. Wilcox, A. C. Tropper, H. E. Beere, D. A. Ritchie, B. Kunert, B. Heinen, and W. Stolz, "4.35 kW peak power femtosecond pulse mode-locked VECSEL for supercontinuum generation" Opt. Express, **21**, 1599 (2013).
19. L. Kornaszewski, G. Maker, G. p. a. Malcolm, M. Butkus, E. u. Rafailov, and C. j. Hamilton, "SESAM-free mode-locked semiconductor disk laser" Laser Photonics Rev., **6**, L20–L23 (2012).
20. A. R. Albrecht, Y. Wang, M. Ghasemkhani, D. V. Seletskiy, J. G. Cederberg, and M. Sheik-Bahae, "Exploring ultrafast negative Kerr effect for mode-locking vertical external-cavity surface-emitting lasers" Opt. Express, **21**, 28801–28808, (2013).
21. K. G. Wilcox and A. C. Tropper, "Comment on SESAM-free mode-locked semiconductor disk laser" Laser Photonics Rev., **7**, 422–423, (2013).
22. J. Moloney, I. Kilen, A. Bäumner, M. Scheller, and S. W. Koch, "Nonequilibrium and thermal effects in mode-locked VECSELs" Opt. Express, **22**, 6422, (2014).
23. M. Gaafar, C. Möller, M. Wichmann, B. Heinen, B. Kunert, A. Rahimi-Iman, W. Stolz, and M. Koch, "Harmonic self-mode-locking of an optically pumped semiconductor disc laser" Electron. Lett., **50**, 542-543 (2014).
24. M. A. Holm, D. Burns, A. I. Ferguson, and M. D. Dawson, "Actively stabilized single-frequency vertical-external-cavity AlGaAs laser" IEEE Photonics Technol. Lett., **11**, 1551–1553 (1999).
25. L. Fan, M. Fallahi, J. T. Murray, R. Bedford, Y. Kaneda, A. R. Zakharian, J. Hader, J. V. Moloney, W. Stolz, and S. W. Koch, "Tunable high-power high-brightness linearly polarized vertical-external-cavity surface-emitting lasers" Appl. Phys. Lett., **88**, 021105–021105–3 (2006).
26 . B. Heinen, F. Zhang, M. Sparenberg, B. Kunert, M. Koch, and W. Stolz, "On the Measurement of the Thermal Resistance of Vertical-External-Cavity Surface-Emitting Lasers (VECSELs)" Quantum Electron. IEEE J. Of, **48**, 934 –940 (2012).
of Vertical-External-Cavity Surface-Emitting Lasers (VECSELs)" Quantum Electron. IEEE J. Of, **48**, 934 –940 (2012).
27. F. Riehle, *Frequency Standards: Basics and Applications*, (Wiley-VCH, 2005), Chap. 2.
28. A. Garnache, A. Ouvrard, and D. Romanini, "Single-Frequency operation of External-Cavity VCSELs: Non-linear multimode temporal dynamics and quantum limit" Opt. Express, **15**, 9403–9417 (2007).

1. Introduction

In recent years, single-frequency vertical-external-cavity surface-emitting lasers (VECSELs) have been intensively investigated owing to their potential to combine a high output power [1,2], a narrow linewidth [3-6] and a large frequency-tunability [6] in one device. Such lasers, also called semiconductor disk lasers (SDLs), are available for a broad spectral range between the ultraviolet [7] and the mid-infrared [8] and are versatile systems that attract the attention from a wide range of application areas, such as spectroscopy [9], metrology [10], optical free-space telecommunication and laser cooling [11].

The other advantage of VECSELs arises from the combination of a semiconductor laser chip with an external cavity, in which intra-cavity elements can be easily employed to access diverse operating conditions. For instance, birefringent filters (BRFs) inside the cavity can enforce single-frequency continuous wave (CW) operation with excellent beam quality [12], while the use of an intra-cavity etalon can promote a stable two-color emission [13, 14], which can be utilized for the generation of CW THz-radiation via frequency conversion in a nonlinear crystal [15]. Employing saturable absorber mirrors VECSELs can be driven in a mode-locked regime [16,17] with peak powers as high as 4.3 kW [18]. It is worth noting, that nowadays mode-locking even without the use of saturable absorbers is observed for such lasers [19-23].

A thorough thermal management allows for considerably high output powers up to 106 W in transverse and longitudinal multimode operation [1]. Besides high output powers, however, numerous applications require a high degree of coherence and stability of the light source. Thus, frequency noise reduction, thermal stability and cavity optimization become significantly important in order to improve the performance of single-frequency VECSELs beyond current limitations. Such passive stabilization techniques serve as the foundation for high-power lasers with a narrow linewidth, prior to employing active stabilization schemes [3,6,24].

In this work, we demonstrate a narrow-linewidth single-frequency VECSEL emitting at 1013 nm, with an output power of 23.6 W. To our knowledge, it represents the highest output power for single frequency VECSELs reported so far. Passive stabilization techniques and an optimized VECSEL design are employed in order to demonstrate a sub-100-kHz free-running linewidth in the microsecond domain and a linewidth of 407 kHz for a sampling time of 1 ms, both at 23.6 W. Moreover, we point out the main contributors to frequency noise that limit the long-time stability of our high-power single-frequency VECSEL.

2. VECSEL chip design and setups

An MOVPE-grown VECSEL chip is employed with a gain region consisting of 10 InGaAs quantum wells (QWs), equally spaced by GaAsP barrier layers. The QWs are arranged to overlap with the antinodes of the standing light field, which is often referred to as a resonant periodic gain (RPG) structure. 22.5 AlAs/GaAs layer pairs form the distributed Bragg reflector (DBR), which has a reflectivity higher than 99.9% at 1013 nm. In order to obtain high output power in single-frequency operation, the micro-cavity resonance at room temperature is initially detuned from the emission wavelength of the QWs for about 18 nm. This is a similar configuration as used in previous studies in order to provide an enhanced spectral overlap and thus optimized gain at high pump powers [1]. The chip is bonded to a diamond heat spreader via solid-liquid-interdiffusion bonding and the semiconductor substrate is removed by selective wet etching.

The VECSEL is optically pumped by an 808 nm fiber-coupled laser which delivers a maximum pump power of 120 W. As shown in Fig.1, a V-shaped cavity is formed by a high-reflectivity concave mirror (radius of curvature R_C = 600 mm) and a plane output coupler together with the VECSEL chip in between. Such a V-configuration leads to a doubled round-trip gain for a given temperature and carrier density [25], as the photons will pass the gain region twice as often as in a cavity where the chip serves as an end-mirror. This design resembles the key difference to the previous works. Because of the enhanced gain, an output coupler with 5% transmission can be employed to achieve high output power. Moreover, the laser mode does not experience any astigmatism, which makes the output beam circular and more suitable for applications. The total optical length of the cavity is 140 mm and it results in a longitudinal mode spacing around 1070 MHz. The TEM_{00} mode on the chip has a diameter about 630 µm. To ensure fundamental-transverse-mode operation, the pump-spot size is chosen to be about 20% smaller than the laser mode. A 10-mm-thick birefringent filter is placed at Brewster's angle (α_B) to control the emitted longitudinal mode. For a minimum loss on the lasing mode, no further intracavity elements are employed. On the other hand, other modes are further suppressed by the relatively high loss induced by the 5%-transmission output coupler. The temperature of the chip is stabilized by the thermo-electric cooler (TEC), which is attached to the back side of the copper heat sink. During operation, the heat generated inside the semiconductor is transferred by the TEC and removed by a water-cooled copper plate. Here, very soft pipes are employed in order to minimize the mechanical vibration coupled from the water cooling system to the heat sink. Most of the optical components are directly mounted on a low-frequency-damping optical table via pedestal pillar posts, which are made of stainless steel and provide high stiffness. The laser setup is surrounded by a plastic housing, which has walls of 20 mm thickness. Additionally, acoustic foam is attached to the inner side of the housing. In this way, thermal fluctuation and acoustical noise originating from the environment are strongly reduced.

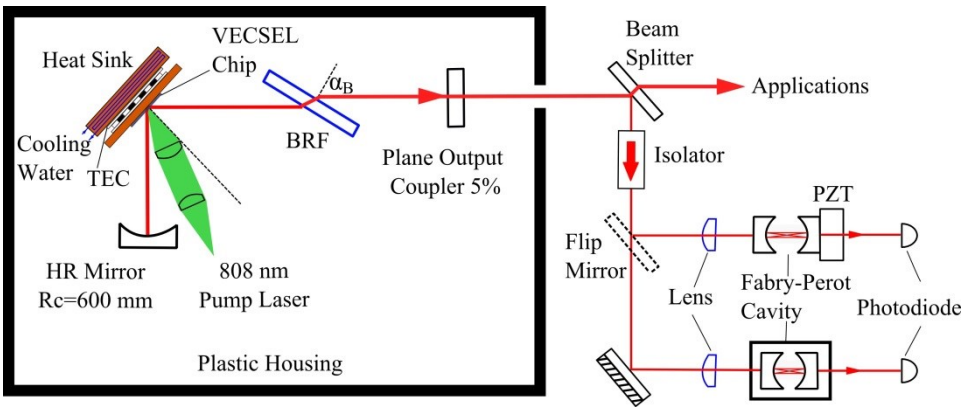

Fig. 1. Schematic drawing of the experimental setup with boxed VECSEL, confocal scanning Fabry-Perot interferometer and frequency discriminator.

3. Experimental results

A heat sink temperature of 16 ℃ allows for single-frequency operation, which is achieved at a fundamental transverse mode and a single longitudinal mode, up to a maximum output power of 23.6 W (Fig. 2). To maintain single-frequency operation at high powers, a careful tuning of the BRF is required. However, this

tuning causes variations in the resulting output power. The linear fitting of the single-frequency output power, shown as the dashed line in Fig. 2, yields a slope efficiency of 44% and a laser threshold at about 15 W net input power. Neglecting the 30%-high reflection loss of the pump beam at the air-chip interface, a total optical-to-optical efficiency of 33% is achieved for an output power of 23.6 W at 71.2 W net input power.

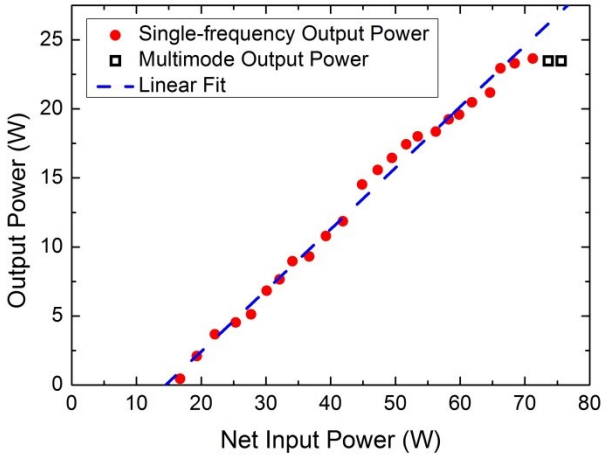

Fig. 2. Output power as function of net input power.

Single-frequency operation is confirmed via a self-made high-resolution confocal scanning Fabry-Perot interferometer (SFPI) which reveals a free spectral range (FSR) of 500 MHz [Fig. 3(a)]. The slightly asymmetrical shape of peaks in the SPFI spectra is due to misalignment and the difference between rise- and fall-time of the current amplifier employed in the SPFI. At an output power of 20 W, single-frequency operation which lasted for more than one minute without mode hopping was observed. As the net input power is increased above 70 W, the VECSEL starts to experience thermal roll-over [26]. If the chip is pumped stronger, side-peaks will arise and single-frequency operation will turn into multiple-longitudinal-mode operation, which is indicated by black squares in Fig. 2. The corresponding SFPI spectrum is shown in the inset of [Fig. 3(a)]. To demonstrate the fundamental-transverse-mode profile, a CCD camera image is recorded under single-frequency operation and is presented in [Fig. 3(b)], with Gaussian cross-sections in both dimensions.

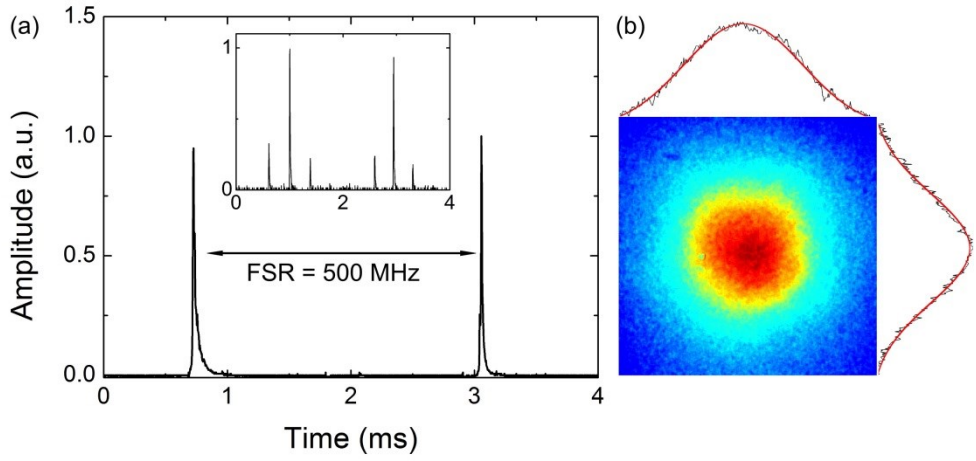

Fig. 3. (a) Scanning Fabry-Perot interferometer spectrum at an output power of 23 W. The free spectral range (FSR) amounts to 500 MHz. Inset: multiple-longitudinal-mode spectrum at a net pump power of 73 W. (b) Output beam profile captured by a CCD camera representing TEM_{00} mode operation. The intensity distributions of the horizontal and vertical cross-sections through the center of the spot are shown on top and right, respectively.

The laser linewidth deduced from the interferometer measurement is 3.3 MHz, which is limited by the resolution of the SFPI. In order to measure the precise value of the linewidth, another Fabry-Perot cavity with a FSR of 750 MHz and a finesse of 34 was set up as a frequency discriminator (see Fig. 1). By coupling a part of the laser output beam into the reference cavity, it converts the frequency fluctuation of the free-running laser into an amplitude variation of the transmitted signal [27]. A DAQ card, which has a maximum sampling rate of 200 kSamples/s, is employed to record the transmitted signal. Since the laser linewidth exhibits a dependency on sampling time [4,6], it is necessary to deduce the resulting linewidth as a function of different sampling time windows (see Fig. 4). At an output power of 23.6 W, the free-running laser yields a linewidth of 88 kHz for a sampling time of 100 µs and 407 kHz for 1 ms. As the sampling time increases, all kinds of low frequency noise start to affect laser-linewidth broadening to a greater extent. As a result, the linewidth is deduced to be 1.78 MHz for a sampling time of 1 s. Although the graph in Fig. 4 does not provide a direct measure of the undesirable noise components, attribution is feasible via the indirect measure which is provided by sampling-time-dependent linewidth analysis. In this study, signatures of two main contributors to linewidth broadening in our systems are observed, well agreeing with previous studies considering noise mechanisms. The first contributor to linewidth broadening is attributed to the acoustical and mechanical resonance from the water cooling system, which corresponds to the considerably steep increase of linewidth in the millisecond domain, i.e. for sampling times ranging from approximately 1 ms to 5 ms (cf. blue colored area in Fig. 4). This is in good agreement with the literature [4,6]. Further broadening of the laser linewidth at longer time spans occurs mainly due to the second contributor, which we attribute to fast thermal drifts within the setup, one source of which is the thermal fluctuation induced by pump laser intensity fluctuation as identified in the literature [3,28] (cf. red colored area in Fig. 4). This illustrates, that a stable free running system is expected as long as aforementioned noise components – generally spoken: external disturbance – are suppressed.

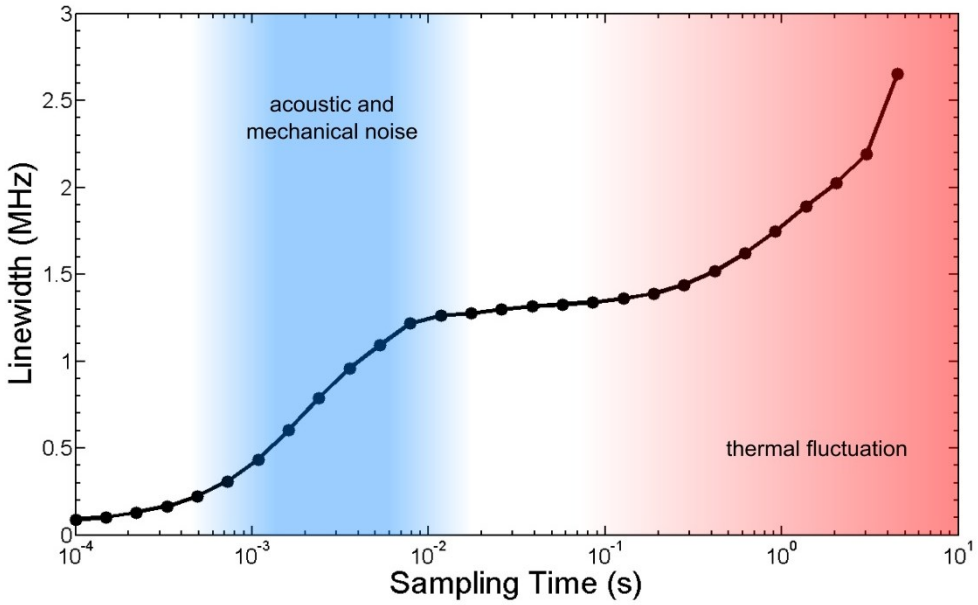

Fig. 4. Laser linewidth as function of sampling time.

4. Conclusion

To summarize, we presented a high-power single-frequency VECSEL operating at an emission wavelength of 1013 nm with a maximum output power of 23.6 W. The linewidth of the emission is determined to be in the sub-100-kHz range for short sampling times of 100µs, while a linewidth of 407 kHz is obtained at a sampling time of 1 ms. The study of the linewidth as function of the sampling time reveals that the stability of the free-running VECSEL is mainly limited by low frequency noise, which could be compensated by

active-stabilization techniques in future studies [24]. With the help of improved thermal management techniques, we have the reason to believe that it is possible to push the single-frequency output power above 30 W.

Acknowledgment

The authors acknowledge financial support from the German Science Foundation (DFG: GRK 1782, DFG: SFB 1083).

Dual-wavelength emission from a serially-connected two-chip VECSEL

Fan Zhang, Mahmoud Gaafar, Christoph Möller, Wolfgang Stolz, Martin Koch,
and Arash Rahimi-Iman

IEEE Photonics Technology Letters, vol. 28, no. 8, pp. 927–929, Apr. 2016.

Contribution: The experiments were planned and carried out by me with the help of Dr. A. Rahimi-Iman. Dr. M. Gaafar supported me with the idea of measuring the anti-phase fluctuations. All coauthors helped with the interpretation of the data and the writing of the manuscript.

Dual-wavelength emission from a serially-connected two-chip VECSEL

Fan Zhang, Mahmoud Gaafar, Christoph Möller, Wolfgang Stolz, Martin Koch and Arash Rahimi-Iman

Abstract—We present a compact two-chip vertical-external-cavity surface-emitting laser design, which provides dual-wavelength emission with a wavelength separation of 10 nm. The design is ideal for type-I frequency conversion, since the two wavelengths exhibit the same polarization and over 600 W intracavity power is generated. Dual-wavelength operation with other desirable wavelength difference can be achieved in this flexible cavity, by using different chip combinations and suitable filters.

***Index Terms*—Vertical-external-cavity surface-emitting laser (VECSEL), semiconductor disk laser (SDL), dual wavelength, optical wavelength conversion.**

INTRODUCTION

Owing to the intensive studies in the recent few years, optically pumped vertical-external-cavity surface-emitting lasers (VECSELs) have shown great potential in high-power multimode, single-frequency and mode-locking operation [1-3]. The flexible open cavity makes this kind of laser ideal for intracavity frequency conversion, for which many application-oriented cavity designs have been proposed [4,5]. Dual-wavelength operation employed for difference-frequency generation (DFG) and sum-frequency generation (SFG) in VECSELs is usually achieved by introducing a Fabry-Perot etalon in the cavity [6-8]. However, the separation of the two wavelengths is only a few nanometers, limited by the gain bandwidth of one VECSEL chip. To improve this, multi-chip configurations have come into consideration. For instance, a T-cavity configuration which exploits two VECSEL chips with different emission wavelength is suggested by Hessenius et al. [9]. 300 W intracavity power has been realized in such two-chip cavity for DFG [10]. Yet, due to the fact that the two wavelengths are orthogonally polarized, this configuration is only suitable for type-II frequency conversion.

In this work, we demonstrate an alternative approach for VECSELs, utilizing a flexible, compact, serially-connected two-chip cavity design. By employing different chip-sets as well as birefringent filters (BRFs) with suitable thickness, the laser is able to generate high-power emission with two wavelengths, which exhibit the same polarization and a desirable wavelength separation. Furthermore, we present intracavity type-I second harmonic generation (SHG) and SFG.

EXPERIMENTAL SETUP

Two MOVPE-grown VECSEL chips are employed in our experiments. Both chips consist of 10 InGaAs quantum wells (QWs), equally spaced by GaAsP barrier layers. The resonant periodic gain (RPG) structure is arranged by overlapping the QWs with the antinodes of the standing light field. 22.5 AlAs/GaAs layer pairs form the distributed Bragg reflector (DBR). Both chips have the same design but slightly different indium concentration in the QWs. Therefore the designed wavelength of one chip is about 10 nm shorter than that of the other. In order to optimize the thermal management, each chip is bonded to a diamond heat spreader via solid-liquid interdiffusion bonding and then mounted to a water-cooled copper heat sink.

As shown in Fig. 1, the VECSEL chips are optically pumped by two fiber-coupled diode lasers at 808 nm. In order to ensure the TEM_{00} mode operation, the pump spot size on each chip is adjusted to be about 10% smaller than the fundamental laser mode size. The laser resonator is completed by serially connecting the first high reflective (HR) concave mirror, two VECSEL chips, the second HR concave mirror, and a HR plane mirror.

The authors acknowledge financial support by the DFG (GRK 1782 and SFB 1083). M. Gaafar acknowledges support from the Yousef Jameel scholarship funds. The authors would like to thank NAsP III/V GmbH, B. Heinen and B. Kunert for the fabrication of the VECSEL chips.

F. Zhang, M. Gaafar, C. Möller, W. Stolz, M. Koch and A. Rahimi-Iman are with the Department of Physics and Materials Science Center, Philipps-University of Marburg, Renthof 5,35032 Marburg, Germany (e-mail: fan.zhang@physik.uni-marburg.de).

W. Stolz is also with NAsP III/V GmbH, Am Knechtacker 19, 35041 Marburg, Germany.

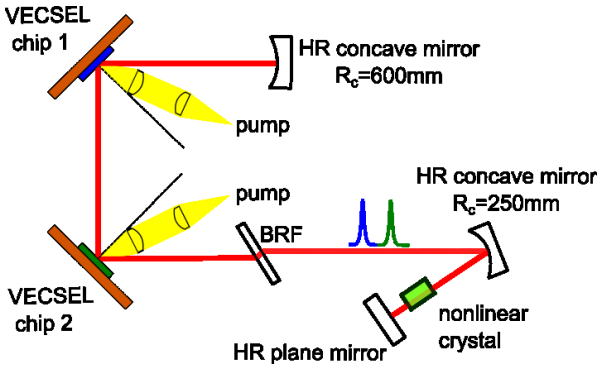

Fig. 1 Schematic drawing of the experimental setup.

A quartz BRF is inserted in the cavity at its Brewster's angle. When a BRF with a free spectral range (FSR) much broader than the gain bandwidth of the laser is employed, only one lasing wavelength will be oscillating in the cavity. By rotating the BRF, the lasing wavelength is forced to shift within the range of the laser's gain bandwidth. Since the output of the laser has a dependence on the convolution of the filtering function and the laser's gain profile, measuring the output power over wavelength will give us a glance at the shape of the total gain of the laser. When a different BRF is used, the filtering effect is possible to allow two wavelengths oscillating simultaneously in the cavity. Therefore with different chips and a suitable BRF, the wavelength separation of the dual-wavelength emission can be extended to even tens of nanometers. Furthermore, the BRF forces the two emission wavelengths to have the same polarization(p-polarization in our case), which makes the setup suitable for type-I frequency conversion.

RESULTS

When only one chip in this cavity is pumped, the laser is able to work at one frequency. As the two chips are both pumped, the gain of the two different chips is combined and therefore the total gain bandwidth becomes broader than that of any single chip. To prove that, a BRF with 1 mm thickness is inserted in the cavity and both chips are pumped simultaneously. Since the FSR of the BRF is rather broad (~100 nm), only one wavelength is oscillating in the cavity. As shown in Fig. 2, the 18-nm wide tuning curve containing two peaks suggests that only a small part of the gain profiles of the two different chips is overlapping. The two peaks at 1013 nm and 1023 nm indicate a 10-nm separation between the optimal lasing wavelengths of the two-chip VECSEL.

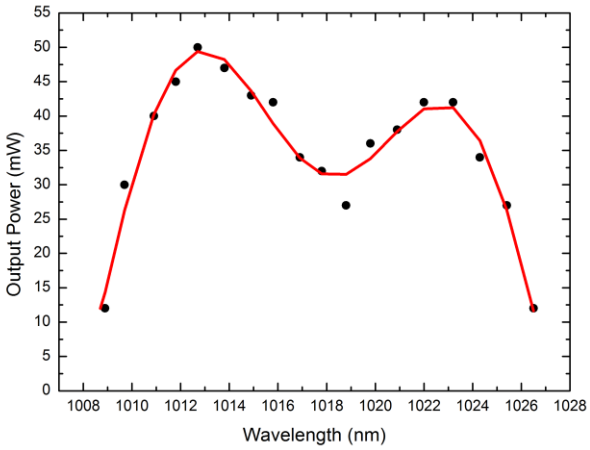

Fig. 2 Wavelength tuning by rotating a 1-mm BRF at a net pump power of 78 W. The two peaks reveal the shape of the combined gain of the two different chips. The red two-peak curve serves as a guide to the eye.

In order to make the best use of the combined gain in this configuration, the 1-mm BRF is replaced by a 10-mm one, which has a FSR of 10 nm and will coincide with the separation of the two gain peaks. As the two chips are pumped simultaneously, the pump intensities on the two chips are adjusted to ensure the two emission wavelengths having comparable amplitudes. Shown as the red curve in Fig. 3, starting from a net pump power of 47 W, stable dual-wavelength operation can be observed. Compared to the one-chip operation (green and blue curves in Fig. 3), the slope efficiency of the two-wavelength emission is lower, being attributed to additional loss from the filtering. However due to the fact that the heat is dissipated on two chips and that the power is combined, the total intracavity power of the two-chip operation can be much higher than that of any one-chip operation, without any sign of thermal roll-over. Owing to the high-Q cavity, the intracavity power reaches 642 W at a net pump power of 99 W. When the chips are further pumped, the lasing intensity from chip 2 increases significantly less than that from chip 1, which is mainly due to the different surface conditions of the chips. Therefore the amplitudes of the two emission wavelengths are no longer comparable and the data is not included in Fig. 3.

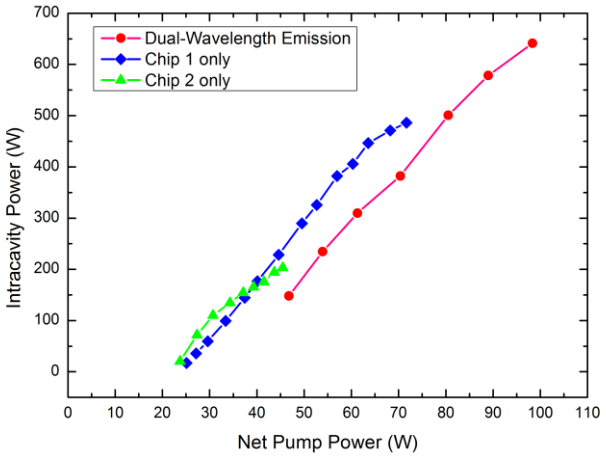

Fig. 3 Intracavity power of dual-wavelength and single chip operation as a function of net pump power. The different performance of the two chips is mainly due to their different surface conditions.

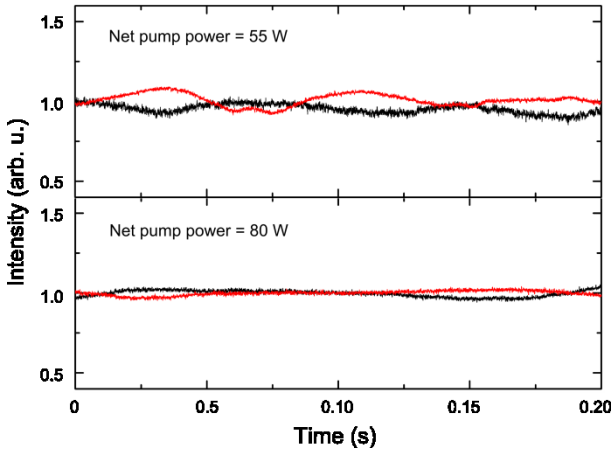

Fig. 4 Normalized time traces of the two emission wavelengths for low (55 W) and high (80 W) net pump powers.

For a dual-wavelength VECSEL, it is important to investigate the coupling of the two emission wavelengths. Therefore we use the similar method described in Ref. [11]: a grating is employed to spatially separate the two wavelengths of the output beam; then the intensity of each wavelength is measured by a photodiode. The normalized time traces for low (55 W) and high (80 W) net pump powers are shown in Fig. 4. In both cases, we observe the antiphase fluctuations in the intensity of the two wavelengths, which indicates that the gain profiles of the two chips partly overlap with each other, for both low and high pump powers. In our future work, the coupling of the two wavelengths shall be investigated for other chips with further gain separation. Here, we find that the antiphase fluctuations for high pump power are significantly decreased in comparison to the low-power level, which can be attributed to the increase of the oscillating mode number. This result is in good agreement with Refs [8] and [11].

Since this setup provides high-power two-wavelength emission with the same polarization, it is suitable for different kinds of type-I frequency conversion. Therefore a periodically poled $LiNbO_3$ (PPLN) crystal is inserted between the second concave mirror and the plane mirror, where the beam waist reaches its minimum. As the dual-wavelength operation starts, bright green light can be observed. The components of the converted light are identified using an optical spectrometer. The SHG and SFG signal (left) together with the laser lines (right) are displayed in Fig. 5: the two peaks at the sides originate from SHG, each of which well corresponds with one wavelength of the laser, while the central peak originates from SFG during the dual-wavelength operation.

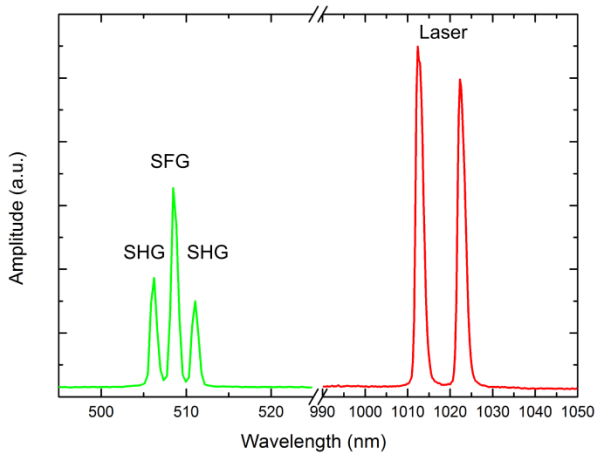

Fig. 5 The spectrum of the dual-wavelength emission as well as the SHG and SFG signal.

Considering the 10-nm separation between the two wavelengths, we are confident about the possibility of THz generation with the frequency around 3 THz via DFG from the PPLN crystal. Compared to the type-II DFG performed in Ref. [10], with the same intracavity power and beam diameter, the expected output power from the type-I DFG in the similar PPLN crystal is four times of the former scheme, since the crystal does not have to be rotated anymore by 45° to adapt to the polarization of the intracavity beam. However, as a consequence of the high absorption in the $LiNbO_3$ crystal at 3 THz, no THz signal has yet been detected experimentally with this setup. Thus, employing other kinds of nonlinear crystals for the achievement of efficient type-I DFG will be an important subject of future work and crucial for the development of a strong and frequency-versatile CW-THz source.

CONCLUSION

By serially connecting two different VECSEL chips in one cavity, we have combined the gain of both chips. With different chip-combinations and filters, this design shows the potential to offer dual-wavelength operation with tailored wavelength differences. Linearly polarized dual-wavelength emission with a wavelength separation of 10 nm and 642 W intracavity power has been generated by using a 10-mm BRF. Thereby type-I intracavity SHG and SFG in a PPLN crystal have been demonstrated.

REFERENCES

[1] B. Heinen, T.-L. Wang, M. Sparenberg, A. Weber, B. Kunert, J. Hader, S. W. Koch, J. V. Moloney, M. Koch, and W. Stolz, "106 W continuous-wave output power from vertical-external-cavity surface-emitting laser," Electron. Lett., vol. 48, no. 9, pp. 516 –517, 2012.

[2] F. Zhang, B. Heinen, M. Wichmann, C. Möller, B. Kunert, A. Rahimi-Iman, W. Stolz, and M. Koch, "A 23-watt single-frequency vertical-external-cavity surface-emitting laser," Opt. Express, vol. 22, no. 11, pp. 12817–12822, Jun. 2014.

[3] M. Scheller, T.-L. Wang, B. Kunert, W. Stolz, S. W. Koch, and J. V. Moloney, "Passively modelocked VECSEL emitting 682 fs pulses with 5.1W of average output power," Electron. Lett., vol. 48, no. 10, pp. 588–589, May 2012.

[4] J. Lin, H. M. Pask, D. J. Spence, C. J. Hamilton, and G. P. A. Malcolm, "Continuous-wave VECSEL Raman laser with tunable lime-yellow-orange output," Opt. Express, vol. 20, no. 5, p. 5219, Feb. 2012.

[5] F. A. Camargo, J. Barrientos, G. Baili, L. Morvan, D. Dolfi, D. Holleville, S. Guerandel, I. Sagnes, P. Georges, and G. Lucas-Leclin, "Coherent Dual-Frequency Emission of a Vertical External-Cavity Semiconductor Laser at the Cesium Line," IEEE Photon. Technol. Lett., vol. 24, no. 14, pp. 1218–1220, Jul. 2012.

[6] L. Fan, M. Fallahi, J. Hader, A. R. Zakharian, J. V. Moloney, W. Stolz, S. W. Koch, R. Bedford, and J. T. Murray, "Linearly polarized dual-wavelength vertical-external-cavity surface-emitting laser," Appl. Phys. Lett., vol. 90, no. 18, pp. 181124, Apr. 2007.

[7] M. Scheller, J. M. Yarborough, J. V. Moloney, M. Fallahi, M. Koch, and S. W. Koch, "Room temperature continuous wave milliwatt terahertz source," Opt. Express, vol. 18, no. 26, pp. 27112–27117, Dec. 2010.

[8] M. Wichmann, M. K. Shakfa, F. Zhang, B. Heinen, M. Scheller, A. Rahimi-Iman, W. Stolz, J. V. Moloney, S. W. Koch, and M. Koch, "Evolution of multi-mode operation in vertical-external-cavity surface-emitting lasers," Opt. Express, vol. 21, no. 26, pp. 31940–31950, Dec. 2013.

[9] C. Hessenius, M. Lukowski, and M. Fallahi, "High-power tunable two-wavelength generation in a two chip co-linear T-cavity vertical external-cavity surface-emitting laser," Appl. Phys. Lett., vol. 101, no. 12, pp. 121110–121110–3, Sep. 2012.

[10] M. Lukowski, C. Hessenius, and M. Fallahi, "Widely Tunable High-Power Two-Color VECSELs for New Wavelength Generation," IEEE J. Sel. Top. Quantum Electron., vol. 21, no. 1, pp. 1–8, Jan. 2015.

[11] M. Wichmann, G. Town, J. Quante, M. Gaafar, A. Rahimi-Iman, W. Stolz, S. W. Koch, and M. Koch, "Anti-Phase Noise Dynamics in a Dual-Wavelength Vertical-External-Cavity Surface-Emitting Laser," IEEE Photonics Technol. Lett., vol. 27, pp. 2039, 2015.

Investigation of the beam quality of a terahertz emitting vertical-external-cavity surface-emitting laser

Fan Zhang, Siming Wang, Arno Rehn, Matthias Wichmann, Gunter Urbasch,
Arash Rahimi-Iman, Stephan W. Koch, and Martin Koch

Journal of Infrared, Millimeter and Terahertz Waves, vol. 37, no. 6, pp. 536–539, Apr. 2016.

Contribution: The experiments were planned and carried out by me under the guidance of Prof. M. Koch. S. Wang and A. Rehn assisted me in the experiments. Dr. M. Wichmann and Dr. G. Urbasch supported me with the theoretical background of the TECSEL and beam quality. All coauthors contributed to the evaluation of the data and the writing of the manuscript.

Investigation of the beam quality of a terahertz emitting vertical-external-cavity surface-emitting laser

Fan Zhang,[1*] Siming Wang,[1] Arno Rehn,[1] Matthias Wichmann,[1] Gunter Urbasch,[1] Arash Rahimi-Iman,[1] Stephan W. Koch,[1] and Martin Koch[1]

[1]*Faculty of Physics and Material Sciences Center, Philipps-University of Marburg, Renthof 5, D-35032 Marburg, Germany*

*corresponding author: fan.zhang@physik.uni-marburg.de

Keywords: CW THz sources, surface-emitting semiconductor disc lasers, terahertz spectroscopy, beam quality

Abstract

We characterize the terahertz beam emitted by a compact Peltier-cooled room-temperature terahertz emitting vertical-external-cavity surface-emitting laser. We determine the beam quality factor M^2 for horizontal and vertical direction, respectively.

Terahertz (THz) technology is a rapidly evolving field for which many applications are foreseen [1-5]. In 2010, Scheller *et al.* presented a new kind of continuous-wave THz source: the terahertz emitting vertical-external-cavity-surface emitting laser (TECSEL) [18]. This source relies on intracavity difference-frequency generation of laser modes bunched around two laser wavelengths. Subsequently this THz source was characterized regarding its stability which is associated with the dynamics of the laser emission at the different wavelengths involved [7-10]. Yet, one important aspect which has not been investigated so far is the quality of the emitted THz beam. This is what we concentrate on in this letter.

At optical wavelengths and in particular for the characterization of lasers the so called beam quality factor M^2 is the parameter which reflects the degree of variation of a beam compared to an ideal Gaussian beam of the same wavelength (see [11, 12] for a definition of M^2 and how to derive it on the basis of measuring second moment widths $D4\sigma$, i. e. the beam diameters along beam-propagation direction). The closer this parameter is to one the closer is the beam to an ideal Gaussian beam. Note, that while for most common laser types there are even commercial solutions available to measure the beam quality of these sources, in contrast, there are only few of such measurements (see [13] for an example) in the THz frequency region.

The setup of the characterized TECSEL is schematically shown in Fig. 1. The VECSEL chip holder temperature is kept at 15 °C throughout the experiment by a thermoelectric cooler (Peltier-element) to maintain stable laser operation and THz generation. The VECSEL chip contains 10 (GaIn)As quantum-wells which serve as the active medium (see [14] for further details on chip and heat management). The diameter of the pump laser spot is adjusted for maximum overlap with the laser mode on the chip, thereby ensuring an emission on a pure TEM_{00}-mode profile. The VECSEL resonator has a Z-shape with a total length of 52 cm. Highly reflecting mirrors ensure a high intra-cavity power [9]. The cavity contains a silica etalon with a thickness of approximately 100 µm which enforces a two-color emission of the laser. Each of the two colors contains several longitudinal laser modes. Photons from these modes are converted via difference-frequency generation to THz photons in a non-linear crystal [6].

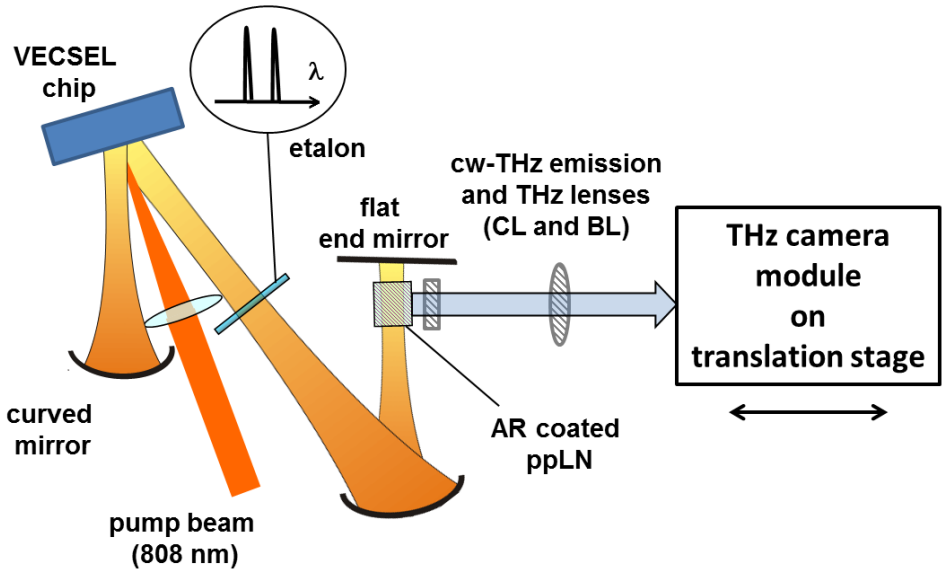

Fig. 1 Schematic drawing of a VECSEL-driven THz source together with a sketch of the THz beam path used for imaging of the THz beam with a THz camera module.

For the non-linear crystal we use a 5 mol % MgO doped Lithiumniobate crystal with a slant stripe periodic poling. By the two free design parameters poling period and poling slanting angle, respectively, the THz emission wavelength can be set to a value of intend. Here, these parameters are chosen as a period of 51 µm and a slanting angle of 67.4 degree. This determines the design frequency of 1.05 THz. The non-linear crystal is positioned in front of the plane end mirror inside the VECSEL cavity where the laser beam diameter has a minimum diameter of approximately 280 µm. Optimum phase matching for the THz wave is reached for THz emission perpendicular to the optical axis of the cavity. The THz emission is collimated with a cylindrical lens (CL) with a focal length of 3 mm and then focused with a biconvex spherical lens (BL) with a focal length of 70 mm. The THz spot near the focus behind the biconvex lens is monitored with a THz camera module (IRXCAM INO384THz, INO, Quebec, Canada) for different positions in beam propagation direction.

Within the measurement, a custom-made software was used that operates the THz camera module, a shutter device and a linear translation stage on which the camera module is mounted, respectively. Multiple pictures of the beam cross section and reference pictures for later background subtraction are recorded at each position. Because offset values and noise strongly influence the calculation of the second-moment width D4σ (see [19] for a

definition) derived from beam profile measurements, an additional processing of the measured raw data has been applied. The processing consists of four steps to correct for the background offset signal, the camera non-uniformity, the background noise where there is no THz signal present and smoothing of the signal, respectively.

Applying the definition of the second-moment width D4σ to the corrected THz beam size measurements, second-moment values for x- and y-direction, respectively, have been calculated.

The inset in Fig. 2 shows a grey-scale image of the focused beam profile. The two cross sections in x- and y-direction show the beam profile that can be well approximated by a Gaussian profile. The main part of Fig. 2 shows the beam width D4σ of the beam profile for x- and y-direction for different positions behind the focusing spherical lens.

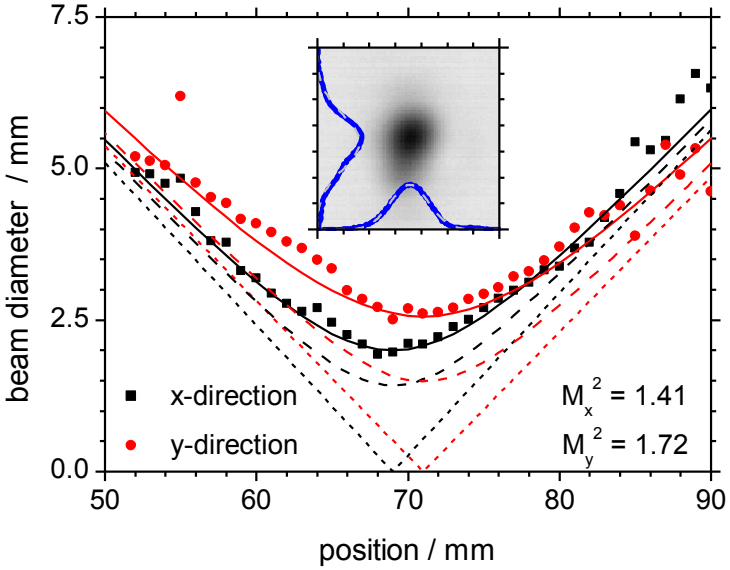

Fig. 2 Beam diameter along propagation direction for the TECSEL in black for x- and in red for y-direction, respectively. Solid lines represent the fit to the data. Dashed and short dashed lines represent the diameter for a Gaussian beam and the geometrical limit, respectively. The inset shows a 3.5mm times 3.5mm part of an image of the beam profile at propagation distance of 70 mm. Orthogonal profiles in blue and their Gaussian fits in dashed grey lines are displayed, too.

The beam quality factor M^2 for both the x- and the y-direction, respectively, has been calculated following Ref. [11] on the basis of the observed minimal diameter at focal position together with the observed far field divergence angle. Fig. 2 shows as solid lines the derived fits to the measured beam widths D4σ for different positions behind the focusing spherical lens. These resulting fits are used to calculate M^2. For comparison,

dashed lines in Fig. 2 represent the beam widths D4σ in case of the situation of the observed far field divergence angle but for a beam quality factor of M^2=1, while short dashed lines represent the observed far field divergence angle, *i. e*. the geometrical limit, respectively.

The deduced beam quality factors M^2 for x- and y-direction are 1.41 and 1.72, respectively. The derived values reflect the good beam quality of the continuous-wave THz source TECSEL that can be understood by the controlled geometrical conditions of the cavity modes used for frequency conversion to the THz spectral range.

In conclusion, we have determined the M^2 of a terahertz beam emitted from a VECSEL-based continuous wave THz source, which exploits intra-cavity frequency mixing in a nonlinear crystal for THz generation.

Acknowledgment

G. U. acknowledges support from EMRP-NEW07. The EMRP is jointly funded by the EMRP participating countries within EURAMET and the European Union. The authors further thank Bernd Heinen and Wolfgang Stolz for processing the VECSEL chip. Additionally, the authors would like to thank Maik Scheller and Jerome V. Moloney for valuable discussions.

References

[1] T. Kürner and S. Priebe, “Towards THz Communications - Status in Research, Standardization and Regulation,” J. Infrared Millim. Terahertz Waves **35**, 53–62 (2013).

[2] C. Jördens and M. Koch, “Detection of foreign bodies in chocolate with pulsed terahertz spectroscopy,” Opt. Eng. **47**, 037003–037003–5 (2008).

[3] C. Jördens, M. Scheller, S. Wietzke, D. Romeike, C. Jansen, T. Zentgraf, K. Wiesauer, V. Reisecker, and M. Koch, “Terahertz spectroscopy to study the orientation of glass fibres in reinforced plastics,” Compos. Sci. Technol. **70**, 472–477 (2010).

[4] E. Castro-Camus, M. Palomar, and A. A. Covarrubias, “Leaf water dynamics of Arabidopsis thaliana monitored in-vivo using terahertz time-domain spectroscopy,” Sci. Rep. **3**, 2910 (2013).

[5] K. Krügener, M. Schwerdtfeger, S. F. Busch, A. Soltani, E. Castro-Camus, M. Koch, and W. Viöl, "Terahertz meets sculptural and architectural art: Evaluation and conservation of stone objects with T-ray technology," Sci. Rep. **5**, 14842 (2015).

[6] M. Scheller, J. M. Yarborough, J. V. Moloney, M. Fallahi, M. Koch, and S. W. Koch, "Room temperature continuous wave milliwatt terahertz source," Opt. Express **18**, 27112–27117 (2010).

[7] A. Chernikov, M. Wichmann, M. K. Shakfa, M. Scheller, J. V. Moloney, S. W. Koch, and M. Koch, "Time-dynamics of the two-color emission from vertical-external-cavity surface-emitting lasers," Appl. Phys. Lett. **100**, 041114 (2012).

[8] M. Wichmann, M. K. Shakfa, F. Zhang, B. Heinen, M. Scheller, A. Rahimi-Iman, W. Stolz, J. V. Moloney, S. W. Koch, and M. Koch, "Evolution of multi-mode operation in vertical-external-cavity surface-emitting lasers," Opt. Express **21**, 31940–31950 (2013).

[9] M. Wichmann, M. Stein, A. Rahimi-Iman, S. W. Koch, and M. Koch, "Interferometric Characterization of a Semiconductor Disk Laser driven Terahertz Source," J. Infrared Millim. Terahertz Waves **35**, 503–508 (2014).

[10] M. Wichmann, G. Town, J. Quante, M. Gaafar, A. Rahimi-Iman, W. Stolz, S. W. Koch, and M. Koch, "Anti-Phase Noise Dynamics in a Dual-Wavelength Vertical-External-Cavity Surface-Emitting Laser," IEEE Photonics Technol. Lett. **27**, 2039 - 2042 (2015).

[11] A. E. Siegman, "How to (Maybe) Measure Laser Beam Quality," in DPSS (Diode Pumped Solid State) Lasers: Applications and Issues (1998), paper MQ1 (1998).

[12] ISO 11146 Lasers and laser-related equipment – Test methods for laser beam parameters – Beam width, divergence, angle and beam propagation factor, 1999.

[13] H. Richter, N. Rothbart, and H.-W. Hübers, "Characterizing the beam properties of terahertz quantum-cascade lasers," J. Infrared Millim. Terahertz Waves **35**, 686–698 (2014).

[14] F. Zhang, B. Heinen, M. Wichmann, C. Möller, B. Kunert, A. Rahimi-Iman, W. Stolz, and M. Koch, "A 23-watt single-frequency vertical-external-cavity surface-emitting laser," Opt. Express **22**, 12817–12822 (2014)

References

[1] T. H. Maiman, "Stimulated Optical Radiation in Ruby," *Nature*, vol. 187, no. 4736, pp. 493–494, 1960.

[2] A. Haglund, J. S. Gustavsson, J. Vukusic, P. Modh, and A. Larsson, "Single fundamental-mode output power exceeding 6 mW from VCSELs with a shallow surface relief," *IEEE Photonics Technol. Lett.*, vol. 16, no. 2, pp. 368–370, 2004.

[3] M. Kuznetsov, F. Hakimi, R. Sprague, and A. Mooradian, "High-power (>0.5 W CW) diode-pumped vertical-external-cavity surface-emitting semiconductor lasers with circular TEM00 beams," *IEEE Photonics Technol. Lett.*, vol. 9, no. 8, pp. 1063–1065, Aug. 1997.

[4] M. Kuznetsov, F. Hakimi, R. Sprague, and A. Mooradian, "Design and characteristics of high-power (>0.5-W CW) diode-pumped vertical-external-cavity surface-emitting semiconductor lasers with circular TEM_{00} beams," *Sel. Top. Quantum Electron. IEEE J. Of*, vol. 5, no. 3, pp. 561–573, Jun. 1999.

[5] A. C. Tropper, H. D. Foreman, A. Garnache, K. G. Wilcox, and S. H. Hoogland, "Vertical-external-cavity semiconductor lasers," *J. Phys. Appl. Phys.*, vol. 37, no. 9, pp. R75–R85, May 2004.

[6] U. Keller and A. C. Tropper, "Passively modelocked surface-emitting semiconductor lasers," *Phys. Rep.*, vol. 429, no. 2, pp. 67–120, Jun. 2006.

[7] O. G. Okhotnikov, *Semiconductor Disk Lasers: Physics and Technology*. John Wiley & Sons, 2010.

[8] A. Rahimi-Iman, "Recent advances in VECSELs," *J. Opt.*, vol. 18, no. 9, p. 093003, 2016.

[9] B. Rudin *et al.*, "Highly efficient optically pumped vertical-emitting semiconductor laser with more than 20 W average output power in a fundamental transverse mode," *Opt. Lett.*, vol. 33, no. 22, pp. 2719–2721, Nov. 2008.

[10] W. J. Alford *et al.*, "Optically Pumped Semiconductor Lasers for Precision Spectroscopic Applications," *IEEE J. Quantum Electron.*, vol. 49, no. 8, pp. 719–727, 2013.

[11] P. Georges, I. Sagnes, and A. Garnache, "Design of a low-threshold VECSEL emitting at 852 nm for Cesium atomic clocks," *Opt. Quantum Electron.*, vol. 40, no. 2–4, pp. 167–173, Jan. 2008.

[12] S. Ranta, M. Tavast, T. Leinonen, R. Epstein, and M. Guina, "Narrow linewidth 1118/559 nm VECSEL based on strain compensated GaInAs/GaAs quantum-wells for laser cooling of Mg-ions," *Opt. Mater. Express*, vol. 2, no. 8, pp. 1011–1019, Aug. 2012.

[13] LIGO Scientific Collaboration and Virgo Collaboration *et al.*, "Observation of Gravitational Waves from a Binary Black Hole Merger," *Phys. Rev. Lett.*, vol. 116, no. 6, p. 061102, 2016.

[14] M. Frede *et al.*, "Fundamental mode, single-frequency laser amplifier for gravitational wave detectors," *Opt. Express*, vol. 15, no. 2, p. 459, Jan. 2007.

[15] P. Kwee *et al.*, "Stabilized high-power laser system for the gravitational wave detector advanced LIGO," *Opt. Express*, vol. 20, no. 10, pp. 10617–10634, May 2012.

[16] C. L. Mueller *et al.*, "The advanced LIGO input optics," *Rev. Sci. Instrum.*, vol. 87, no. 1, p. 014502, Jan. 2016.

[17] F. Zhang *et al.*, "A 23-watt single-frequency vertical-external-cavity surface-emitting laser," *Opt. Express*, vol. 22, no. 11, pp. 12817–12822, Jun. 2014.

[18] M. Scheller, J. M. Yarborough, J. V. Moloney, M. Fallahi, M. Koch, and S. W. Koch, "Room temperature continuous wave milliwatt terahertz source," *Opt. Express*, vol. 18, no. 26, pp. 27112–27117, Dec. 2010.
[19] A. Chernikov *et al.*, "Time-dynamics of the two-color emission from vertical-external-cavity surface-emitting lasers," *Appl. Phys. Lett.*, vol. 100, no. 4, p. 041114, Jan. 2012.
[20] M. Wichmann *et al.*, "Evolution of multi-mode operation in vertical-external-cavity surface-emitting lasers," *Opt. Express*, vol. 21, no. 26, pp. 31940–31950, Dec. 2013.
[21] M. Wichmann *et al.*, "Antiphase Noise Dynamics in a Dual-Wavelength Vertical-External-Cavity Surface-Emitting Laser," *IEEE Photonics Technol. Lett.*, vol. 27, no. 19, pp. 2039–2042, Oct. 2015.
[22] T. Leinonen, S. Ranta, A. Laakso, Y. Morozov, M. Saarinen, and M. Pessa, "Dual-wavelength generation by vertical external cavity surface-emitting laser," *Opt. Express*, vol. 15, no. 20, pp. 13451–13456, Oct. 2007.
[23] C. Hessenius, M. Lukowski, and M. Fallahi, "High-power tunable two-wavelength generation in a two chip co-linear T-cavity vertical external-cavity surface-emitting laser," *Appl. Phys. Lett.*, vol. 101, no. 12, p. 121110, Sep. 2012.
[24] C. Hessenius, M. Lukowski, and M. Fallahi, "Tunable type II intracavity sum-frequency generation in a two chip collinear vertical external cavity surface emitting laser," *Opt. Lett.*, vol. 38, no. 5, pp. 640–642, Mar. 2013.
[25] M. Lukowski, C. Hessenius, and M. Fallahi, "Widely Tunable High-Power Two-Color VECSELs for New Wavelength Generation," *IEEE J. Sel. Top. Quantum Electron.*, vol. 21, no. 1, pp. 1–8, Jan. 2015.
[26] F. Zhang, M. Gaafar, C. Möller, W. Stolz, M. Koch, and A. Rahimi-Iman, "Dual-Wavelength Emission From a Serially Connected Two-Chip VECSEL," *IEEE Photonics Technol. Lett.*, vol. 28, no. 8, pp. 927–929, Apr. 2016.
[27] F. Zhang *et al.*, "Investigation of the Beam Quality of a Terahertz Emitting Vertical-External-Cavity Surface-Emitting Laser," *J. Infrared Millim. Terahertz Waves*, vol. 37, no. 6, pp. 536–539, Apr. 2016.
[28] A. C. Tropper and S. Hoogland, "Extended cavity surface-emitting semiconductor lasers," *Prog. Quantum Electron.*, vol. 30, no. 1, pp. 1–43, Jan. 2006.
[29] J. Hader *et al.*, "Predictive Microscopic Modeling of VECSELs," *IEEE J. Quantum Electron.*, vol. 46, no. 5, pp. 810–817, May 2010.
[30] A. E. Siegman, *Lasers*. University Science Books, 1986.
[31] S. Calvez, J. E. Hastie, M. Guina, O. G. Okhotnikov, and M. D. Dawson, "Semiconductor disk lasers for the generation of visible and ultraviolet radiation," *Laser Photonics Rev.*, vol. 3, no. 5, pp. 407–434, Sep. 2009.
[32] B. Heinen *et al.*, "106 W continuous-wave output power from vertical-external-cavity surface-emitting laser," *Electron. Lett.*, vol. 48, no. 9, pp. 516–517, 2012.
[33] B. Heinen, F. Zhang, M. Sparenberg, B. Kunert, M. Koch, and W. Stolz, "On the Measurement of the Thermal Resistance of Vertical-External-Cavity Surface-Emitting Lasers (VECSELs)," *Quantum Electron. IEEE J. Of*, vol. 48, no. 7, pp. 934–940, Jul. 2012.
[34] J. E. Hastie, L. G. Morton, A. J. Kemp, M. D. Dawson, A. B. Krysa, and J. S. Roberts, "Tunable ultraviolet output from an intracavity frequency-doubled red vertical-external-cavity surface-emitting laser," *Appl. Phys. Lett.*, vol. 89, no. 6, pp. 061114-061114-3, Aug. 2006.
[35] J. E. Hastie *et al.*, "0.5-W single transverse-mode operation of an 850-nm diode-pumped surface-emitting semiconductor laser," *IEEE Photonics Technol. Lett.*, vol. 15, no. 7, pp. 894–896, Jul. 2003.

[36] A. J. Kemp *et al.*, "Thermal management in vertical-external-cavity surface-emitting lasers: finite-element analysis of a heatspreader approach," *IEEE J. Quantum Electron.*, vol. 41, no. 2, pp. 148–155, Feb. 2005.
[37] J. M. Hopkins *et al.*, "0.6W CW GaInNAs vertical external-cavity surface emitting laser operating at 1.32μm," *Electron. Lett.*, vol. 40, no. 1, pp. 30–31, 2004.
[38] H. Lindberg, M. Strassner, E. Gerster, J. Bengtsson, and A. Larsson, "Thermal management of optically pumped long-wavelength InP-based semiconductor disk lasers," *IEEE J. Sel. Top. Quantum Electron.*, vol. 11, no. 5, pp. 1126–1134, Sep. 2005.
[39] A. Härkönen *et al.*, "1-W antimonide-based vertical external cavity surface emitting laser operating at 2-μm," *Opt. Express*, vol. 14, no. 14, pp. 6479–6484, Jul. 2006.
[40] A. J. Kemp *et al.*, "Thermal Management in 2.3-μm Semiconductor Disk Lasers: A Finite Element Analysis," *IEEE J. Quantum Electron.*, vol. 44, no. 2, pp. 125–135, 2008.
[41] M. Rahim, M. Arnold, F. Felder, K. Behfar, and H. Zogg, "Midinfrared lead-chalcogenide vertical external cavity surface emitting laser with 5 μm wavelength," *Appl. Phys. Lett.*, vol. 91, no. 15, pp. 151102-151102–3, Oct. 2007.
[42] M. Y. A. Raja *et al.*, "Resonant periodic gain surface-emitting semiconductor lasers," *IEEE J. Quantum Electron.*, vol. 25, no. 6, pp. 1500–1512, 1989.
[43] S. W. Corzine, R. S. Geels, J. W. Scott, R. H. Yan, and L. A. Coldren, "Design of Fabry-Perot surface-emitting lasers with a periodic gain structure," *IEEE J. Quantum Electron.*, vol. 25, no. 6, pp. 1513–1524, 1989.
[44] M. Y. A. Raja, S. R. J. Brueck, M. O. Scully, and C. Lee, "Resonant periodic-gain surface-emitting semiconductor lasers and correlated emission in a ring cavity," *Phys. Rev. A*, vol. 44, no. 7, pp. 4599–4607, 1991.
[45] T.-L. Wang *et al.*, "Quantum design strategy pushes high-power vertical-external-cavity surface-emitting lasers beyond 100 W," *Laser Photonics Rev.*, vol. 6, no. 5, pp. L12–L14, Sep. 2012.
[46] S. Lutgen, T. Albrecht, P. Brick, W. Reill, J. Luft, and W. Späth, "8-W high-efficiency continuous-wave semiconductor disk laser at 1000 nm," *Appl. Phys. Lett.*, vol. 82, no. 21, pp. 3620–3622, May 2003.
[47] B. Heinen, C. Moller, K. Jandieri, B. Kunert, M. Koch, and W. Stolz, "The Thermal Resistance of High-Power Semiconductor Disk Lasers," *IEEE J. Quantum Electron.*, vol. 51, no. 5, pp. 1–9, May 2015.
[48] M. Scheller, T.-L. Wang, B. Kunert, W. Stolz, S. W. Koch, and J. V. Moloney, "Passively modelocked VECSEL emitting 682 fs pulses with 5.1W of average output power," *Electron. Lett.*, vol. 48, no. 10, pp. 588–589, May 2012.
[49] A. H. Quarterman *et al.*, "A passively mode-locked external-cavity semiconductor laser emitting 60-fs pulses," *Nat. Photonics*, vol. 3, no. 12, pp. 729–731, 2009.
[50] M. Gaafar *et al.*, "Harmonic self-mode-locking of optically pumped semiconductor disc laser," *Electron. Lett.*, vol. 50, no. 7, pp. 542–543, Mar. 2014.
[51] M. Gaafar *et al.*, "Self-mode-locked quantum-dot vertical-external-cavity surface-emitting laser," *Opt. Lett.*, vol. 39, no. 15, pp. 4623–4626, Aug. 2014.
[52] M. A. Gaafar, A. Rahimi-Iman, K. A. Fedorova, W. Stolz, E. U. Rafailov, and M. Koch, "Mode-locked semiconductor disk lasers," *Adv. Opt. Photonics*, vol. 8, no. 3, pp. 370–400, Sep. 2016.
[53] M. A. Holm, D. Burns, A. I. Ferguson, and M. D. Dawson, "Actively stabilized single-frequency vertical-external-cavity AlGaAs laser," *IEEE Photonics Technol. Lett.*, vol. 11, no. 12, pp. 1551–1553, Dec. 1999.
[54] M. Jacquemet *et al.*, "Single-frequency cw vertical external cavity surface emitting semiconductor laser at 1003 nm and 501 nm by intracavity frequency doubling," *Appl. Phys. B*, vol. 86, no. 3, pp. 503–510, Nov. 2006.

[55] A. Rantamaki, A. Chamorovskiy, J. Lyytikainen, and O. Okhotnikov, "4.6-W Single Frequency Semiconductor Disk Laser With kHz Linewidth," *IEEE Photonics Technol. Lett.*, vol. 24, no. 16, pp. 1378–1380, Aug. 2012.
[56] T. Leinonen *et al.*, "High power (23W) vertical external cavity surface emitting laser emitting at 1180 nm," *Proc. SPIE*, 2013, vol. 8606, pp. 860604-860604–6.
[57] A. Laurain, C. Mart, J. Hader, J. V. Moloney, B. Kunert, and W. Stolz, "15 W Single Frequency Optically Pumped Semiconductor Laser With Sub-Megahertz Linewidth," *IEEE Photonics Technol. Lett.*, vol. 26, no. 2, pp. 131–133, 2014.
[58] A. Rantamäki *et al.*, "High-power flip-chip semiconductor disk laser in the 1.3 μm wavelength band," *Opt. Lett.*, vol. 39, no. 16, pp. 4855–4858, Aug. 2014.
[59] A. Ouvrard, A. Garnache, L. Cerutti, F. Genty, and D. Romanini, "Single-frequency tunable Sb-based VCSELs emitting at 2.3 μm," *IEEE Photonics Technol. Lett.*, vol. 17, no. 10, pp. 2020–2022, Oct. 2005.
[60] S. Kaspar, M. Rattunde, T. Töpper, C. Manz, K. Köhler, and J. Wagner, "Semiconductor disk laser at 2.05 μm wavelength with <100 kHz linewidth at 1 W output power," *Appl. Phys. Lett.*, vol. 100, no. 3, pp. 031109-031109-3, Jan. 2012.
[61] S. Kaspar *et al.*, "Sub-MHz-Linewidth 200-mW Actively Stabilized 2.3-μm Semiconductor Disk Laser," *IEEE Photonics Technol. Lett.*, vol. 23, no. 20, pp. 1538–1540, Oct. 2011.
[62] S. Kaspar *et al.*, "Linewidth Narrowing and Power Scaling of Single-Frequency 2.X μm GaSb-Based Semiconductor Disk Lasers," *IEEE J. Quantum Electron.*, vol. 49, no. 3, pp. 314–324, Mar. 2013.
[63] B. Cocquelin *et al.*, "Tunable single-frequency operation of a diode-pumped vertical external-cavity laser at the cesium D2 line," *Appl. Phys. B*, vol. 95, no. 2, pp. 315–321, Jan. 2009.
[64] S. Giet *et al.*, "Stabilization of a semiconductor disk laser using an intra-cavity high reflectivity grating," *Opt. Express*, vol. 15, no. 25, pp. 16520–16526, 2007.
[65] A. Laurain, C. Mart, J. Hader, J. V. Moloney, B. Kunert, and W. Stolz, "Optical noise of stabilized high-power single frequency optically pumped semiconductor laser," *Opt. Lett.*, vol. 39, no. 6, pp. 1573–1576, Mar. 2014.
[66] M. Kuznetsov, M. Stern, and J. Coppeta, "Single transverse mode optical resonators," *Opt. Express*, vol. 13, no. 1, pp. 171–181, 2005.
[67] O. Svelto and D. C. Hanna, *Principles of lasers*. Springer, 1998.
[68] C. Voumard, R. Salathé, and H. Weber, "Mode selection by etalons in external diode laser cavities," *Appl. Phys.*, vol. 7, no. 2, pp. 123–126, Jun. 1975.
[69] S. Giet *et al.*, "Spectral narrowing and locking of a vertical-external-cavity surface-emitting laser using an intracavity volume Bragg grating," *IEEE Photonics Technol. Lett.*, vol. 18, no. 16, pp. 1786–1788, Aug. 2006.
[70] A. Garnache *et al.*, "Single frequency free-runing low noise compact external-cavity VCSELs at high power level (50mW)," in *34th European Conference on Optical Communication, 2008. ECOC 2008*, 2008, pp. 1–2.
[71] A. Laurain, M. Myara, G. Beaudoin, I. Sagnes, and A. Garnache, "High power single-frequency continuously-tunable compact extended-cavity semiconductor laser," *Opt. Express*, vol. 17, no. 12, pp. 9503–9508, Jun. 2009.
[72] A. Laurain, M. Myara, G. Beaudoin, I. Sagnes, and A. Garnache, "Multiwatt-power highly-coherent compact single-frequency tunable Vertical-External-Cavity Surface-Emitting Semiconductor Laser," *Opt. Express*, vol. 18, no. 14, pp. 14627–14636, Jul. 2010.
[73] L. G. Morton, H. D. Foreman, J. E. Hastie, M. D. Dawson, and E. Riis, "Actively Stabilised Single-Frequency Red VECSEL," in *Advanced Solid-State Photonics (2007), paper WB7*, 2007, p. WB7.

[74] A. Rantamäki, J. Rautiainen, A. Sirbu, A. Mereuta, E. Kapon, and O. G. Okhotnikov, "1.56 μm 1 watt single frequency semiconductor disk laser," *Opt. Express*, vol. 21, no. 2, pp. 2355–2360, Jan. 2013.
[75] L. Fan *et al.*, "Linearly polarized dual-wavelength vertical-external-cavity surface-emitting laser," *Appl. Phys. Lett.*, vol. 90, no. 18, p. 181124, Apr. 2007.
[76] C. Hessenius, M. Fallahi, J. Moloney, and R. Bedford, "Lateral lasing and ASE reduction in VECSELs," *Proc. SPIE*, 2011, vol. 7919, pp. 791909-791909–8.
[77] C. Hessenius, M. Lukowski, J. Moloney, and M. Fallahi, "Tunable single-frequency yellow laser for sodium guidestar applications".
[78] C. Hessenius, P. Y. Guinet, M. Lukowski, J. Moloney, and M. Fallahi, "589-nm single-frequency VECSEL for sodium guidestar applications," *Proc. SPIE*, 2012, vol. 8242, p. 82420E–82420E–7.
[79] A. L. Schawlow and C. H. Townes, "Infrared and Optical Masers," *Phys. Rev.*, vol. 112, no. 6, pp. 1940–1949, 1958.
[80] D. W. Allan, "Statistics of atomic frequency standards," *Proc. IEEE*, vol. 54, no. 2, pp. 221–230, 1966.
[81] D. F. Riehle, *Frequency Standards: Basics and Applications*. 2005.
[82] T. W. Hansch and B. Couillaud, "Laser frequency stabilization by polarization spectroscopy of a reflecting reference cavity," *Opt. Commun.*, vol. 35, no. 3, pp. 441–444, 1980.
[83] R. W. P. Drever *et al.*, "Laser phase and frequency stabilization using an optical resonator," *Appl. Phys. B*, vol. 31, no. 2, pp. 97–105, Jun. 1983.
[84] Y. Kaneda *et al.*, "Continuous-wave all-solid-state 244 nm deep-ultraviolet laser source by fourth-harmonic generation of an optically pumped semiconductor laser using CsLiB6O10 in an external resonator," *Opt. Lett.*, vol. 33, no. 15, pp. 1705–1707, Aug. 2008.
[85] J. Paul, Y. Kaneda, T.-L. Wang, C. Lytle, J. V. Moloney, and R. J. Jones, "Doppler-free spectroscopy of mercury at 253.7 nm using a high-power, frequency-quadrupled, optically pumped external-cavity semiconductor laser," *Opt. Lett.*, vol. 36, no. 1, pp. 61–63, Jan. 2011.
[86] E. Kantola, T. Leinonen, J.-P. Penttinen, V.-M. Korpijärvi, and M. Guina, "615 nm GaInNAs VECSEL with output power above 10 W," *Opt. Express*, vol. 23, no. 16, pp. 20280–20287, Aug. 2015.
[87] E. Kantola, T. Leinonen, S. Ranta, M. Tavast, and M. Guina, "High-efficiency 20 W yellow VECSEL," *Opt. Express*, vol. 22, no. 6, pp. 6372–6380, Mar. 2014.
[88] Y. A. Morozov, I. S. Nefedov, and V. Y. Aleshkin, "Nonlinear frequency conversion in a double vertical-cavity surface-emitting laser," *Semiconductors*, vol. 38, no. 11, pp. 1350–1355.
[89] J. Rautiainen, I. Krestnikov, J. Nikkinen, and O. G. Okhotnikov, "2.5 W orange power by frequency conversion from a dual-gain quantum-dot disk laser," *Opt. Lett.*, vol. 35, no. 12, p. 1935, Jun. 2010.
[90] T. Kürner and S. Priebe, "Towards THz Communications - Status in Research, Standardization and Regulation," *J. Infrared Millim. Terahertz Waves*, vol. 35, no. 1, pp. 53–62, Aug. 2013.
[91] C. Jördens and M. Koch, "Detection of foreign bodies in chocolate with pulsed terahertz spectroscopy," *Opt. Eng.*, vol. 47, no. 3, pp. 037003-037003-5, 2008.
[92] C. Jördens *et al.*, "Terahertz spectroscopy to study the orientation of glass fibres in reinforced plastics," *Compos. Sci. Technol.*, vol. 70, no. 3, pp. 472–477, Mar. 2010.
[93] E. Castro-Camus, M. Palomar, and A. A. Covarrubias, "Leaf water dynamics of Arabidopsis thaliana monitored in-vivo using terahertz time-domain spectroscopy," *Sci. Rep.*, vol. 3, p. 2910, Oct. 2013.

[94] K. Krügener *et al.*, "Terahertz meets sculptural and architectural art: Evaluation and conservation of stone objects with T-ray technology," *Sci. Rep.*, vol. 5, p. 14842, Oct. 2015.
[95] C. Sirtori, "Applied physics: Bridge for the terahertz gap," *Nature*, vol. 417, no. 6885, pp. 132–133, 2002.
[96] M. Wichmann, M. Stein, A. Rahimi-Iman, S. W. Koch, and M. Koch, "Interferometric Characterization of a Semiconductor Disk Laser driven Terahertz Source," *J. Infrared Millim. Terahertz Waves*, vol. 35, no. 6–7, pp. 503–508, Apr. 2014.
[97] T. Leinonen, Y. A. Morozov, A. Harkonen, and M. Pessa, "Vertical external-cavity surface-emitting laser for dual-wavelength generation," *IEEE Photonics Technol. Lett.*, vol. 17, no. 12, pp. 2508–2510, Dec. 2005.
[98] A. Jasik *et al.*, "Dual-wavelength vertical external-cavity surface-emitting laser: strict growth control and scalable design," *Appl. Phys. B*, vol. 122, no. 2, pp. 1–8, Jan. 2016.
[99] C. Hessenius, M. Lukowski, and M. Fallahi, "High-power tunable two-wavelength generation in a two chip co-linear T-cavity vertical external-cavity surface-emitting laser," *Appl. Phys. Lett.*, vol. 101, no. 12, pp. 121110-121110–3, Sep. 2012.
[100] F. Zhang, M. Gaafar, C. Möller, W. Stolz, M. Koch, and A. Rahimi-Iman, "A serially-connected two-chip VECSEL for dual-wavelength emission with high intracavity power," *Proc. SPIE*, 2016, vol. 9734, pp. 973414-973414–6.
[101] M. Schmid, S. Benchabane, F. Torabi-Goudarzi, R. Abram, A. I. Ferguson, and E. Riis, "Optical in-well pumping of a vertical-external-cavity surface-emitting laser," *Appl. Phys. Lett.*, vol. 84, no. 24, pp. 4860–4862, May 2004.
[102] S.-S. Beyertt *et al.*, "Optical in-well pumping of a semiconductor disk laser with high optical efficiency," *Quantum Electron. IEEE J. Of*, vol. 41, no. 12, pp. 1439–1449, Dec. 2005.
[103] Y. Sasaki, Y. Avetisyan, H. Yokoyama, and H. Ito, "Surface-emitted terahertz-wave difference-frequency generation in two-dimensional periodically poled lithium niobate," *Opt. Lett.*, vol. 30, no. 21, pp. 2927–2929, Nov. 2005.
[104] J. A. L'huillier, G. Torosyan, M. Theuer, Y. Avetisyan, and R. Beigang, "Generation of THz radiation using bulk, periodically and aperiodically poled lithium niobate – Part 1: Theory," *Appl. Phys. B*, vol. 86, no. 2, pp. 185–196, Jan. 2007.
[105] A. E. Siegman, "How to (Maybe) Measure Laser Beam Quality," in *DPSS (Diode Pumped Solid State) Lasers: Applications and Issues (1998), paper MQ1*, 1998, p. MQ1.
[106] "ISO 11146-1:2005 - Lasers and laser-related equipment -- Test methods for laser beam widths, divergence angles and beam propagation ratios -- Part 1: Stigmatic and simple astigmatic beams." [Online]. Available: http://www.iso.org/iso/iso_catalogue/catalogue_tc/catalogue_detail.htm?csnumber=33625.
[107] "ISO 11146-2:2005 - Lasers and laser-related equipment -- Test methods for laser beam widths, divergence angles and beam propagation ratios -- Part 2: General astigmatic beams." [Online]. Available: http://www.iso.org/iso/iso_catalogue/catalogue_tc/catalogue_detail.htm?csnumber=33626.
[108] A. E. Siegman, "Defining, measuring, and optimizing laser beam quality," pp. 2–12, Feb. 1993.
[109] J. Hader, H.-J. Yang, M. Scheller, J. V. Moloney, and S. W. Koch, "Microscopic analysis of saturable absorbers: Semiconductor saturable absorber mirrors versus graphene," *J. Appl. Phys.*, vol. 119, no. 5, p. 053102, Feb. 2016.
[110] F. Zhang, C. Möller, M. Koch, S. W. Koch, A. Rahimi-Iman, and W. Stolz, "Impact of detuning on the performance of VECSELs," *Opt. Express*, submitted.
[111] T.-L. Wang *et al.*, "Strategies for power scaling VECSELs," *Proc. SPIE*, 2012, vol. 8242, pp. 824209-824209–8.